UNIVERSITY OF
LIVERPOOL

RF Plasma Modification of Carbon Nanotubes for use in Molecular Electronic Devices.

Thesis submitted in accordance with the requirements of
the University of Liverpool for the degree of Doctor in Philosophy
by

Paul Aden

Department of Electrical Engineering & Electronics

April 2010

Acknowledgements

I would like to acknowledge the commitment, guidance and support from my supervisors Prof J W Bradley and Dr I Alexandrou.

I am also grateful to Dr Paul Unsworth, Dr Sam Haq and Dr Vlad Vishnyakov for allowing me to use use equipment and sharing their knowledge during the course of my research.

I would like to thank some of the many I have worked with including Miss Lindsey Duffy, Dr Ian Swindles, Mr Alan Roby, Dr Gregory Clark, Miss Eleanor Watters, Mr Dimitrios Delaportas, Mr Kevin Molloy, Mr Tom Dowick, Dr Paul Byrant and Dr Malina Mahadavan. I would also like to take this opportunity to mention my friend Colin, because he asked so nicely.

Most of all I would like to thank Gemma, my loving girlfriend, for putting up with my endless working days. Finally I would like to thank my family for their support and season tickets.

Abstract

This thesis explores the possibility of modifying the carbon lattice structure by nitrogen decoration using radio frequency (RF) plasma, in order to modify multi wall nanotubes for use in electronic devices, as well as an investigation into nanotube production from plasma arcs in liquid. Modification of multi wall nanotubes was performed using a non thermal, low temperature plasma functionalisation process. Which is a clean, safe, simple method of modifying nanotube properties. The activated species contained with plasmas are able to initiate chemical and physical reactions at the surface, resulting in surface modification.

It has been shown that; carbon nanotubes can be successfully be created using plasma arc in liquid. That this plasma arc in liquid has unique and interesting properties which could be tuned to provide tailored carbon nanotubes. A theory for the process which take place within the arc to produce carbon nanotubes had been proposed. RF Plasma analysis has been carried out to give an insight into the physics behind the modifications to prevent the process from being a 'black box' system. An understanding of the RF plasma modification process will allow for selection of plasma properties to achieve specific carbon nanotube properties. Carbon nanotubes have be produced and imaged and details on dispersion techniques discussed. Random network carbon nanotube transistors have been designed, developed, used as analytical techniques, and a theory proposed for there operation.

Carbon Nanotubes have been shown to have unique electrical properties which have made them an appealing electronic component for many researchers. High carrier mobility and semiconductor characteristics have made carbon nanotubes a promising alternative to silicon. A carbon nanotube is constructed from a graphene sheet rolled into a cylinder, this is known as a single wall nanotube, rolling multiple sheets produces

a multi-wall nanotube. Whereas single wall nanotubes have semiconducting properties multi wall nanotubes do not, however, cost and complications associated with producing and using single wall nanotubes means that multi wall nanotubes are more commercially accessible. Multi-wall nanotubes are physically and electrically more stable than their single wall counterparts. They are less likely to naturally form nano ropes and/or bundles, which exhibit low solubility in water and other organic solvents. Cheaper and easier to produce multi-wall carbon nanotubes have few draw backs, however as they do not always behave as semiconductors they cannot be utilised as useful semiconductor devices.

Chapter one gives an oversight into the applications, physics and background behind Carbon Nanotubes and plasma. Chapter two discusses and explains the equipment used throughout this research. Detailing the design and use of the purpose built RF Plasma rig (designed from the ground up for nanotube modification) and the Arc in Liquids apparatus. Design of the analytical techniques, such as Langmuir and Capacitive probes, Mass Spectrometry for extraction plasma properties as well as OES, XPS, FTIR, Raman spectroscopy and electrical characteristics of the carbon nanotubes are also discussed here. Details of the experimental setup and procedures is also explained.

Chapter three gives results and discussion of multi wall carbon nanotubes which have been created in the lab using a relatively new plasma arc in liquid technique. The unique 'home made' arc system was investigated and using various liquids (Liquid Nitrogen, Water and a Water ethanol mix) the arc generated was studied using electrical characterisation and Optical Emission Spectroscopy. A theory behind the formation and expansion of the gas bubble within the liquid has been proposed. By using OES time averaged and time resolved it has been possible to see that the evolution of the arc discharge and link it with various parameters such as voltage and current. It has been shown that nanotube production in liquid is a valid up scalable process of creating carbon nanotubes.

Chapter four explores the results from the RF plasma properties establishing a link between chapter three and five to give a greater understanding of the processes taking place during modification. Using some well established techniques such as Langmuir Probes, Capacitive Probes and Mass Spectrometry, various plasma properties have been

extracted to give a detailed understanding of the processes taking place. A knowledge of the physical processes within the plasma would allow for tuning of the nanotube modification, allowing different properties to be obtained depending upon the input parameters and variables.

Chapter five covers the findings of carbon nanotube analysis, before and after modification. Unique carbon nanotube transistors have been designed and developed into functional molecular electron devices. These transistors use a percolation path structure to enable transistor channel conduction, which averages the properties of the nanotubes across the channel. The design of these transistors could lend themselves (coupled with localised modifications) to 'printed' electronic components, for quick and cheap mass production circuits. The electrical properties of these devices have been investigated, and they have been used as a analytical tools. Fourier Transform Infrared Spectroscopy, X-ray Photoelectron Spectroscopy, Raman Spectroscopy, Scanning Electron Microscopy and Transmission Electron Microscopy, have also been used to analyse modification of carbon nanotubes.

Contents

Chapter 1

Introduction

1.1 Nanotubes

Carbon Nanotubes (CNTs) have been shown to have excellent mechanical and electrical properties [1] [2]. As such, the properties of CNTs have become the subject of much investigation over recent years. Multiwalled CNTs (MWNTs) where discovered by Sumio Ijima in 1991 whilst at NEC, and two years later he and Donald Bethune at IBM independently observed single walled CNTs (SWNTs). An idea originally devised in 1990 by Dr. Richard Smalley who commented on the possibility of tubular buckyballs, (sixty carbon atoms arranged in a soccer ball shape, also known as Fullerene Spheres). CNTs are created when a sheet of graphene (a single layer of graphite atoms) approaches 30nm it becomes more energetically favourable for this very narrow strip of graphite to curl up into a cylinder [3], figure 1.1. CNTs are composed entirely of sp^2 bonds, similar to graphite, which are stronger than the sp^3 bonds found in diamond. This bonding structure provides them with unique strength, often being quoted to be a hundred times stronger than steel [1], although this value is expected to vary depending upon the chirality.

It is easier to produce CNTs from strips that are three to eight sheets, known as walls, thick. This is what is know as a Multiwalled Nanotube (MWNT), a TEM image is shown as an example in figure 1.2. Each wall is separated by an interlayer gap of approximately 0.34nm [4].

Carbon nanotubes have numerous applications; Recently BMC, a Swiss bicycle manufacturer, entered a bicycle into the Tour de France utilising carbon nanotubes in the frame of the bike. Utilising carbon nanotube to re-inforce a resin matrix they

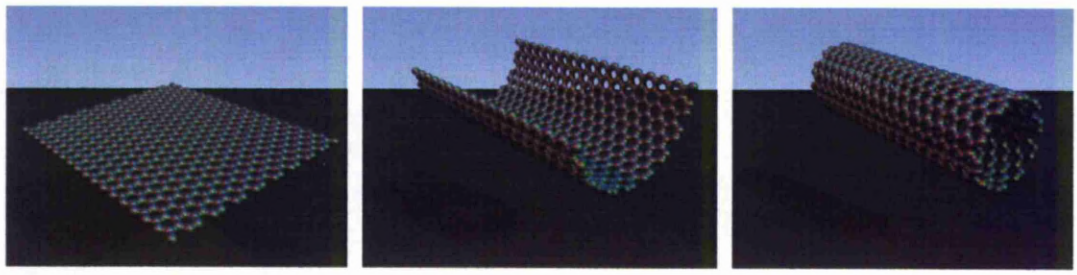

Figure 1.1: From left to right, sheet of graphene folds into single wall nanotube.

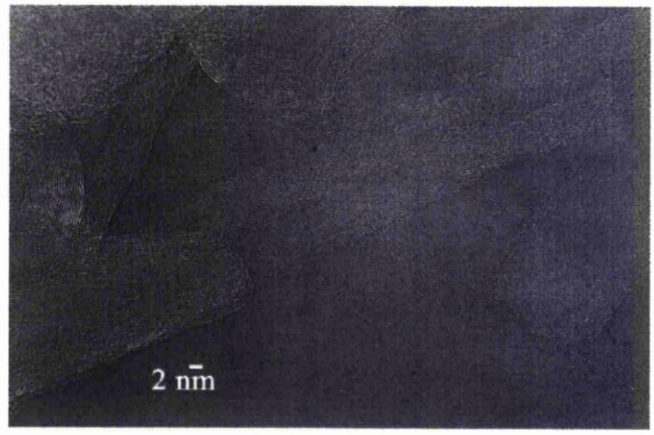

Figure 1.2: TEM of a multiwalled carbon nanotube produced in a plasma arc in H_2O.

created a bike with unrivalled strength with minimum weight [5]. It is this lightweight strength that has seen a number of companies and researchers weave nanotube fibres into clothes to create protective clothing products [6]. A. Fennimore et al [7] have produced the worlds smallest motor constructed of a MWNT, they have taken advantage of the low fiction between the walls of the nanotube as a linear bearing. It has also been proposed that CNTs could be used as a drug delivery systems [8,9] for targeting cancerous cells or even as nano sized test tubes [10]. The size, physical and electrical properties have made carbon nanotubes an option to replace materials such as ITO in flexible displays [11]. It is also conceivable that soluble carbon nanotubes could be used to simply ink-jet print electrical circuits on any variety of materials. Recently it was shown that by applying currents to CNTs it was possible to produce sound via thermoacoustics [12], CNTs can be found in some of the latest solar cells, Mirtra et al [13] used a buckyball, nantotube polymer composite to trap and transport electrons which are created by dissociation of excitons created by sunlight. Researchers at MIT have

been using CNTs to improve the performance of capacitors. Due to the high aspect ration 'fields' of carbon nanotubes have massive surface areas, making them potential useful for storing charge in batteries.

Liming Dai [14] showed that nitrogen doped carbon nanotubes was a suitable replacement for the platinum catalysts used in fuel cells. Leveraging the phenomenon of tunnelling in CNTs it is possible to produce field emission displays, these displays could potentially have; low power consumption, high images quality and could be no thicker than the glass protecting them. Such displays are based on the CNTs emitting electrons via tunnelling.

SWNTs, which are produced from a single sheet of graphene, figure 1.2, are not as easy to manufacture and are therefore much more expensive, requiring large specialist equipment. MWNTs typically have a diameter in the range of 10 to 50 nm, and a length upto 10μm [15], whereas SWNTs are much thinner with a diameter of around 1.0 to 3 nm and generally have a length of a few microns. MWNTs can be more appealing than single walled nanotubes due to differences in their properties. MWNTs are physically and electrically more stable [16] than their single wall counterparts. They are less likely to naturally form nano ropes and/or bundles, which exhibit low solubility in water and other organic solvents. Most importantly they are cheaper [17, 18], and easier to produce. However, due to the mainly metallic nature of multiwall nanotubes (MWNTs) [16] they are generally only good for field emission [2], nanowires, vias and other metallic, non-semiconducting, devices. MWNTs are more resistive to chemicals which is important for functionalisation, whereby chemicals are used to modify their properties. When SWNTs are functionalised using chemical methods, it is possible to damage some of the bonds leaving holes in the lattice.

It is worth noting here that there is a third kind of nanotube, the double-walled carbon nanotube (DWNT) although technically a MWNT they display properties which are much more like that of a SWNT but with added bonus of retaining some of the advantages of MWNT such as resistance to chemicals, bundle and rope forming and physical stability. However DWNTs are the most difficult types of nanotubes to manufacture.

SWNTs can have semiconducting (typically p-type) or metallic characteristics, two

known reasons for this are the tube diameter and the tube chirality [3]. The chirality of a carbon nanotube describes the direction in which the graphene sheet has been rolled with respect to the lattice, figure 1.3.

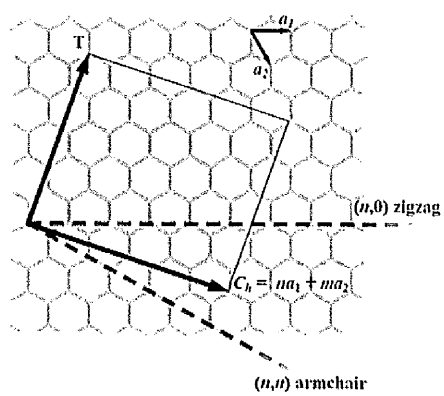

(a)

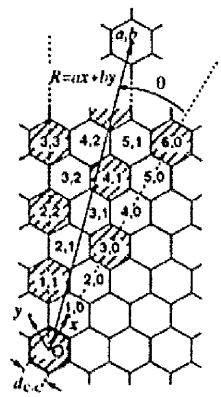

(b) Shaded hexagons represent metallic chiral vectors [19]

Figure 1.3: Schematic describing chirality of single wall carbon nanotubes and the chirality naming convention.

From figure 1.3(b) if when formed the nanotubes are rolled along the vector $2a+b = 3N$ then the nanotube will be metallic, when N is a positive integer, this will mean that the CNT will have no band gap, however if $2a + b \neq 3N$ then the nanotube will have a small band gap and will therefore display semiconducting properties [19]. Where $a = b$ then the nanotube will be rolled into what is known as an armchair chirality, this is due to the lattice looking like an armchair when rolled in this vector. All armchair CNTs will be metallic. These purely metallic nanotubes have been reported to have electrical conducatnces up to $4 \times 10^9 Acm^{-1}$, which is in the order of a thousand times higher than copper [20]. MWNTs generally have a metallic behavior, as the diameter of CNTs increase the band gap decreases, once the diameter reaches 2 nm the bad gap will be zero and therefore the nanotube will be metallic. It has been proposed that using plasma functionalisation it could be possible to dope the MWNTs in order to produce MWNTs with semiconducting properties, therefore producing nanotubes with semiconducting properties but without the difficulty and high costs of producing single walled nanotubes.

Due to the many positive attributes of MWNTs they would make good components in semi-conducting devices. The cost of production of semiconducting devices would be driven down by the inclusion of MWNTs due to the more cost effective methods of production, compared to methods such as CVD [21] and laser ablation [22–24], used to grown SWNTs. On top of this the unique sensitivity of CNTs lend themselves to become ideal integrated sensors. Integrating CNTs into molecular devices such as transistors could allows for changes in the CNTs electrical properties, due to external changes, to be easily detected. This would then open the path for low cost integrated sensors for anything from biomedical applications such as DNA, Glucose, Cancerous Cells to dangerous gas sensing such as carbon dioxide.

Using pyrolytic methods, it has been shown that by doping MWNTs with nitrogen they have shown that it is possible to induce n-type semiconducting properties [25]. This could prove very useful for the development of carbon nanotube transistors and other nano-electronic applications, allowing MWNTs to replace SWNTs. Kai Xiao et al [25] have introduced nitrogen into the carbon nanotubes as donor states to the system and have studied the electronic properties of the N-doped MWNT's at several different temperatures. Their finding showed that using a single multiwall nanotube, field effect transistors (MWNT-FET) can be created which have clear n-type properties and display high mobility. They concluded that nitrogen doped MWNT's have novel electrical properties that undoped MWNT do not have. Again using pyrolytic methods Czerw et al [26] have demonstrated that Nitrogen doping of MWNTs leads to the introduction of conduction band modifications, including a large electron donor state. They reported distortions and gaps within the carbon lattice, which they attribute to the decoration of the nitrogen, figure 1.4. Other common methods of functionalisation has been wet chemical exposure or by exposing CNTs to vapors at high temperatures these techniques have shown changes in chemical or physical properties [27]. Other methods involve the doping of CNTs during the growth of the tube. However these methods, (chemical and pyrolytic) may damage the carbon nanotubes and potentially lead to waste disposal issues [28]. Khare et al [28] have recently attached hydrogen atoms to the sidewalls of SWNT using a glow discharge process. Using this cold plasma process they concluded that plasma functionalisation was a clean, low temperature, simple

method of producing very clear results compared to chemical techniques. Plasmas contain activated species able to initiate chemical and physical reactions when it contacts a surface. As a result, modification reactions at the surface occur and cause alterations of the surface properties and surface morphology [29]. Terrones et al [30] have demonstrated that the N-doping of CNTs lead to the introduction of conduction band modifications (at 0.18eV). The valence and conduction band features are symmetrical around the fermi level (0eV), for pure nanotubes and they suggest that these nitrogen induced states are just above the fermi energy. This electron donor feature is seen everywhere along the straight sections of the nanotubes, fig 1.4.

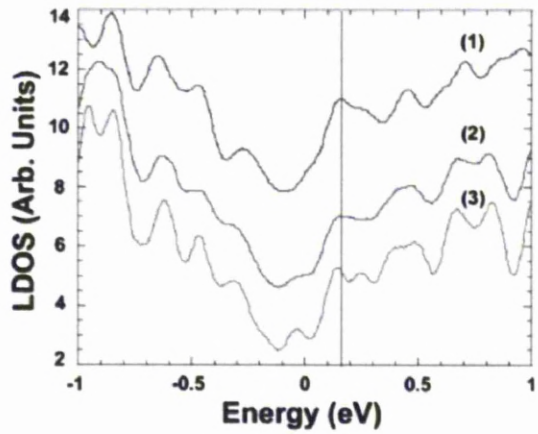

Figure 1.4: Tunneling spectra acquired on a straight and clean section of an N-doped CNT [30]

1.2 Plasma Glow Discharge

Plasmas are partially, or fully, ionised gases and can consist of electrons, both positive and negative ions as well as neutral gas molecules/atoms. Plasmas have characteristics unlike that of gases, liquids or solids and have long been describe as the fourth state of matter. Plasma is the most abundant state of matter in the universe [31], comprising of around 99% of all matter. The majority of which consisting of interstellar mediums, stars, atmospheres, nebulae, etc. Terrestrially plasmas occur naturally in lightning bolts, fire and the aurora borealis. The list of man made plasmas and their applications is an ever growing one, fluorescent lamps, neon signs, arc welding equipment, tesla coils, plasma televisions, plasma etching devices, fusion research, to name a few.

A simple Plasma discharge can be initiated simply by applying an electric field across a gas which is below atmospheric pressure. This field then excites electrons within the gas (or from the electrode) and causes the gas to ionise and produce plasma, once enough gas particles are ionised then a current will flow between the electrodes through the plasma. The voltage at the point at which current begins to flow is known as the breakdown voltage, and is dependent upon the electrode separation, the pressure of the gas, and the gas being used. Once this point has been reached the atoms within the gas break down, to allow the electrons and positive ions to move freely. For plasmas in thermal equilibrium, such as stars, $T_e = T_i$, were is T_e and T_i are the electron and ion temperatures respectively, were the notation temperature is used to describe the particles velocity distribution, and ion and electron densities are approximately equal, $n_e \approx n_i$. As $n_e \approx n_i$ the plasma is on average electrically neutral, however over very short distances this is not always the case. Over a distance of what is known as the Debye length the plasma may no longer be neutral. This is the length in which the electrons redistribute themselves to shield the plasma from any charge density inequality, also known as debye shielding.

In weakly ionised plasmas, such as those used in this work, it is a more accurate to assume that neither of the charged particles are in thermal equilibrium. In this scenario $T_e >> T_i$, this is due to the energy being preferentially applied to the electrons, whilst the heavier ions exchange energy with the background gas via collisions [32]. Due to $T_e >> T_i$ it is the electrons that disassociate the molecules in the gas to generate

free radicals as well as causing ionisation. However T_e is often lower than the energy required for ionisation but due to the distribution of energy a small number of electrons will have sufficient energy, [31] [32], [33].

Figure 1.5 displays the large range of plasma density of a variety of plasma types from interplanetary plasma to laboratory controlled experimental plasma. The plasmas used within this work fall within lower end of the non thermal low pressure discharge region.

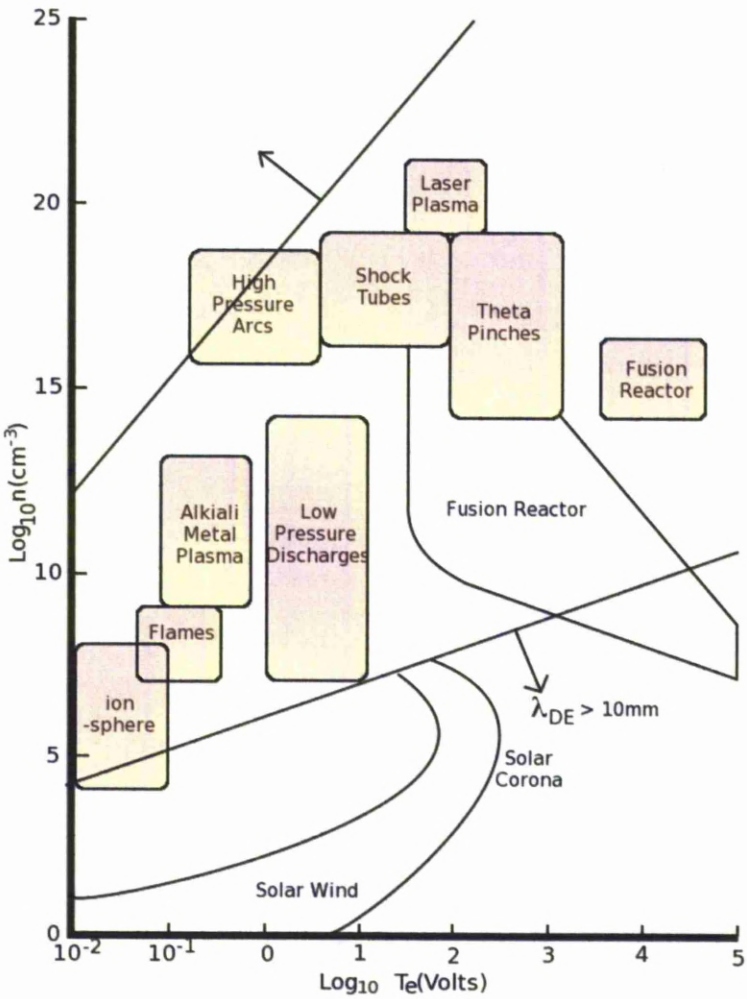

Figure 1.5: Plasma Temp Vs Density for a variety of plasmas [32]

As mentioned $T_e >> T_i$, however it is the ions that perform much of the surface bombardment this is due to the acceleration of the ions across the sheath. This plays

the most important role in surface modification/implantation this acceleration means that although the ion temperature in the bulk can be much lower than the electron temperature ions arriving on the surface can have temperatures orders of magnitudes higher than the electron temperature. Sheaths within the plasma occur at surfaces between objects in the plasma and the plasma. Due to the ions having lower energies than the electrons, they are lost too the objects faster thus leaving the plasma with a positive charge and therefore this would mean that the object would have a negative charge with respect to the plasma. This positive charge in the plasma falls off very rapidly towards the object surfaces, figure 1.6. Due to what is know as deybe shielding, this negative charge cannot be maintained across the entire plasma and therefore a sheath forms with is a number of deybe lengths in thickness.

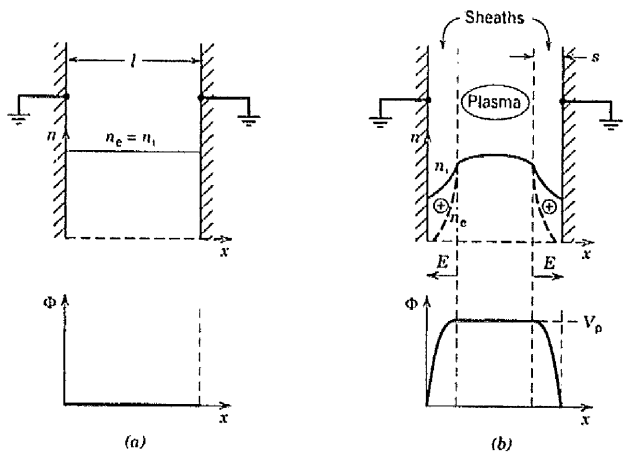

Figure 1.6: Plasma density and potentials across the plasma a) initial condition b) after sheath formation [32].

Debye shielding is the process in which the plasma shields out electric fields. Considering a charge inserted into the plasma it would attract an number of oppositely charged particles, in a sheath around the charge, and therefore would repel an equal number of same charged particles. A polarisation field is produced balancing the disturbing electric field (due to the displacement of the opposite charged particles). If no thermal motion was present then this field would produce an ideal shielding effect, whereby the charge is contained and no electric field would be present in the bulk plasma. However this is not the case and therefore particles on the edge (where there is a weaker field) of the sheath may have the thermal energy required to escape. The

edge of this sheath must now be redefined as the point were the potential energy is equal to the thermal energy. The shielding distance is known as the debye length, this is defined as

$$\lambda_D \equiv \left(\frac{\epsilon_0 K T_e}{ne^2}\right)^{1/2} \tag{1.1}$$

Where λ_D is the Debye length, KT_e is the thermal energy, ϵ_0 is the permittivity of vacuum, n is density and e is the charge on an electron.

1.2.1 RF Glow Discharge

To reach the plasma state, energy for the ionization of the atoms, and molecules, must be input into the system, from an external source. The most common methods of supplying the gas with energy is Direct Current (DC) or Alternating Current (AC). Alternating current can be administered either by; capacitive coupling, or inductive coupling. For this work a capacitively coupled AC current of radio frequency (RF) 13.56Mhz was used. When a time varying voltage is applied to the driven electrode electrons in the Nitrogen gas react to the varying voltage and gain energy. When the RF power exceeds a certain value the discharge ignites, as explained earlier. This value is dependant on the pressure, geometry of the electrodes and the gas used. For example, the breakdown power required for N_2 plasma in the vacuum system described in chapter 2.1, with a 60mm plate separation at a pressure of $1x10^{-3}$mTorr will be approximately 5 Watts, providing it is tuned. After breakdown the gas will become electrically conductive and will start emitting light. The power and pressure required for break down of the gas in an RF generated plasma is generally lower than those needed when using a direct current method [33].

In low temperature plasmas the required energy to ionise a atom is only possessed by the small number of electrons in the higher energy tail of the distribution. However this number of electrons can be increased due to the RF field effect. As the RF field increases the electrons accelerate to their maximum positive velocity and then as it decreases they are decelerated to their maximum negative velocity and so on as the cycle continues. If an electron where to be reversed due to a collision with a heavier

particle just before the reversal of the electric field then the electron would be able to attain an energy which would surpass that of the energy required to ionise a neutral particle. Giving a larger number of electrons which have the required energy to ionise the gas.

The value 13.56Mhz is an arbitrary value that has been allocated for plasma research, along with the first few harmonics. However this driving frequency must be large enough so that the substrate would not have time to 'extinguish' the plasma. RF plasma has been selected for this sudy due to the ability to place insulating materials on the substrate for processing. In a DC discharge a insulating material on the substrate would rapidly charge to the potential of the opposing electrode preventing current flow and consequently the plasma would go out. In a RF powered plasma this would not happen as the insulator would be subjected to alternating fields, preventing charge build up. As mentioned earlier when opposite charge particles are displaced electric fields are created, which produces a restoring force on the displaced particles. The time taken in an RF plasma for the charged particles to reach their equilibrium positions is dependent on their masses, and as the restoring force is proportional to their equilibrium position the particles oscillate, by what is known as the plasma frequency which is given by for ions.

$$\omega_{pi} = \left(\frac{e^2 n_i}{\epsilon_0 M}\right)^{1/2} \tag{1.2}$$

and by substituting n_i for n_e will give the plasma frequency for the electrons, therefore the natural frequency of the plasma can be given as

$$\omega_p = \left(\omega_{pi}^2 + \omega_{pe}^2\right)^{1/2} \tag{1.3}$$

again due to ions only reacting to time average potentials and electrons responding to instantaneous potentials it must follow that;

$$\omega_{pi} < \omega_p << \omega_{pe} \tag{1.4}$$

and therefore the ion plasma frequency must be below the applied RF to allow for the condition explained earlier where the insulated surfaces on the electrode do not extinguish the plasma.

The behaviour of the sheaths within an RF plasma are different to those in a DC discharge. As the applied voltage is constantly changing the electrons within the plasma respond to the instantious electric fields and oscillate back and forth. However the less mobile ions respond to the time averaged electric fields. Due to this oscillation sheath regions appear around both electrodes which contain a net positive charge, when averaged over the period. Producing a strong (time averaged) electric field within the sheath from the plasma to the electrodes. The variation in mobility between ions and electrons means that ions are continually lost to the electrodes whilst electrons are only lost at the point in the cycle when the sheath collapses into the electrode. This in turn means that the discharge nearly always has a positive charge with respect to the electrode (and wall), except in the instant were electrons do escape to the electrode. The driven electrode also adopts a mean potential that is negative with respect to the opposite electrode whilst still oscillating due to the applied RF. That is to say that the RF potential oscillates around what is known as the DC self bias potential as shown in figure 1.7 as the red line. The plasma ability to self bias is one of the most important aspects of an RF plasma, this RF self biasing establishes itself within a few RF cycles after the gas breakdowns.

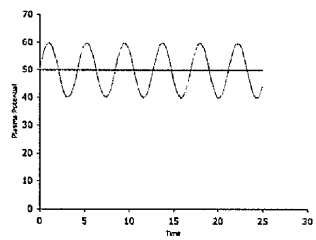

Figure 1.7: Exaggerated example of how the RF potential oscillates around the DC potential.

It should be noted that the self bias potential is close to the DC floating potential when there is only a small amplitude driving RF but the self bias potential is approximately equal to the driving RF when there is a large applied amplitude [34].

1.3 Plasma Modification of Carbon Nanoparticles

Recently A. Felten et al [35] published a paper detailing three types of plasma functionalisation. Using radio-frequency plasma they functionalised MWNTs with O_2, NH_3 and CF_4. The MWNTs that they used in the study were commercially available and were not purified, meaning that approximately 40%wt of the powder is made up of amorphous carbon and catalyst particles. The plasma treatments were carried out at 13.56MHz with powers between 10 and 50 watts, at a pressure between 0.05 and 0.6 Torr and with an exposure time between 15 and 1200 seconds. In order to determine the chemical changes at the nanotube surface x-ray photoelectron spectroscopy (XPS) was used. They found that, for the ammonia treatment, the nitrogen concentrations increased with increasing exposure time and plasma power. They concluded that varying distinct plasma parameters can lead to different reaction products and give the possibility to fine tune the relative occurrence of different functional groups on the MWNT surface.

Yan Bingyong et al, [3] functionalised MWNT's prepared on a Ni Cr/Si surface with Argon. Although their aim was different to A. Felton [35] the process was similar. The argon plasma treatment was carried out for 2, 5 and 10 min, with a gas flow of 10sccm, a pressure of 100mTorr and an RF power of 60W. The surface of the MWNT was then examined using scanning electron microscopy (SEM). Within their results they found that after treatment the previously randomly oriented arrays of MWNT which where tangled became straighter at the stems of the MWNT's. Chirila et al, [36] have also recently functionalised CNT with oxygen in RF and Microwave plasmas using similar methods and parameters. Although they do not state what type of carbon nanotubes they used, they were successfully able to increase oxygen containing groups on the surface by up to ten times.

Plank et al [37, 38] have functionalised SWNT with fluorine using SF_6 and CF_4 plasmas. Using an reactive ion etcher they functionalised bucky papers on top of PTFE membranes in a dc plasma biased at 300v with varying gas flow and pressure. They have recently taken plasma flourinated SWNT's and have functionalised them with 1,2-diaminoethane in order to produce n-type SWNTs [39]. Once functionalised, nanotube transistors where produced from silicon (with Au/Ti source and drains with

25/5nm respectively) and the SWNT spun cast on top of the source and drain. The transistors were then analysed using a probe analyiser. They state that these devices show decreased conduction, a sign of the first stage of n-doping.

1.4 Summary

It has therefore been put forward that plasma functionalisation is implemented; using a capacitively coupled RF Plasma generated using parallel plates. Plasma properties are monitored and altered in order to vary the characteristics of the MWNT transistors. Growth of nanotubes in LN_2, H_2O and a H_2O C_2H_6 mixture is also be investigated. Molecular electronic devices have been constructed using the CNTs and RF modification of the CNTs will allow us to modify the electrical characteristics of the tubes in order to create improved junctions between the MWNT and the source and drain. Modification to the CNT properties should allow the charge through the CNTs to be regulated in order to produce devices with higher motilities. Various techniques, such as TEM, FTIR and electrical measurements have been employed in order to characterise the CNTs before and after exposure to the plasma.

This chapter has provided an introduction to both carbon nanotubes and plasma discharges needed for this study. A more detailed introduction to these topics can be found in the following books; Tanaka, [19], Endo [40], Lieberman and Lichtenberg [32], F. Chen [31], Goldston and Rutherford [41] and Chapman [33].

Chapter 2

Experimental Techniques

2.1 RF Plasma System

In order to perform functionalisation of carbon nanotubes a purpose built plasma rig has been designed, constructed and characterised. The vacuum chamber has five main ports, arranged in a cross in the XY axis with the 5th in the Z axis, all ISO 160, figure 2.1. The right hand port is connected to a turbomolecular pump through a baffle and a 90° elbow. The top and bottom ports are used for feedthrough to the electrodes (with the bottom port also used for mass spectroscopy). The left hand port contains pressure gauges, gas inputs and a probe feedthrough which allows for various probes to be fed into the chamber. The front facing port is a full size viewing port, protected by a folding shutter system. A local gas bottle is secured directly onto the rig and flow rate controlled using mass flow controllers and needle valves. The main chamber has an internal volume of 8ltrs and a surface area of approximately $0.21m^2$. With all the flanges blanked off a base pressure of $1x10^{-5}$ mbar is achievable in 2 hours. With the rig in the configuration that is used for experiments a base pressure of $2x10^{-5}$mBar can be achieved in the same time. With bake out at around 70 to 80 °C for roughly 4 hours a base pressure of $1x10^{-5}$ mBar can be reached. An overview of the basic system can been see in figure 2.1. Gas flow is from left to right through the chamber via a gate value to the pumps.

A nitrogen plasma is generated using two parallel plates an an RF power supply to produce a capacitively coupled RF plasma. Mounted so that the faces of the plates are horizontal allowing the samples to be placed directly onto the bottom plate. The plates have been designed so that they are both insulated from the chamber allowing

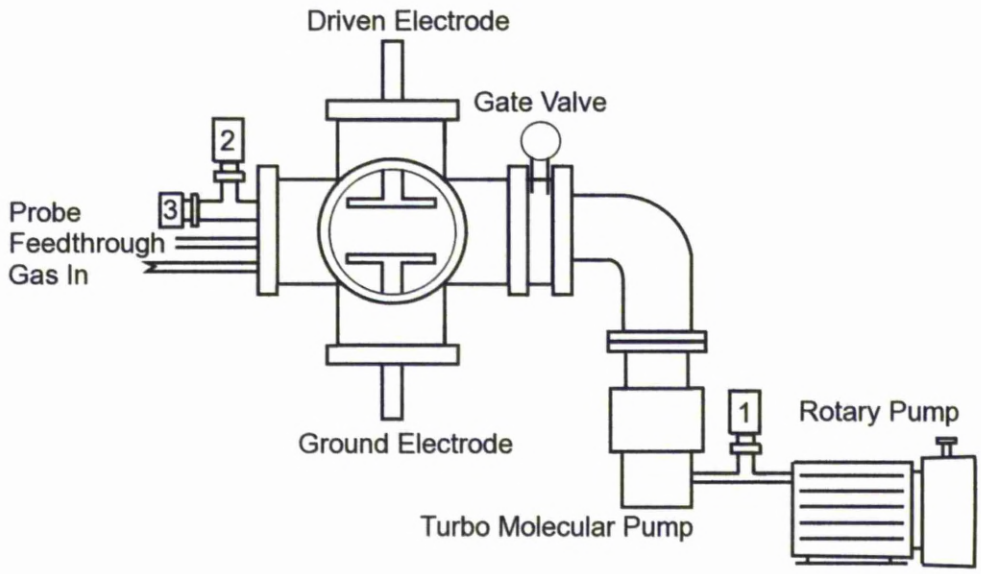

Figure 2.1: Schematic of the vacuum system.

any number of electrical configurations, meaning samples can be placed on either driven or grounded electrode depending on the configuration. Figure 2.2 shows a schematic of the typical setup, where the lower electrode is grounded and the higher electrode is driven. Each plate is 145mm in diameter with a variable separation of 0 to 250mm.

Due to the size of the chamber plasma discharge was originally observed both between electrodes and between the chamber walls, this problem was resolved by placing a shield over the driven electrode. The shield is constructed of a PTFE stand off 2 mm thick and a grounded stainless steel covering. As the walls of the chamber are connected to ground the discharge produced is asymmetric. The RF power is supplied by a Coaxial Systems with a maximum output of 150 Watts, along a coaxial cable through the matching circuit to the driven electrode. In order to maximise the power transfer through the system an impedance matching circuit is required. Impedance matching maximises the power transfer by reducing the reflections within the system.

This matching unit is a L type LC network consisting of two variable capacitors and one fixed inductance, figure 2.3. This compensates for reflections along the power line

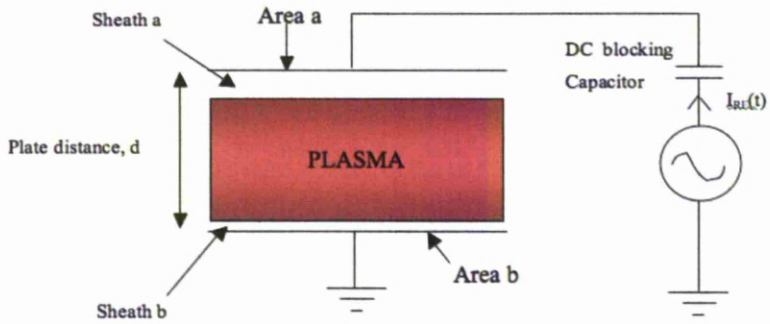

Figure 2.2: Schematic of the plasma system.

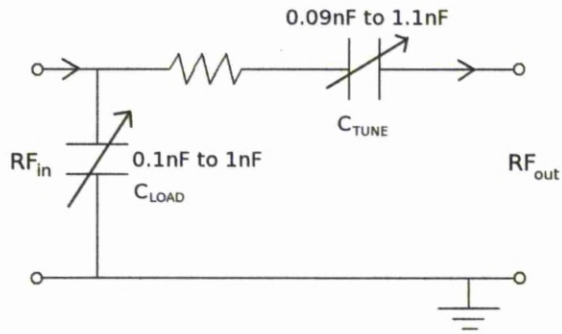

Figure 2.3: L type matching network, use to maximise power transfer by minimising reflections within the system.

and for phase changes between the resistive power supply and the capacitive RF plasma. The power at maximum efficiency will be transferred when the impedances are complex conjugate matched throughout the system, from the transmitter output, through the coaxial cable (which can be represented using a equivalent transmission line circuit), to the plasma (the load). For maximum power, Zload = Zsource* (where * indicates the complex conjugate). When the impedances are not matched standing waves on the transmission line will occur due to reflections. Measurements for electrical diagnosis, current, voltage and phase, can be taken using an in line box, described on the next page, which is placed as close to the driven electrode as possible and provides access to the cable for line current and voltage measurements to be taken. Measurements were taken using a Tektronic P5100 current probe and a high voltage Tektronix P6015A

voltage probe connected to a Tektronic TDS 3014 oscilliscope.

Figure 2.4 shows the complete system setup in the laboratory, this is the standard setup used to do functionalisation, probe diagnostics and electrical characterisation of the plasma. Not shown in the picture are the three pressure gauges, a pirani gauge is installed between the rotary pump and the turbo pump, the second is a Leybold ITR 90 wide range pressure gauge and a high range MKS pressure transducer, labelled 1, 2 and 3 respectively on figure 2.1.

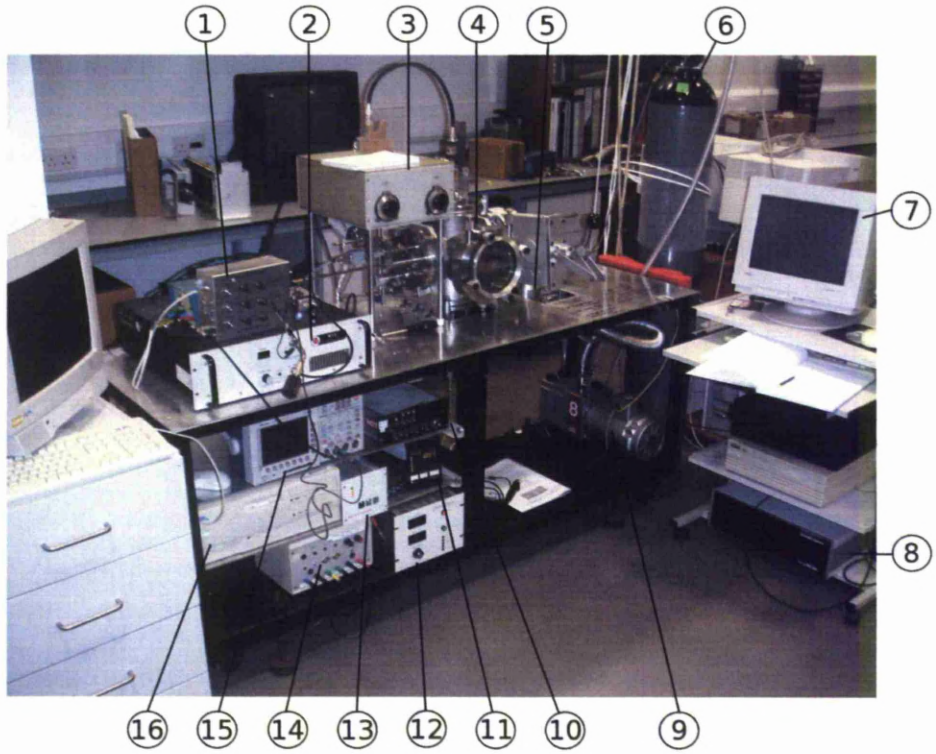

Figure 2.4: Photograph of the vacuum system.

1	Langmuir compensation phase shifter
2	Langmuir compensation amplifier
3	Main matching unit and blocking capacitor
4	Main chamber
5	Turbo Molecular pump, BOC Edwards EXT 70
6	Nitrogen gas bottle
7	Smart Probe computer
8	Smart Probe system for langmuir measurments
9	Rotary Pump, BOC Edwards No 8
10	Gas flow controller
11	Chamber pressure readout
12	RF Power supply
13	Turbo Molecular pump control unit
14	DC Power supply
15	Oscilloscope
16	Main computer

The setup for the RF excitation of the gas is a capacitively coupled RF discharge where two electrodes are mounted vertically into a vacuum chamber (figure 2.1). The plasma used for the functionalisation will be a low pressure, non thermal plasma, with the top electrode driven and the samples placed on the bottom electrode.

An in line box has been designed to allow line current and voltage measurements to be taken. It is simply a box that allows access to the cable whilst keeping it and the measurement equipment shielded.

The various control parameters must be know to determine the plasma properties. These control parameters include frequency, driving voltage, power, plate distance, and gas pressure. This will then allows calculation of the plasma properties which in turn will allow for the control parameters to be varied to produce the desired plasma properties. An image of the plasma can be seen in figure 2.5.

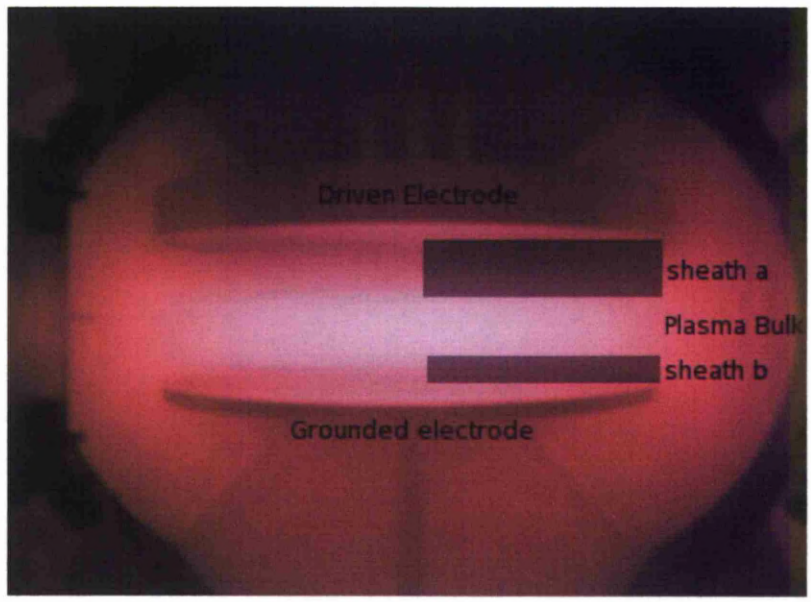

Figure 2.5: Image of RF plasma at 10mTorr, 10 Watts with an electrode separation of 6cm

2.2 Langmuir Probe

The langmuir probe is a small metal intrusion into the plasma which is biased, with respect to the plasma potential, to draw electron/ion current. The drawing of current from the plasma to determine plasma parameters was first studied by Mott-Smith and Langmuir during the 1920's [42]. The langmuir probe is surrounded by a sheath much like any electrode, however due to its small size it does not perturb the plasma [32], if it were the probe would then act as an electrode altering the plasma properties and giving inaccurate results. This is of paramount importance when trying to determine local plasma parameters. A basic probe setup is shown in figure 2.6, using this configuration a typical I-V characteristic should be obtained, shown in figure 2.7.

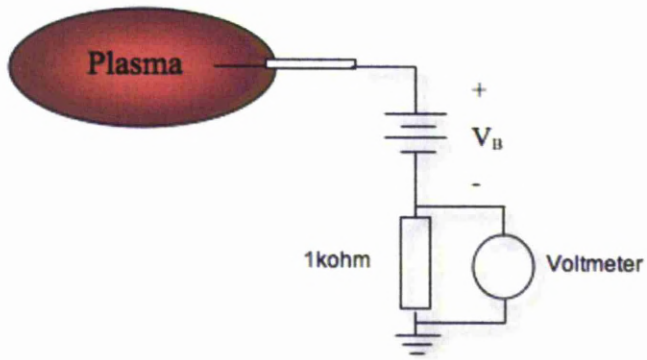

Figure 2.6: Basic langmuir probe setup

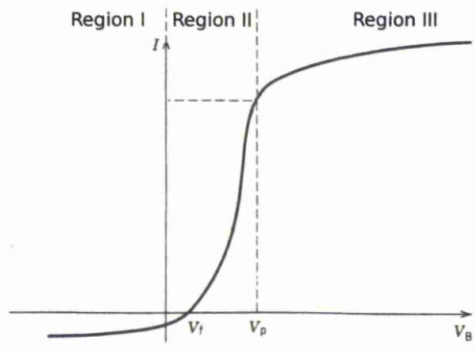

Figure 2.7: Typical langmuir probe characteristic [32].

The typical I-V characteristic acquired through a langmuir probe allows calculation a number of local plasma parameters. Examining figure 2.7, when V_B (the bias applied

to the probe) is less than V_f, region I, electrons are repelled from the probe sheath and therefore the current drawn is mainly ion current, this is said to be a negative current flowing out of the plasma into the probe. V_f is the floating potential of the plasma, at this potential an insulated probe that cannot draw current will float [32], the electron and ion currents are equal due to the probe being sufficiently negative compared to the plasma. Between V_f and V_p, region II, the electrons are repelled due to what is known as the boltzmann relation. The boltzmann relation is given by

$$n_e = n_o e^{\phi/T_e} \tag{2.1}$$

where n_o is the area density. At V_p, Region III, the probe and plasma are at the same potential, at this point there is no sheath around the probe. The probe draws current only from the electrons giving a positive current from the probe to the plasma, this is due to the much larger electron velocity than ion velocity, $\Gamma_e >> \Gamma_i$. This positive current is known as the electron saturation current I_{esat} after this point (i.e. V_B is greater than V_p) the current drawn saturates with a dependance of the probe geometry.

It is also possible to obtain electron temperature and density (T_e, n_e) from the curve using simple probe theory. The electron temperature is calculated by measuring the current at V_p and dividing it by the integral of the langmuir probe curve from V_f to V_P.

$$\frac{1}{kT_e} = \frac{I(V_p)}{\int_{V_f}^{V_p} I(V)dv} \tag{2.2}$$

once T_e has been calculated n_e can then be found from the electron saturation current I_e.

$$I_e \approx \frac{1}{4} A_p n_e e \sqrt{\frac{8kT_e}{\pi m_e}} \tag{2.3}$$

The probes used during this work were designed and constructed in house. The probe is designed in the style of a cylindrical Langmuir probe. It consists of two main parts, as shown in figure 2.8, the stem and the tip, this two part design allows for various probe configurations using the same probe stem.

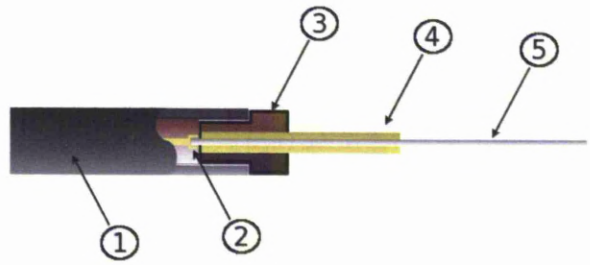

Figure 2.8: Langmuir probe, 1: Probe Stem, 2: Socket connector, 3: Ceramic tip holder, 4: Tungsten probe tip

The stem of the probe consists of a 1/4" steel tube, shown in figure 2.9, with an electrical feed through which is solder sealed to maintain the vacuum. The other end of the probe consists of a recessed ceramic socket. The socket is recessed by 5mm for two reasons, firstly it shields the connection between the stem and the tip from the plasma and secondly it provides support for the tip. Insulated copper wire connects the electrical feed through to the socket inside the tubing. A feed through was designed for the vacuum chamber so that the probe, shown in figure 2.9, had the capability to be moved back and forth, coupled with the ability to move both plates up and down allows probe measurements to be taken at any position within the plasma. The probe tip is constructed of a copper plug which is connected to a tungsten wire, of 0.5mm in diameter which forms the collection surface. This is encapsulated in ceramic which fits inside the recess of the probe stem. The tungsten wire protrudes out of the ceramic encapsulation by 15mm. Tungsten was selected as it has a low secondary electron emission coefficient, this can be further minimised by keeping the probe surface area low. The use of a small probe tip is also advantages as the larger the collection area the larger the current drawn. Drawing larger current from the plasma can directly effect the shape of the I-V characteristics by rounding the curve around the plasma potential. As the probe stem is grounded it is important that the probe tip holder is electrically insulated as not to draw current from the plasma, for this reason it is constructed of ceramic and is of a length so that it may be placed in the plasma without the grounded stem drawing current. The probe tip used is 15mm in length which is greater than several deybe lengths, so that the collected current is not affected by any current that maybe collected by the holder. It is also important that the probe is

positioned perpendicular to the electric field in order to minimise distortions.

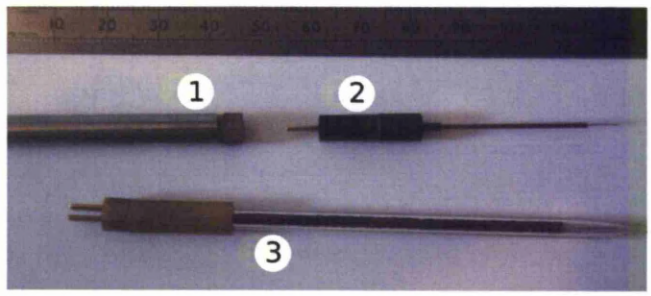

Figure 2.9: 1) Probe stem, 2) Langmuir probe, 3) Capacitive probe

2.2.1 Orbital Motion Limited Theory

General Langmuir probe theory was discussed in section 2.2 however this is an ideal case and in reality other considerations must be taken into account. Orbital Motion Limited (OML) theory allows for the effects of a cylindrical probe within the plasma.

Ideally the current drawn would remain constant after the bias potential reaches the electron saturation current, this however is only the case when considering a planar probe. The probes used within this work are not planar but are cylindrical, due to their wire construction, it is important to consider how the current my be limited by the orbital motion of ions collected by the probe. A cylindrical probe will continue to collect more current with increasing bias due to the increase in effective collection area [32], figure 2.10 shows how the variation in probe shape moves the curve away from the ideal characteristic. It can be seen here that as the probe bias increases the knee of the I-V characteristic becomes less distinct as the probe shape moves away from being planar, this is due to an increase in the effective collection area of the probe, figure 2.10. However a planar probe will too have a small increase in effective collection area due to sheath effects at the edges of the probe, and thus will show a slight increase in the saturated current unlike the 'theoretical planar probe'. In order to understand the variance in the electron collection it is important to consider the motion of particles approaching the probe surface, figure 2.11 shows the motion of an ion approaching the surface of the probe.

The figure 2.11 shows how various ion trajectories are affected by the probe potential. Path one is known as a pass by trajectory, this type of ion path does not influence

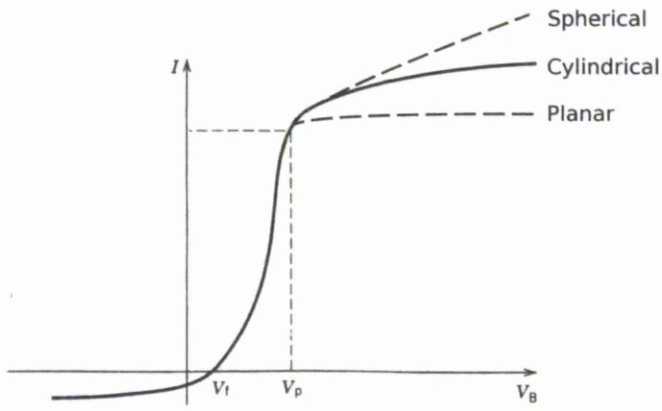

Figure 2.10: Change in Langmuir probe shape due to shape of probe tip, (note: exaggerated for illustration).

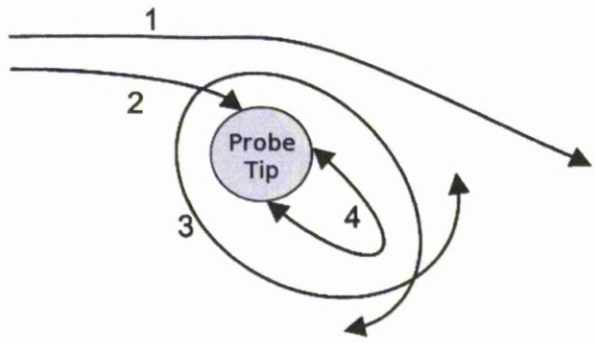

Figure 2.11: Ion trajectories around the probe tip, front view. [43]

the probe current. Path two describes any trajectory that approaches from infinity, ions are drawn to the probe and contribute towards the OML current. The third path does not contribute towards the current. The forth path is a trapped ion generated by the probe and does contribute to the current [43]. OML suggests that the collected ion/electrons have a velocity that is at a tangent to the probes surface. However a number of assumptions are made in order for OML to hold true. Firstly the plasma is assumed to be in non equilibrium i.e. $T_e > T_i$ and that it is quasi neutral, $n_e \quad n_i$ and that the electrons have a maxwellian energy distribution [42]. It is also assumed that the probe radius is less than the ion (and electron) mean free path. The probes used in this work were designed in such away that the diameter of the probe tip was less than that of the ion mean free path allowing for OML theory to be valid.

2.2.2 RF Compensation of a Langmuir Probe

The langmuir probe analysis presented thus far only applies when operating with a DC plasma, in order to apply these analysis techniques to an RF Plasma a number of considerations need to be taken into account. The probe tip in the plasma is modulated by the RF (and it's harmonics), that powers the system. This results in RF self-biasing which, time averaged, causes the characteristics to become skewed, figure 2.12. As such the standard DC langmuir probe theory cannot be directly applied [44]. It has been shown that this RF modulation prevents the probe from drawing current when it is self biased [45, 46].

The effect of this distortion on the langmuir probe results is to produce high values of electron temperatures and lower values of plasma densities. This problem can be rectified by compensating the probe. Compensation forces the probe to follow the RF oscillations in the plasma so that the plasma appears to be DC from the reference point of the probe. This then allows for analysis using traditional DC Langmuir probe theory. To do this there are two commonly used methods, the first is active compensation. A RF signal is applied to the probe tip, the signal is generated from a trigger which either comes from the plasma or the power supply. This RF applied to the probe must be both matched in amplitude and phase to the plasma and it's harmonics in order for it to efficiently cancel out the effects of the RF [47], [48]. The second is know as a

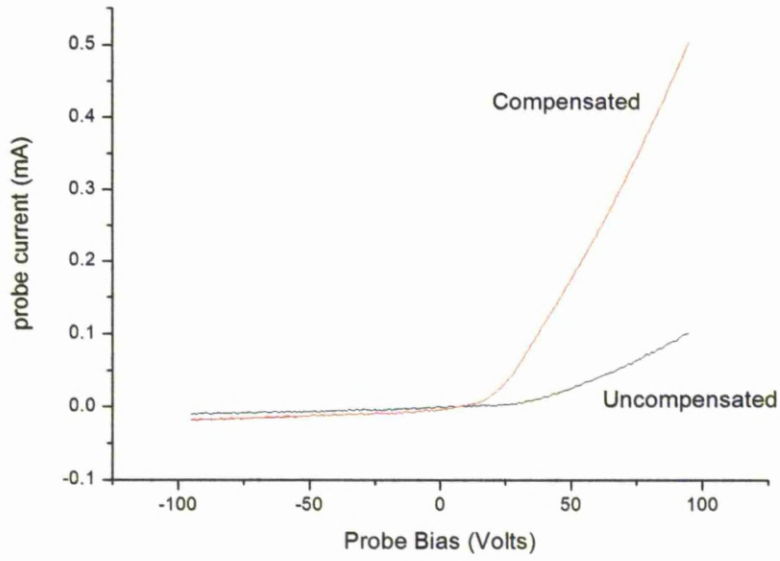

Figure 2.12: Uncompensated langmuir probe I-V curve (black) compared to compensated langmuir probe (red)

passive probe. This method has a feedback loop built into the probe so that the tip is driven directly from the plasma variation. This type of compensation involves serveral LC ciruicts so that there is no RF drop across the sheath. For the work presented here an actively compensated langmuir probe was used such as that described by A Dyson et al [49]. Active compensation of Langmuir probes has been reported by N. Braithwaith et al [48] and A. Dyson et al [49] for up to the third harmonic component. This three harmonic matching is achived using a number of phased locked loops which when locked to the harmonic allow generation of two additional harmonics with variable phase and amplitude. The active compensation used here consists of two components. An aux output from the RF power supply, running at the same frequency and phase as the main output, is connected to a three harmonic phase matching unit. Dyson et al, provide excellent detail on the construction of this harmonics box [49]. The combined three harmonic signal is then passed through a high performance RF amplifier, a M75 by IFI 0.01 to 230 Mhz up to a maximum of 75 W, this allows for fine adjustment of the amplitude to precisely cancel out the RF component across the probe sheath.

Uncompensated langmuir probe measurements were taken in the plasma system to

observe the effects of not compensating the probe, and an example of which can be seen in figure 2.12.

Once uncompensated resuts had been taken compensated results where taken following the compensated method shown by A. Dyson et al [49]. The DC bias voltages where supplied by the Smart Probe langmuir probe system (scientific systems) the software hardware combination allows for control over the parameters and recording of data on a PC. In order to operate the Smart Probe analytical hardware and software an RF choke must be placed in between the probe and the Smart Probe input. The RF Choke and DC filter serves two purposes, firstly it filters the RF from the Smart Probe system and secondly it filters the DC from the Phase shifter, protecting each device from the other. A simple butterworth filter was designed and built over a basic LC circuit in order to improve performance of the RF choke and DC filter. The same parameters as those used in the electrical characteristics were varied for compensated langmuir probe I-V characteristics.

2.3 Capacitive Probe Plasma Analysis

The RF oscillation of the plasma potential, Vp(RF), can be measured directly by use of a capacitive probe, as well as being inferred by measuring the RF waveforms applied during langmuir compensation. The method used in this experiment is the same as that from a number of other studies [34, 50, 51]. The capacitive probe (figure 2.13) consists of a glass tube with an external diameter of 4mm and a length of 70mm. The tube contains a coaxial cable which is shielded for the majority of the length of the tube, leaving a unshielded 8mm tip exposed, this will act as the pick up for the RF waveform. The probe tip can be seen in figure 2.9.

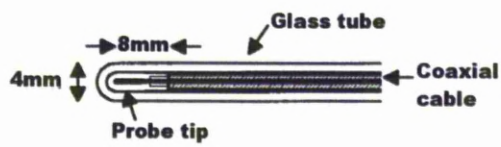

Figure 2.13: Capacitive probe

The probe underwent calibration, a copper braid was placed around it and an

known signal applied. This gives rise to current flow in the unshielded probe tip which is detected by an oscilloscope. A 50Ω input termination was used to reduce the effects of standing waves along the coaxial cable. The power and frequency of the applied signal was varied and the output recorded. This type of calibration can not take into account the capacitance of the RF sheath around the probe, as such the capacitance of the probe is designed to be much greater so that the probe sheath capacitance can be neglected. However due to limitations of the applied signals it is only possible to calibrate the probe up to the sixth harmonic. This allows the time varying plasma potential ($V_p(t)$) to be expressed as

$$V_p(t) = \left(1 + \frac{1}{i\omega R_{in} C_p}\right) V_{in}(t) \tag{2.4}$$

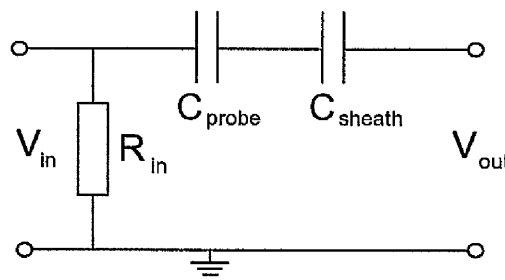

Figure 2.14: Capacitive probe equivalent circuit

2.4 Mass Spectrometry

In order to understand the interactions between the plasma and carbon nanotubes it is important to identify the particles and their associated properties arriving at the nanotube surface. Energy resolved mass spectrometry was used to analyse the plasma parameters, such as V_p (plasma potential), ion energy and ion species at the grounded electrode. The mass spectrometer sorts the ions by applying a number of electric fields to them as they travel towards the sensors, separating them out by mass as they travel. This data is then displayed on a computer allowing analysis of ion properties.

The mass spectrometer used in this work is a Hiden Analytical EQP300, figure 2.15, it is designed for energy and mass analysis of ions, neutrals and radicals generated in plasmas or for secondary ion mass analysis (SIMS). It allows detailed analysis of mass spectra, energy spectra of positive/negative ions, radicals and neutrals. In order to perform these tasks almost twenty electrodes and lenses can be adjusted to improve accuracy and performance. Whilst the EQP300 is capable of residual gas analysis (RGA) it has only been implemented occasionally. The EQP300 utlilies a quadrupole mass selector, this consists of four circular rods, set parallel to each other. This quadrupole mass analyser is the component of the instrument which filters the ions, based on their mass to charge ratio (M/e).

Each opposing rod pair is connected together electrically to form a positive pair and a negative pair of rods. The positive pair has a RF voltage superimposed on a positive DC voltage, while the negative pair has a negative DC and RF voltage that is 180 degrees out of phase with the positive pair. i.e. rods 1 and 3 would be $V_{DC} + V_0 cos\omega t$ whilst 2 and 4 $-(V_{DC} + V_0 cos\omega t)$ Ions move at uniform speed between the rods along the filter axis, for a given set of voltages, all ions below a given mass are neutralised on the positive set of rods, while larger ions are passed. The negative set of rods allows low-mass ions to pass and neutralises any ions above a set mass. This means that by adjusting the RF to DC ratio, the pass bands of each pair can be altered so that only ions of a very specific mass can pass while all others are neutralised or 'filtered'. For this system the driving frequency of the potential applied is fixed so in order to alter the mass 'pass band' the $\frac{V_{DC}}{V_0}$ ratio is altered.

The Hiden EQP mass specrometer has a mass maximum resolution of 0.35nm, and can resolve particles up to 300amu, and has an energy range of $\pm$ 100eV. In order to achieve this the twenty electrodes (lenses) must be re-tuned when; the energy in the plasma is altered, ion mass/energy interest changes, changing the gas, or any alterations to the system/mass spectrometer occur. Therefore once a mass/energy has been selected the system must be re-tuned. The tuning can be broken down into five sections, Extraction, Sector, Quad, Detector and Source. The large array of lenses which are available to tunemo the EQP200 must be turn regularly and carefully. However most of these lenses can be auto-tuned around a chosen ion energy from within the

EQP software. Problems can arise with inaccurate tuning, a slight variation in any of the lenses can produce inaccurate IEDFs. It is therefore important to dedicate large amounts of time to ensure accurate tuning. One method of producing accurate results is to vary the tuning parameters for each energy of interest until the maximum amount of counts is achieved, it can then be assumed the ion loss due to the system is at a minimum.

Figure 2.15 displays a cross section of the mass spectrometer the ion entrance is to the left where extraction takes place. This involves the first two electrodes, extractor and lens 1 as these are the first electrodes which ions encounter they are critical for plasma measurements. Although not usually used for RGA they can reject any externally generated charged particles. Sector, this section includes; vertical, horizontal and DC quad which form the quadruple lens, while plates, transit energy, axis and lens 2 govern the voltages of the energy filter. Energy is the main variable in this section with little adjustment required in the DC quad and no adjustment in the energy filter. Focus 2, resolution, delta m and suppressor are all contained in the Quad section, however Focus 2 and suppressor are not available for tuning whilst the other two allow for fine tunning of the resolution of the machine. The final section for plasma analysis is the dectector, it is crucially important that this section is tuned correctly as incorrect tuning can reduce the life cycle of the machine. The RGA only source section contains emission electron energy and cage electrodes, correctly setting these variables will allow effective use of the RGA mode. As the ion entrance to the spectrometer is grounded all IEDFs are referenced to ground.

The EQP 300 is situated in a vertical orientation so that the orifices is in the centre of the grounded electrode, this is shown in figure 2.17. This will give the most accurate representation of the ion bombardment at the carbon nanotube surface.

The orifice is a 0.1 mm hole in a 2 mm thick plate, beyond this point is the extractor and lenses as mentioned earlier the tuning of these lenses is crucial to the extraction of ions from the plasma. The EQP 300 is isolated from the main vacuum system having it's own pumping system where the orifice acts as a small leak. The equipment has a safe operating pressure of 10^{-6}Torr and has measures in place to prevent it from running above this pressure. The external casing of the system is grounded by being

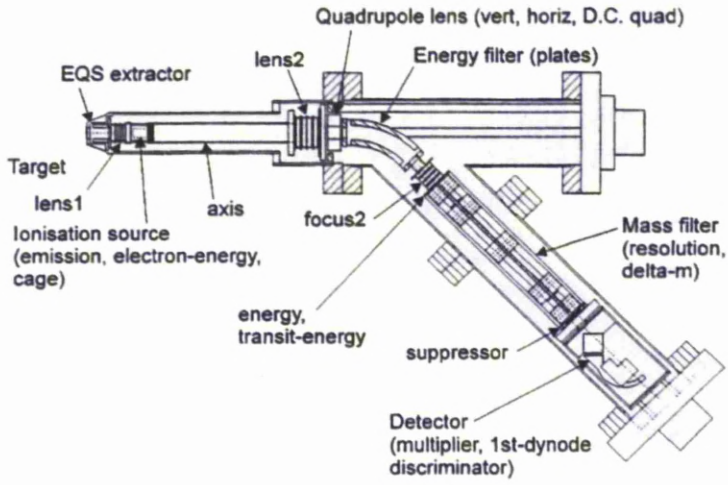

Figure 2.15: Hiden Analytical EQP300 mass spectrometer [52]

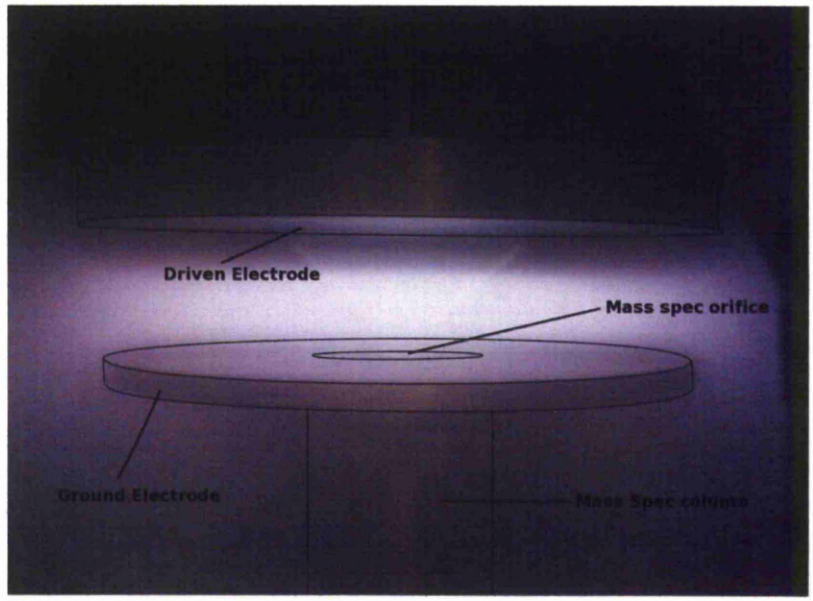

Figure 2.16: Image of EQP 300 in operation within the Plasma rig.

connected to the vacuum chamber as well as through the control unit, this allows the top of the mass spectrometer to act as the grounded plate. The EQP 300 consists of the main spectrometer (fig 2.15) and the power supply and control unit which is connect to a PC to control the operation of the instrument. Figure 2.17 shows the full mass spec setup.

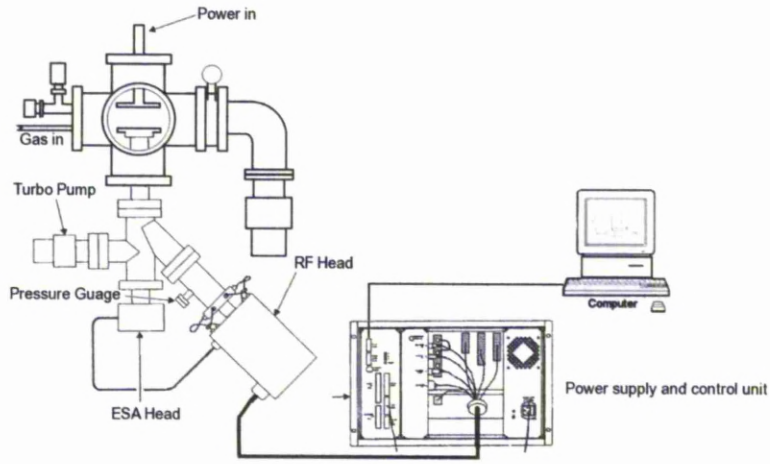

Figure 2.17: Mass spectrometer setup in the vacuum system.

2.4.1 Potential at nanotube surface

In order to accurately interpret the mass spectrometry results they must be modified to take into account for the fact that the nanotubes do not sit on a grounded surface. As the EQP 300 is grounded the results acquired are with reference to ground, however the CNTs sit on a silicon surface which is insulated from the grounded surface. The ions which arrive at this surface will have a different energy than those at collected by the EQP 300. It is possible to experimentally measure the potential which the CNTs sit. A probe was constructed to be electrically insulated from the grounded electrode and to sit 1 mm above it, this replicates the position were the CNTs are exposed to the plasma. Figure 2.18 shows a schematic of the probe set up and an image of the construction is shown in figure 2.19:

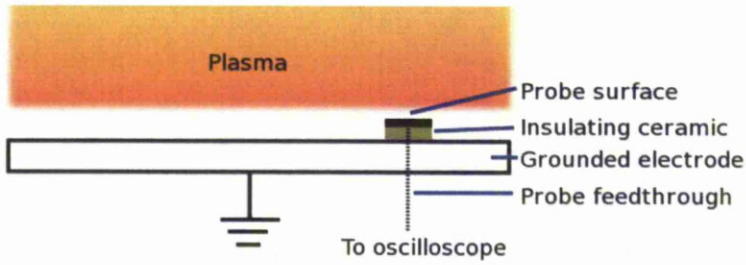

Figure 2.18: Schematic of ground probe.

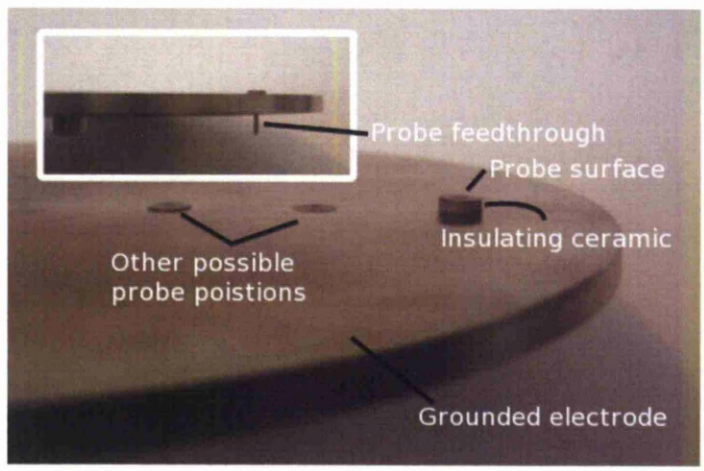

Figure 2.19: Mass spectrometer setup in the vacuum system.

2.5 Nanotube Production

Using the same methods as those described by I. Alexandrou [18] Multiwalled carbon nanotubes were grown in liquid nitrogen, de-ionised water and ethanol. The experimental apparatus used to produce the arc discharge in liquid is shown in figure 2.20. The system consists of an arc welding A/C power supply, an Clarke Weld 190 TE which acts as a constant current source. There are two carbon electrodes, supplied by POCO graphite, on a traveling x axis to maintain the distance between them, 1mm. They are an isotropic ultrafine grain graphite 25mm and 5mm in diameter, for the cathode and anode respectively, with an electrical resistivity of $24\mu\Omega/m$. It is the anode, shown on the right in fig 2.20(a), that is consumed during the arc plasma discharge, as explained in chapter 3.2. A diode between the source and the cathode half rectifies the supply and the anode is grounded to provide a stable reference. This has two main benefits, firstly it increases the lifetime of the anode, unlike the cathode heavy particles arriving at the grounded electrode do not have sufficient energy to damage the surface. Secondly the heat produced in the electrodes is reduced.

Voltage measurements were taken at points A, B and C. A 0.01Ω resistor between the anode and ground allows the current in the circuit to be calculated from the voltage drop. Measurements were recorded using a digital oscilloscope (Tektronic TCP202) using two x1 Probes (Tektronic P5100).

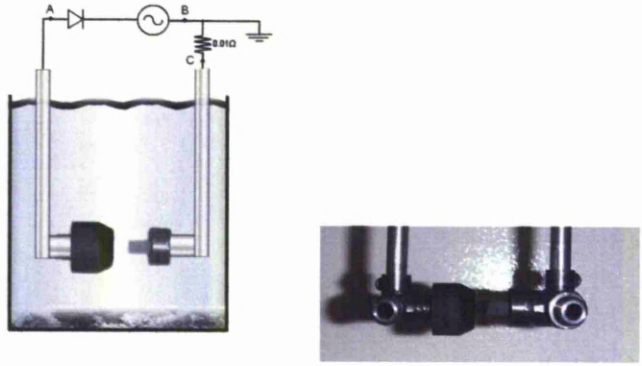

(a) (b)

Figure 2.20: Schematic of Arc discharge method used to produce carbon nanotubes.

Whilst the electrodes remain submerged in the liquid a constant current is passed

through the system. A carbon plasma arc discharge is formed when the two electrodes are brought within sufficient distance of each other, this can be seen in figure 2.21.

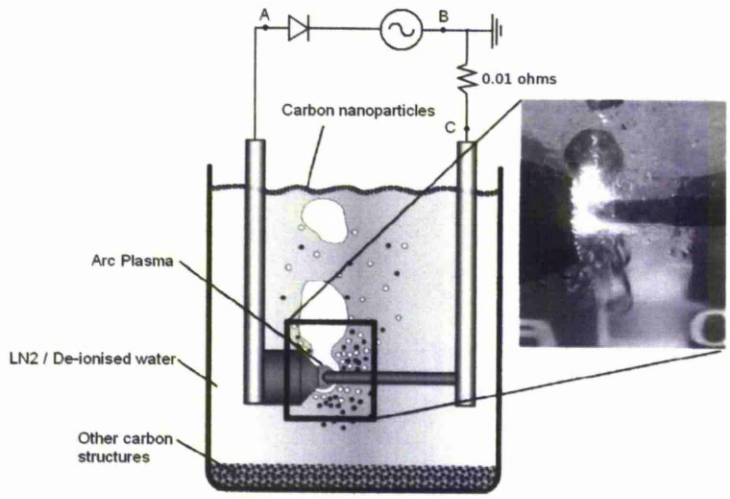

Figure 2.21: Schematic of Arc discharge method used to produce carbon nanotubes in water.

During the carbon arc discharge, the anode and liquid in the vicinity of the arc spot vaporize due to the intense heat. The gases formed escape in bubbles rather than in a continuous upward stream. When the formed bubbles reach the surface of the liquid, the vapor that has already condensed inside them is released onto the liquid surface in the form of small thin flakes [53]. These small flakes have been shown to contain carbon MWNTs and carbon onions [18, 53]. The process of removing the nanoparticles from the liquid differs depending on which liquid is used. After finishing the arc the liquid nitrogen is left to evaporate and the material is then collected in bulk from the bottom of the beaker. This material takes the form of a powder with large bulk particles, which contains no nano-particles. The powder is separated out by placing it in di-ionised water and subjecting the solution to an ultra sonic bath, this is then filtered using 5 *um* filter paper. Again this is left to dry leaving only the powder containing nanoparticles. The nano-particles in the water arc, and ethanol/water mix, form flakes on the surface of the water these are collected off the top of the water surface and are then filtered in order to remove any large carbon macroparticles, again with the 5 *um* filter paper, and are left to dry, leaving a powder containing nanoparticles. The

experimental setup used to produce CNTs can be seen in figure 2.22.

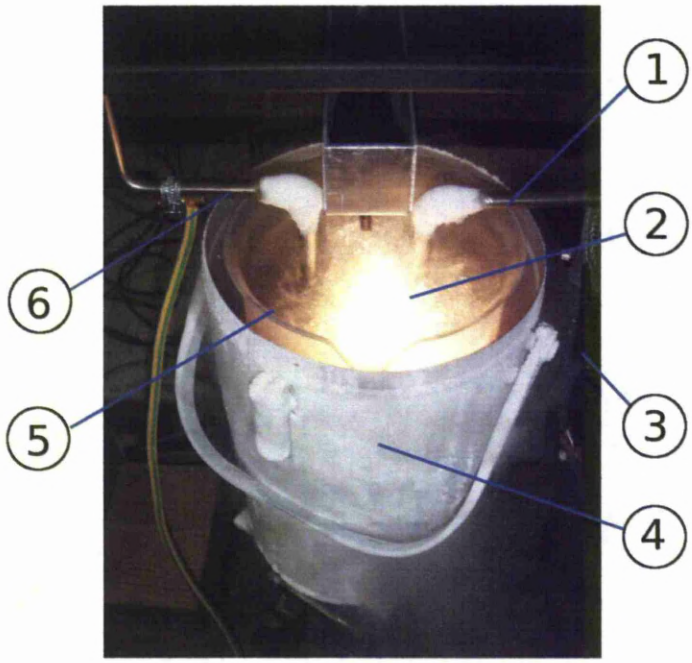

Figure 2.22: Photograph of the nanotube production system, not shown are the 0.01Ω resistor and the voltage probes.

1	Moving cathode arm
2	Arc in Liquid Nitrogen
3	High current diode
4	Protective aluminium beaker
5	Pyrex glass beaker containing Liquid Nitrogen
6	Fixed Anode arm

The nanoparticle powder can be seen in figure 2.23, this material was produced in a LN_2 and at this scale is representative of all the materials produced by different methods.

Figure 2.23: Nanoparticle powder produced in LN_2.

2.6 Optical Emission Spectroscopy

Optical emission spectroscopy (OES) is a technique used to analyse plasma properties by examining the light emitted from the discharge. It allows identification of the different species as well as the ability to calculate electron energies. There are however difficulties with using this technique on short arc discharges such as this. As the supply is 50Hz capturing one cycle proved difficult due to very low intensity levels, the small size of the plasma could of also contributed to this low intensity count. This meant that a number of cycles had to be accumulated in order to obtain intensities which allowed lines to be distinguished from the background. Unfortunately due to the nature of the discharge each cycle may not be the same as the previous even under the same experimental conditions, due to the constantly changing surface of the anode. Another important parameter that is influenced by the surface of the anode is the electrode distance. The distance needed to strike the arc is approximated to be between 0.1mm and 0.5mm (although the arc is run around 1mm), it is controlled manually however without precision it is not always possible to obtain exactly the same distance for each arc. The surface geometry and temperature of the electrodes can strongly influence the electrode distance needed to strike and maintain an arc.

1	Signal generator
2	Triggered signal generator
3	F-Number matcher
4	Optical fiber
5	Monochromator
6	ICCD
7	Optical control computer
8	Oscilloscope control computer
9	Oscilloscope
10	Cathode movement control
11	High current diode
12	Collimating tube enclosure
13	Voltage Probe

The OES system shown in figure 2.26 consists of a Thermo Oriel F number matcher, L.O.T. Oriel MS260i monochromator, shown in more detail in figure 2.26, and a Andor iStar DH520 intensified charged coupled device (ICCD) camera controlled via a PC

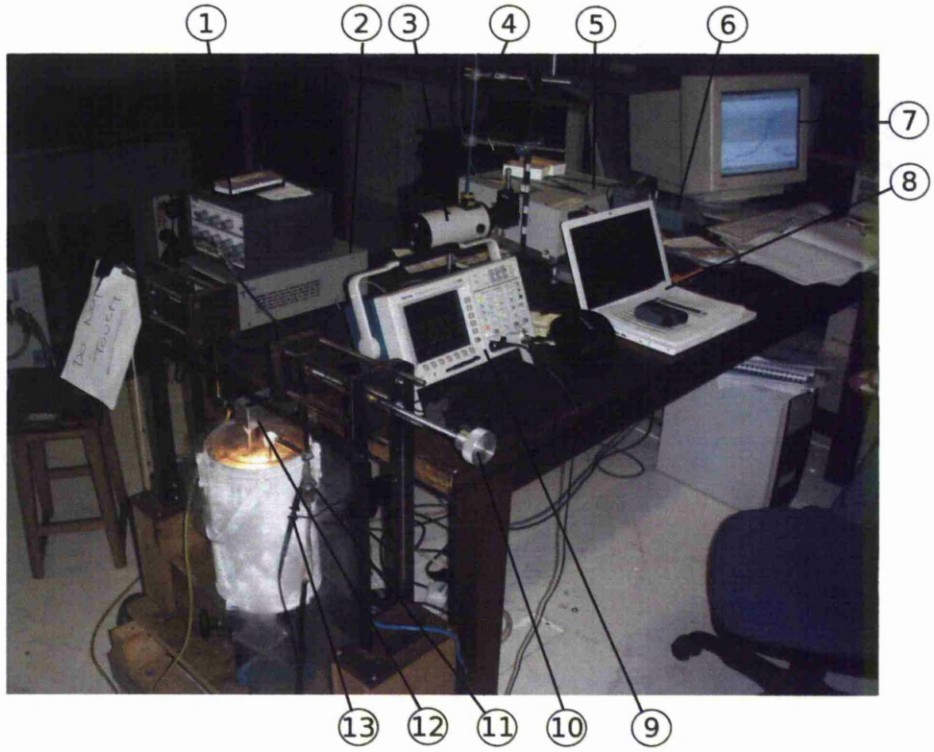

Figure 2.24: Photograph of the nanotube production OES setup.

running Andor MCD software v2.36. Light enters the system through a collimating tube, this tube is sealed in a custom built steel cylinder which has a Quartz window at one end. This allows the collimating tube to to be placed submersed in the liquid so that it is 15mm directly above the discharge. In order to obtain an accurate position the anode is fixed in place and a light is shone down the fiber, from the ICCD to the collecting point, in order to produce a bright spot out of the collecting end. This gives a visual point of were the light will be collected from, the collimating tube can then moved to the area on the anode where the plasma arc will strike. The light from the plasma travels down the tube and is then reflected through a 45°mirror onto a lens which focus the light down the optical fiber before reaching the F number matcher. The F number matcher is a series of angled mirrors which enables the F number of the fiber (f/2) to be matched with the F number of the monochromator (f/4). This is to improve efficiency of the system by minimising stay light due to the divergence

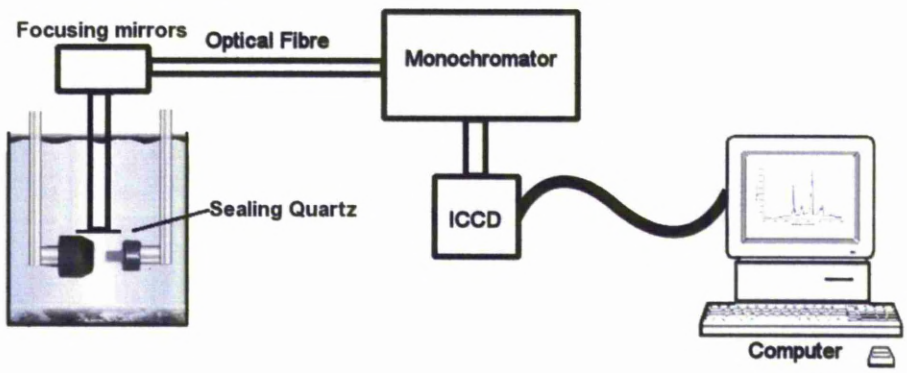

Figure 2.25: Schematic of the OES system.

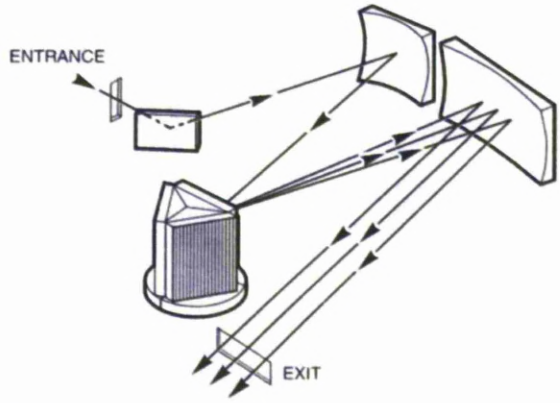

Figure 2.26: Optical configuration inside the monochromator [54].

of the light out of the fiber. Light enters the monochromater through a 50μm slit before reaching the diffraction grating, the slit width is a important component of the monochromators resolution. The width of the slit is inversely proportional to the width of the central maximum of the diffraction pattern and therefore a small slit with will give better resolution. However smaller slit widths will result in lower intensities meaning there is a trade off between good resolution and reasonable intensity levels. The diffraction grating separates the beam depending on the wavelength, the lines on the grating disperse the light creating intensity maxima at different angles, according to;

$$dsin\Theta_m = m\lambda \tag{2.5}$$

where d is the line separation, λ is the wavelength, Θ is the entrance angle and m is the order of the maxima. The diffracted light is then reflected on to the ICCD where the amount of charge in each pixel is recorded and downloaded to the computer. During the experiments carried out a 600 line grating was used to provide the maximum wavelength range possible with this equipment. The ICCD is a 1024 x 256 array with 26 μm^2 size pixels, the response factor of the ICCD is shown in figure 2.27. As the array behaves differently towards the edges data is only recorded in the pixel range of approximately 300 to 700. This ICCD response function was obtained by scanning over the pixel areas collecting data from a known constant light source and comparing the intensity at each pixel for a set wavelength. The camera is internally cooled to -12 °C to reduce electronic noise in the system.

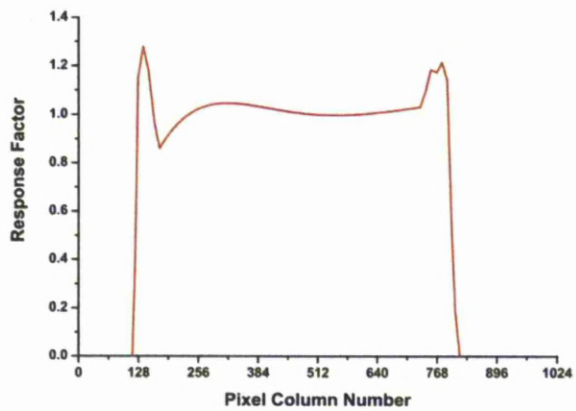

Figure 2.27: ICCD response function [55]

In order to ensure that the wavelengths measured are accurately aligned, calibration of the equipment was continuously carried out using argon and mercury pen lamps as well as a bright light source to line the fiber up with the arc discharge. This allowed for the data obtained to be shifted to correct for any system wavelength errors. Due to the nature of the system there is a inherent transfer function that must be taken into account before interpreting the spectra recorded. The system is wavelength dependent,

that is that as the wavelength increases the recorded intensity changes in accordance to the systems transfer function, this function can be seen in fig, 2.28. This wavelength dependent function was calculated using a tungsten emission lamp at a known temperature of 3400K (230V and 1KW, AC), the emission from this lamp behaves according to the Plank radiation law for grey bodies (the constant A, in eqn 2.6 accounts for the emission not being a perfect black body). This transfer function experiment was undertaken by I. Swindells [55].

$$I(\lambda) = A2\pi hc^2/\lambda^5(e^{hc/\lambda KT} - 1) \tag{2.6}$$

Knowing this allows the wavelength function to be ploted against intensity, Once normalised a five ordered polynomial is fitted to the curve shown in figure 2.28, this now makes it possible to obtain a function which when inverted can be applied to collected data to remove the wavelength dependent function, an example of which can be seen in figure 3.8 (chapter 3).

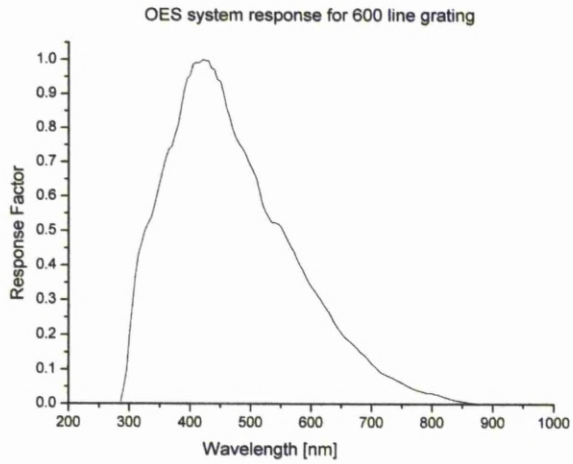

Figure 2.28: OES system wavelength response function [55]

The ICCD is controlled with two input signals, the shutter signal, which opens the shutter in preparation for imaging and the fire signal which tells the camera to image. For the time averaged results the shutter and fire signals where both set with a 12 ms pulse width and were set to fire at the same time. The camera fire signal was triggered by the voltage drop across the 0.01Ω resistor using two pulse generators and a RC filter

to obtain an accurate trigger position, shown in figure 2.29 both voltage and current of the arc can be seen with a generated signal in between. Without the RC filter in place the an accurate location for the triggering position could not be located, it was therefore decided that the simple filter would be used to remove any spurious peaks from the waveforms.

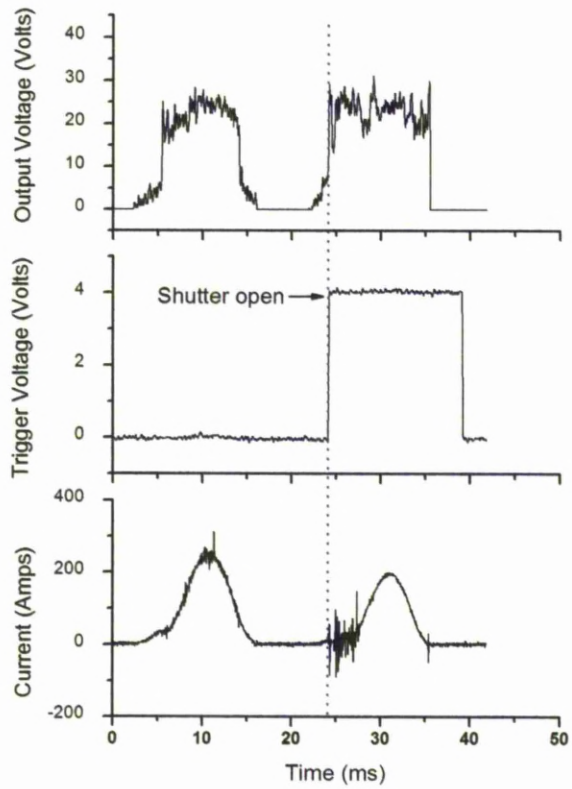

Figure 2.29: Trigger position example for time averaged OES. The shutter and fire signals are triggered at the same time.

However for the time resolved work the shutter was open for 1 s with the fire signal set with a 2.5 ms width, figure 2.30, the one 1s shutter signal is manually set. In the example shown the trigger position for the camera is set on the distortion of the current, this then triggers the camera fire signal. It was important to obtain an accurate record signal, and as shut the shutter was left open using a third trigger which was high for 1s, this allowed summing of all time resolved sections over the 1 second period.

The method of averaging over 1 second was selected due to the volitile nature of the process. By leaving the shutter open for the entire 1 second reduced the respose time of the system as opening and closing the shutter could take up to 1 ms and as such would reduce the time resolved capabilities. This meant that the system could image the arc without having to wait for the shutter to open.

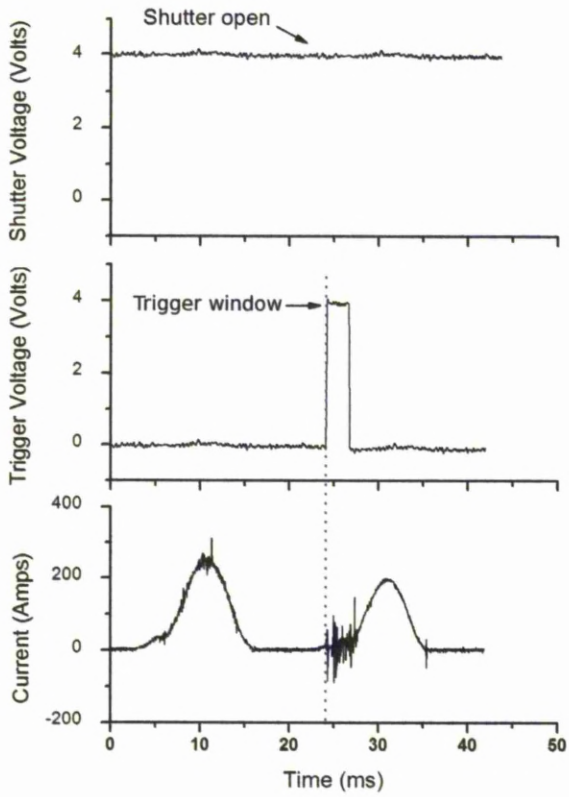

Figure 2.30: Time resolved example of trigger position, the image window is set by the trigger signal and does not have to wait for the shutter to open as the shutter signal is high set high.

2.7 Other Nanotube Analysis Techniques

2.7.1 X-ray Photoelectron Spectroscopy

XPS was performed on various nanotube samples by Dr Paul Unsworth of the Interdisciplinary Research Centre (IRC) at the University of Liverpool's surface science department on the VSW ESCA instrument. In order to accurately count the number of electrons at each kinetic energy the analysis must be performed in ultra-high vacuum (UHV), to achieve this the system is equipped with a rotary pump, turbo molecular pump, a molecular drag pump, a diaphragm pump and a titanium sublimation pump. The X-ray source is a monochromated source based on the Henke design [56]. Electrons are generated via thermonic emission from a tungsten source and are then accelerated on to a aluminium anode. The design of the system is such that the electrons are sharply focused over a area approximately $5mm^2$. The X-ray gun is isolated from the main chamber by an X-ray transparent Mylar window, this protects the samples from the high pressures and the monochromator from any materials desorption from the samples. The mounting of the X-ray gun allows it to be moved within a few millimetres from the sample. The sample is mounted on a x, y, z sample stage which allows for movement of the sample whilst under vacuum. The instrument has six focusing lenses for collecting photoelectrons and focusing them on to the entrance slit of the analyser. The energy scale of the spectrometer can be precisely calibrated to allow accurate measurement of the binding and auger energies. The analyser contains two channel plates situated beneath the slit, each plate runs individually and records data in parallel, the results are then summed together. It is this multi-plate arrangement that allows the analyser to produce high resolution measurements. The analyser is powered and controlled via a computer with custom software written by Scientific Instruments Consultants. The VSW ESCA instrument is the same as that used by Andreas Domkes in his Ph.D thesis [57] were a more detailed description can be found.

Nanotubes are drop cast onto small 5 mm x 5 mm glass plates coated with gold and are exposed to various plasma conditions before XPS.

2.7.2 Fourier Transform Infrared Spectroscopy

Fourier transform infrared spectroscopy (FTIR) was carried out by Dr Sam Haq of the Chemistry Department at the University of Liverpool on a Mattson Instruments Galaxy 6020 FTIR spectrometer. In FTIR infrared light is passed through a interferometer, which can measure all the IR frequencies at once, and then through the sample and is then recorded on the sensor, which measures the length of displacement in wavelength. When the infrared light light interacts with the sample some of the light will be absorbed and the chemical bonds will be affected by either symmetrical stretching, asymmetrical stretching, scissor bending or rocking bending. Light which passes through will then display a spectrum which is unique to the properties of the sample. In FTIR the adsorption of light will be in a specific wavelength range relating to the chemical functional groups rather than the structure of larger molecules. The signal that arrives at the detector is known as an interferogram, a fourier transform is applied to the interferogram in order to extract the spectrum.

Nanotubes were cast on the surface of an Infrared transparent plate made of potassium bromide (KBr). Background scans were performed to analyse any possible dispersion by the KBr, usually due to moisture collecting on the surface from the atmosphere. The data was collected at 4 cm^{-1} resolution over 200 scans. A wide band liquid nitrogen cooled Mercury Cadmium Telluride detector is used which has a spectral range of around 4000-600 cm^{-1}. For the background (reference spectrum which the sample sample spectrum was ratioed against) clean KBr plate was used, this is then removed from the final spectra.

2.7.3 Raman Spectroscopy

Raman spectroscopy was carried out at the Manchester Metropolitan University in the DRIAM Analytical services department by Dr Valdimir Vishnyakov. Raman spectroscopy is a chemical analysis technique that relies on inelastic scattering monochromatic light, also known as, Raman scattering. Raman scattering occurs when light interacts with a molecules electron cloud, this excites an electron to a virtual state, which will then drop into a vibration excited state. A laser beam is concentrated on the sample and irradiates the point of interest, the scattered radiation contains infor-

mation about the molecular vibrations/rotations and the energies involved. The shifts in energy can give information about the phonon modes in the system. The Raman assembly at Manchester Metropolitan University consists of two Renishaw setups, the first is the Micro Raman InVia and the second is the SEMSCA, this allows for accurate positioning and submicron resolution. The system can identify material phases and measure stresses. Carbon nanotubes were drop cast over the Sio_2 surface in the same manner which is used to produce nanotube transistors.

Chapter 3

Production of Carbon Nanotubes

3.1 Introduction

The most widely used methods of producing carbon nanotubes include techniques such as laser ablation [58,59], chemical vapor deposition (CVD) [60,61], high pressure carbon monoxide production [62] and arc discharge [18,53]. Laser ablation is a process which involves the pulsing of a laser at a graphite target in a high temperature reactor while an inert gas is bled into the chamber. The pulsing of the laser vaporises the target and CNTs are produced as a result and are collected off the cooler surfaces in the reactor. CVD requires the use of metal catalyst particles which are placed on a substrate, which is then heated to approximately 700°C , CNTs will grow at the sites of the metal catalyst and the diameter of the CNTs grown is relative to the size of these catalyst particles. In order to produce the CNTs two gases must be feed into the chamber; the first is a gas which contains the carbon for tube growth such as acetylene, ethylene, ethanol or methane the second is a process gas such as ammonia, nitrogen, or hydrogen. However all of these methods require large expensive equipment and produce can many unwanted materials within the carbon nanotube product. Arc in liquids however aims to reduce contamination, increase yield and significantly reduce costs. Growth of Carbon Nanotubes by arc in liquids is a relatively recent technique which, due to it's low running costs and simple setup, is starting to attract plenty of interest [17,18,53,63–65].

It has been shown by I.Alexandrou et al [18] and N.Sano et al [53] that MWNTs can be created using an arc discharge submerged in water. The liquid arc method is an attractive method of nanotube growth because the apparatus is simple to build,

there is no need for vacuum equipment, and the source materials are cheap, easy to find, and need no special care is needed, as non-explosive / corrosive materials or gases are used. The method requires only a dc power supply, a graphite electrode, and a container of liquid, as described in chapter 2. The process involves striking a carbon arc discharged between two electrodes figure, 2.21 submerged in various liquids including liquid nitrogen, ethanol and water. During the arc the anode and the liquid in its vicinity are vaporised and the gases formed escape in bubbles. The carbon plasma is confined in a gaseous bubble, which is eventually forced to the surface of the liquid. The formed particles are released onto the liquid surface while the uncondensed vapor is released to the air, producing carbon nanoparticles almost free of amorphous carbon [18].This chapter investigates the properties of arc discharges in various liquids. As discussed in chapter 2 optical emission spectroscopy (OES) and electrical analysis was carried out to study the plasma used to produce nanoparticles. Nanotubes were successfully grown in water, liquid nitrogen and a water ethanol mixture.

Due to the small size of plasma this chapter presents some non intrusive methods of diagnosis, such as material analysis, optical emission spectroscopy and electrical characterisation.

3.2 Arc in Liquids

An arc discharge is generally characterised by a high current density and a low voltage drop, it is this that differentiates it from a glow discharge. Arcs discharges also have a negative resistance, that is to say that the voltage drop will decrease as current increases. This type of arcing process is is an easy and convenient method for producing a thermal plasma, and due to it's high temperatures and ability to melt or vaporise metals they have been in commercial use for decades, in devices such as welding machines, arc lamps, chemical reactors and plasma spray coating systems.

The arc is initialised when the electrodes are brought into contact and due to surface roughness creates a small contact point which generates a high current density, this leads to vaporisation of the carbon and a breakdown of this vapour produces the arc discharge. The arc used can be characterised as an anodic arc, whereby the anode is consumed and the consumption of the cathode is negletable, this is due to the low

mobility and energies of the positive ions. As mentioned previously the arc discharge is a thermal plasma, whereby the electrons and the ions are at the same temperature (i.e. $T_e \approx T_i \approx T$), as shown later in this chapter the arc is also a non ideal plasma. Figure 3.1 shows the proposed arc discharge model for an electrical discharge submersed in liquid. The arc consists of a number of regions, the first being the arc itself, consisting of the arc column, and the sheath around each electrode. Due to the larger sheath at the anode will have much larger potential difference than that at the cathode. It is for this reason that the lower energy positive ions do not consume the cathode, due to the small size of the are the sheaths are expected to be in the order of 100nm. The compressed liquid region, figure 3.1, of the arc generated high pressures within the arc, as such the ions are neturalised very soon which leads to a low ionic current (preventing damage of the cathode). However a very small amount of erosion at the cathode does takes place at the start of each arc which subsequently drops off as the ions are neutralised [66]. The second region is a gaseous carbon/liquid mixture produced due to the vaporisation of the liquid. The third region is a compressed region of liquid which acts to restrict the first two regions. The plasma column has temperatures that reach 5000K, well above the sublimation temperature of carbon. Sano et al [53] state that the temperature gradient between the gaseous vapour and the liquid is a crucial component of the carbon nanoparticale formation, forcing the carbon to rapidly solidify. It has been proposed that the larger temperature gradient for the arc discharge in the LN2 than in water, can contribute to shaper bending of carbon to produce various different formations of carbon such as Nano Horns, and that the lower the temperature gradient give rise to slower bending which produces a higher proportion of nano onions [67]. The arc is generated by thermal evaporation of the anode, therefore unlike cathodic arc plasmas here the vapour is gereated by thermonic rather than thermofield emission [53]. The gaseous bubble expands due to the continuing vaporisation, once the bubble reaches a size whereby it is buoyant enough to float, a large part of it will float to the surface carrying various carbon nanoparticles with it, whilst the core of the arc is still surrounded.

The three liquids used vary drastically in their behaviour. The water evaporates at a relatively constant rate and provides the most stable arcing conditions of the three. The LN_2 and C_2H_6O provide two different problems. Due to the very low boiling point

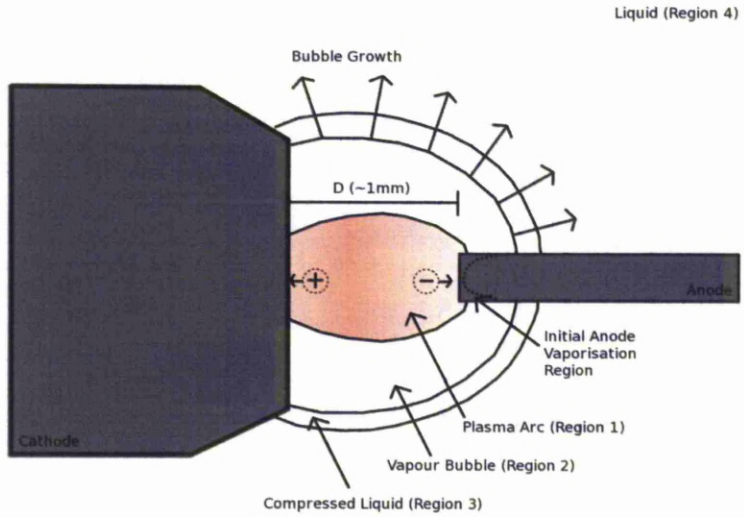

Figure 3.1: Arc Discharge model.

of LN_2, 77K, the liquid is always boiling at room temperature, this causes two issues, firstly the arcing process now takes place in a much more volatile environment and as such variation in the conditions which the plasma experiences fluctuate constantly, with different pressure, densities, etc. It is this variation in the system that leads to more defective nanoparticles than those seen in water [18]. Second and less significantly the evaporation of the liquid is much more rapid resulting in a near constant flow of LN_2 in the system in order to maintain the same levels of LN_2. However the lower temperature of the liquid provides good cooling for the electrodes and it has been shown that a higher ratio of CNTs to amorphous carbon can be attributed to the cooler electrodes [68]. The ethanol however represents a much more challenging problem. Although Ethanol has a boiling point of 352K, it is a flammable substance and as such has a flash point of 286K, and a auto ignition temperature of 640K. With temperatures in the arc high enough to start the evaporation process relatively rapidly great care must be taken not to run the arc for too long in order to ensure that liquid does not reach the required temperature so that the vapour given does not ignite. Therefore analysing arc in ethanol can be a long, laborious and dangerous process.

The arc discharge used in this work is similar to that used for electrical discharge machining (EDM). Research into EDM gained interest due to the ability to easily cut

materials difficult to shape using standard machining techniques and as such a number of models to explain the discharge process have been published. Eubank et al [66], from their model, calculated that a total of 18% of the total energy expenditure goes into vaporising the cathode, with 74% going into expanding the plasma by consuming the surrounding liquid.

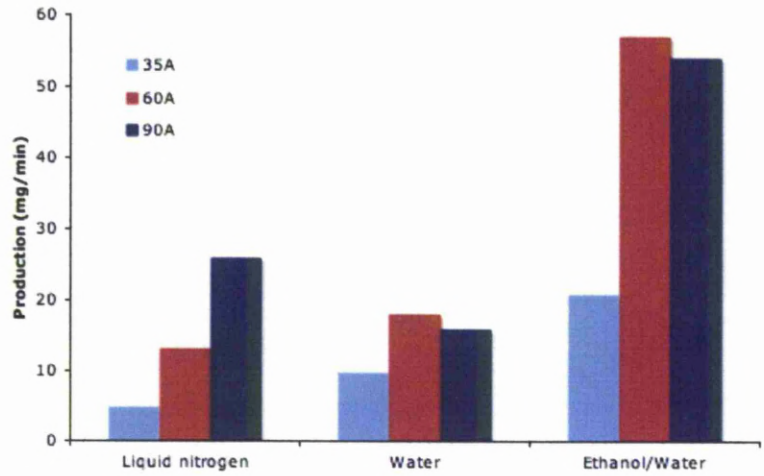

Figure 3.2: Production rates (mg/min) for LN_2, H_2O and C_2H_5OH at various currents.

Material production rates from the various arc conditions can be seen in figure 3.2, these values are measured from the final resulting powders. It can be clearly seen that the ethanol/water mixture produces is the most productive regime, this is due to the additional C feedstock (C_2H_5OH) and therefore producing the same amount of material would not require as much power than if running in water alone of liquid nitrogen. Both the ethanol/water mixture and the water experiments do not yield much higher production rates when increasing the current from 60A to 90A whereas the liquid nitrogen environment still shows a steady increase in production. The reason being that as the current increases within the ethanol/water mixture and the water experiments the temperature, and therefore the rate of bubble expansion, increases, this prevents the compressed liquid region from generated the same high pressures within the arc discharge. The liquid nitrogen is naturally cooler and this helps keep the electrode temperatures lower, allowing for increased production at higher currents.

3.3 Electrical Characteristics

In order to characterise the arc discharge process it is necessary to record the electrical properties of the system. Measurements for the open circuit output from the 35A arc-welding unit were taken at point B (on figure 2.21 from ET chapter 2) and can be seen in figure 3.3(a). This shows that the system in use is almost a perfect sinusoid (from a 50 Hz main supply) and provides a reference for all operation waveforms. However examining the FFT, figure 3.3(b) shows that there are a number of harmonics present. This must be remembered when considering the results.

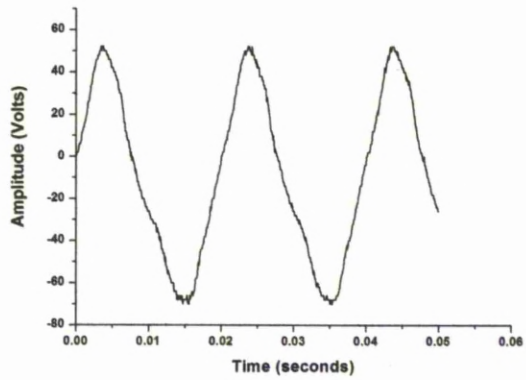

(a) Open circuit voltage waveform.

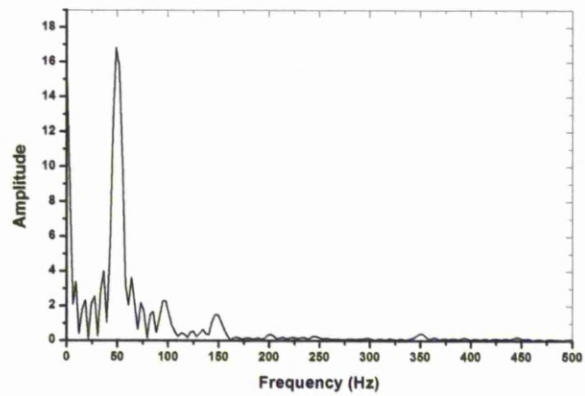

(b) FFT of Open circuit voltage.

Figure 3.3: Voltage waveforms of plasma arc discharge in liquid.

Figures 3.6, 3.5, 3.4 show current and voltage for 90A, 60A and 35A settings respectively, all currents are the root mean square values (RMS). Currents are calculated from the voltage drop across the 0.01Ω resistor, arc discharge voltage is measured directly with reference to ground. Figures 3.6, 3.5, 3.4 also show current waveforms for good quality (which are visually bright) arcs and poor quality (visually a dull red) arcs. The latter is caused when the equipment is not arcing correctly, mainly due to a large portion of the anode touching the cathode, therefore some of the current flows directly to the cathode resulting in heating of the electrodes which causes problems when taking optical spectrum, as well as lowering the yield.

The waveforms show a 5MHz signal at the start of the current waveforms and corresponding peaks on the voltage, when this 'noise' is visible the observed arcs are much brighter and produce a more defined OES signal. This suggests that the arc has two main regimes, that of the main 50Hz supply and the second from the much higher frequency 5Mhz. It is also noted that whist running a good bright arc the voltage is no longer sinusoidal, taking on a much flatter squarer form. In order to obtain a bright arc which runs for a long period these squarer noisier signals are required in order to sustain the discharge. It can be seen in figure 3.7 that the that the various different liquids result in different waveforms, this is to be expected as the resistivity of each liquid will be different, and as such it maybe possible to turn the liquid for optimum electrical performance.

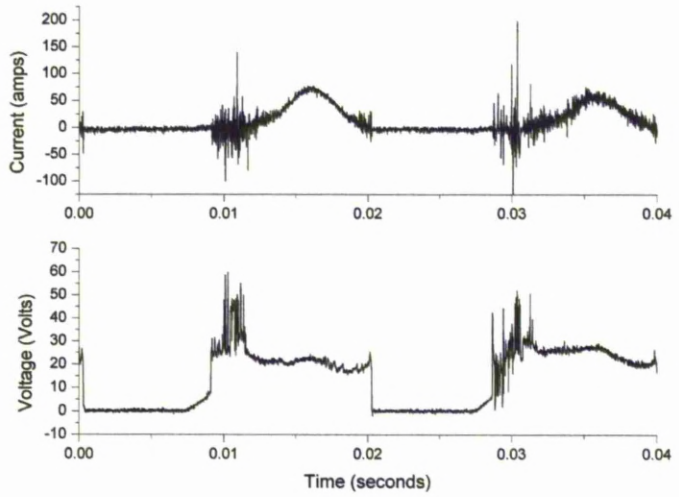

(a) Current (top) and voltage waveforms for a good water arc 35A

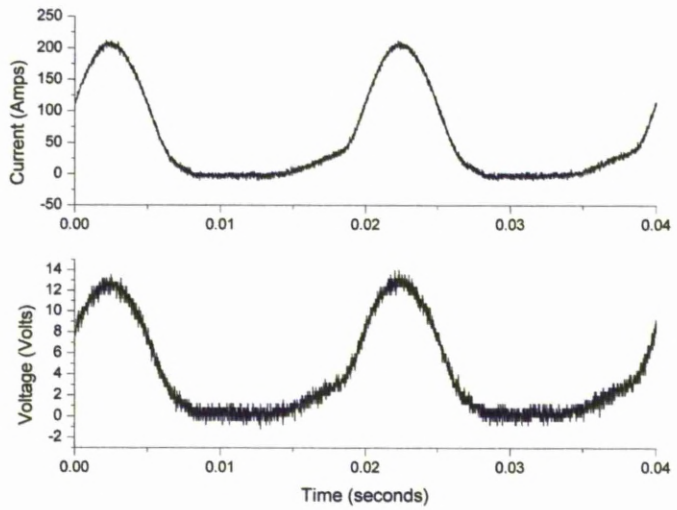

(b) Current (top) and voltage waveforms for a bad water arc 35A

Figure 3.4: Current and voltage waveforms in water for a 35A (a) good arc (b) bad arc

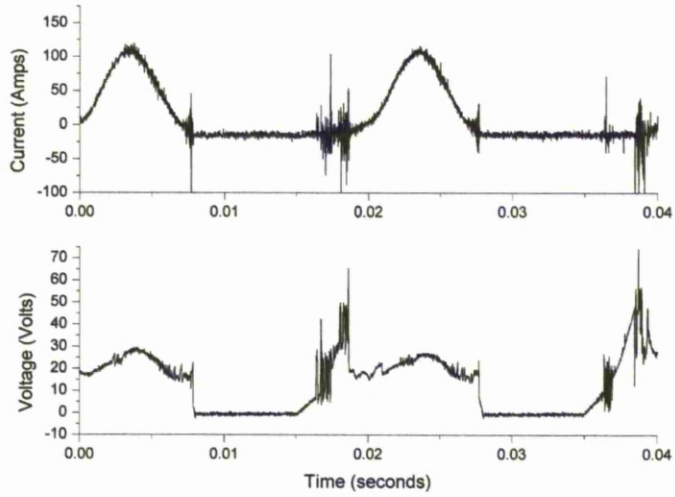

(a) Current (top) and voltage waveforms for a good water arc 60A

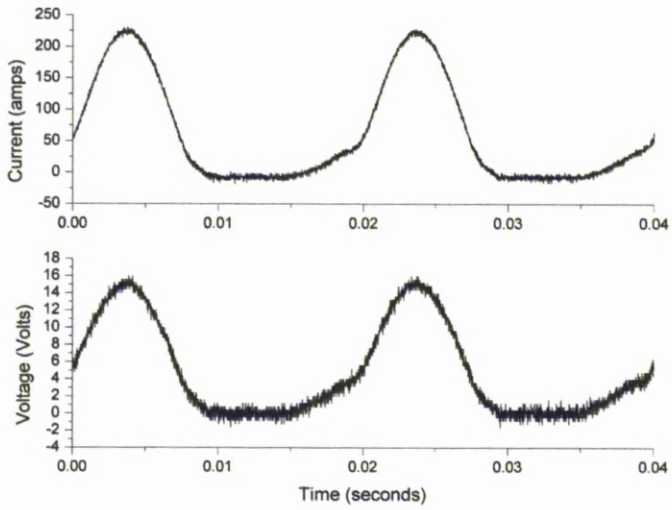

(b) Current (top) and voltage waveforms for a bad water arc 60A

Figure 3.5: Current and voltage waveforms in water for a 60A (a) good arc (b) bad arc

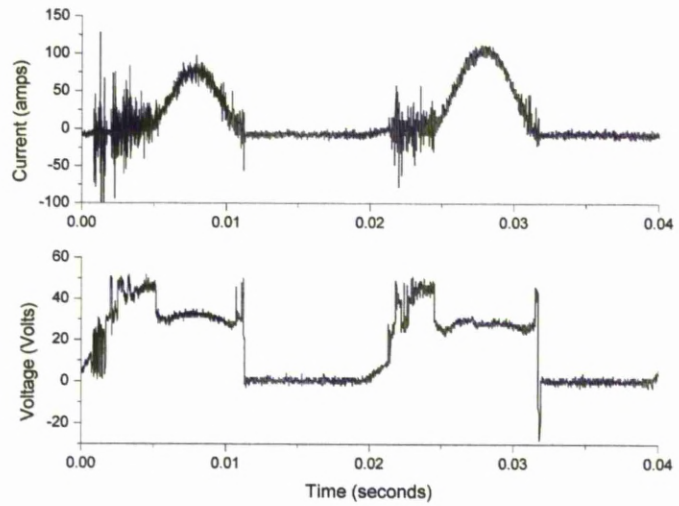

(a) Current (top) and voltage waveforms for a good water arc 90A

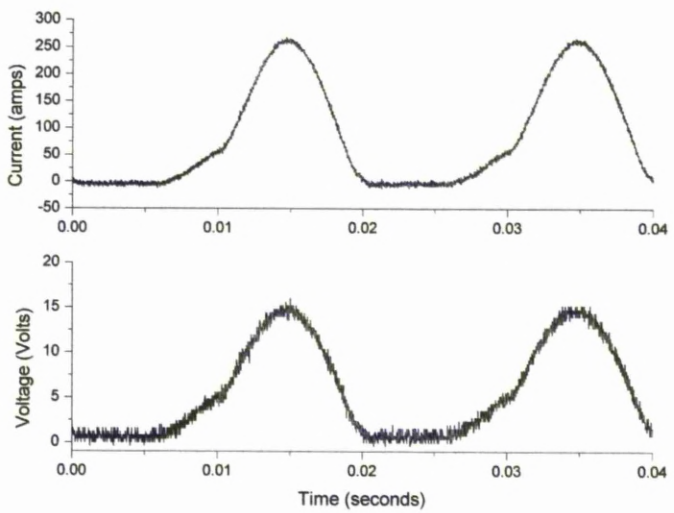

(b) Current (top) and voltage waveforms for a bad water arc 90A

Figure 3.6: Current and voltage waveforms in water for a 90A (a) good arc (b) bad arc

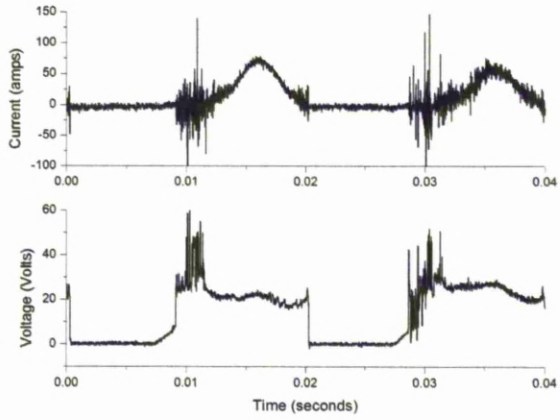

(a) Current (top) and voltage waveforms for a good water arc 35A

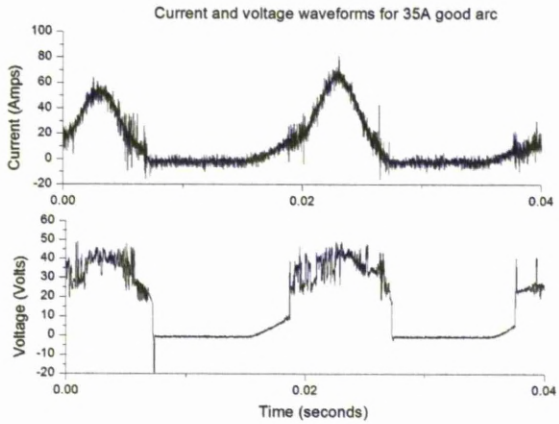

(b) Current (top) and voltage waveforms for a good liquid nitrogen arc 35A

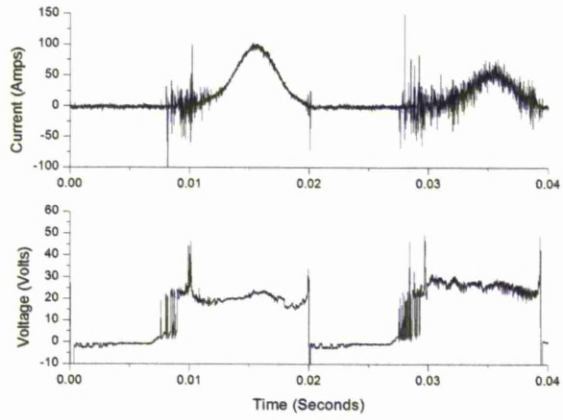

(c) Current (top) and voltage waveforms for a good water/ethanol mixture arc 35A

Figure 3.7: Comparative current and voltage waveforms for a 35A a) water arc b) LN2 arc c) Water Ethanol mixture.

3.4 Optical Emission Spectroscopy

OES of plasma arc in liquid is a very difficult task, due to the small gap distance 1mm, highly erratic discharge conditions, constantly changing volume and transparency of the liquid. Optical spectroscopy was carried out for the three different current conditions mentioned earlier (35 A, 60 A, 90 A) for both liquid nitrogen, water and the water ethanol mixture. Also collected was time resolved data for the H_2O arc. The spectra for each of the conditions is corrected for the response of the system and the background is then removed, as discussed . The normalised and background removed results for OES are shown, each spectra was a accumulation of 100 spectra to produce each graph, due to low intensity levels and is then normalised to the 516 nm C_2 line to aid comparison between conditions, this is due to the arc being erratic and will allow different cycles to be easily compared. Figures 3.8(a) and 3.8(b) show the spectra before and after the data has been processed, (whereby the machine transfer function has been removed as explained in Chapter 2.5).

Figures 3.9 shows raw data for the 320 nm to 480 nm spectral section. It can be seen that over time the background intensity increases until it engulfs any lines that were previously visible. Descoeudres et al. [69] atribute this to extreme densities which destroy the upper energy levels of the atoms meaning that the free bound radiation becomes more important than the line radiation. This is where an electron collides with an ion and recombines, the excess energy appears as a photon. This suggests that the plasma is non ideal having a very high electron density. Where by the average number of electrons contained within a debye sphere, (i.e. a sphere with diameter of one debye length) is much greater than one. All data is recorded with both the 600 grating and and the 1200 grating to allow resolutions shown in figure 3.10 enabling accurate line assignment.

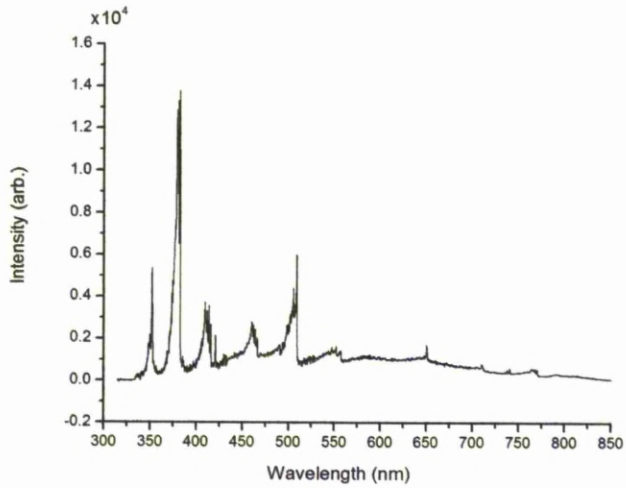

(a) OES spectra for a plasma arc in liquid at 90A half rectified AC before data processing.

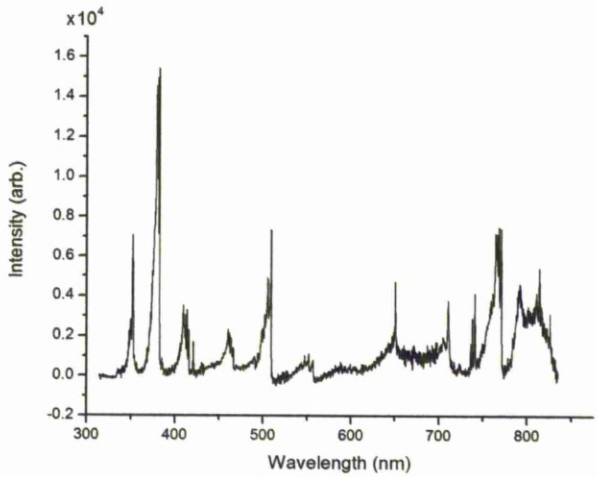

(b) OES spectra for plasma arc in liquid at 90A half rectified AC after data processing.

Figure 3.8: It is important to account for the system response as shown here, LN_2 spectra before (a) and after (b) data processing.

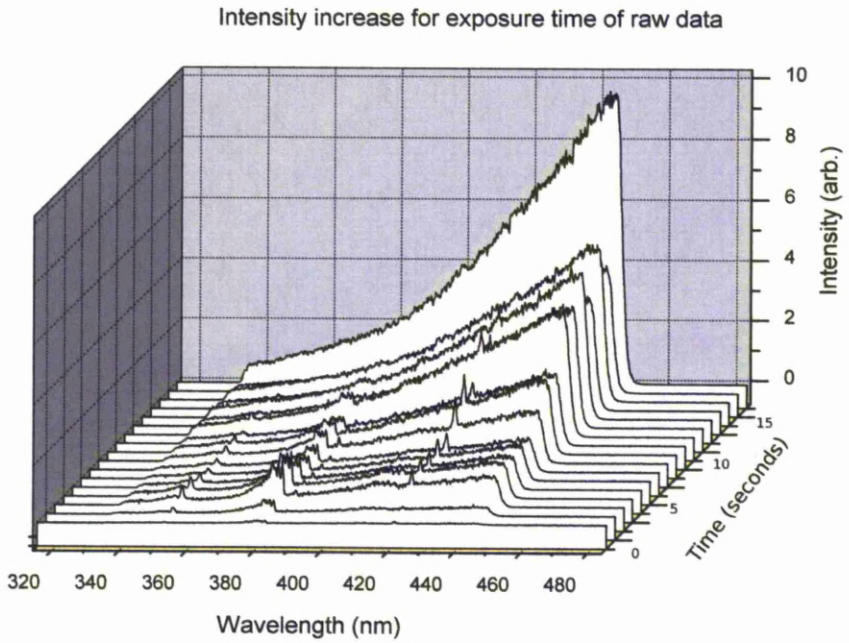

Figure 3.9: An increase in background radiation can be seen as the length of time the arc runs increases.

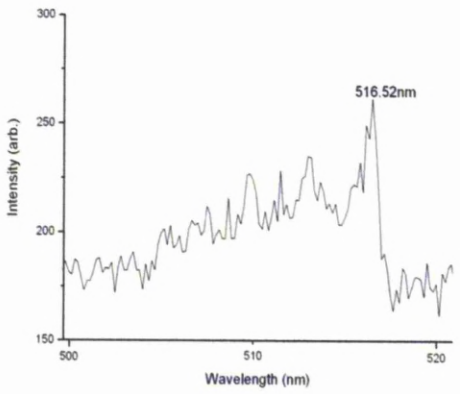

Figure 3.10: Example of the high resolution 2400 grating, giving detail to sub nanometer accuracy.

Plasma in LN_2 Spectra

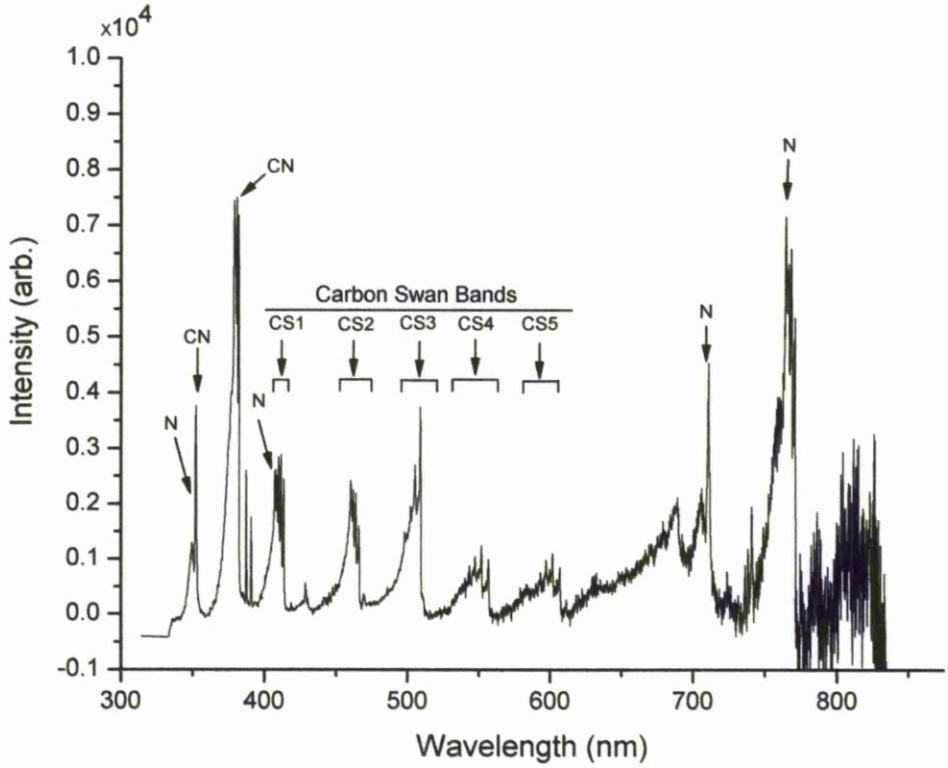

Figure 3.11: The most important line assignment for a 90A half rectified LN_2 arc, which are relevant to this study, the carbon swan bands, CN and molecular nitrogen.

From left to right the spectrum shows the peak for $N_2{}^+$ at 359, then most importantly for nitrogen incorporation in the nanotube lattice is the CN bands. CN peaks are readily observed by OES due to their low excitation energy of 3.2eV. CN can be seen in the UVA region at 359.0 nm and 388.3 nm the latter of which is the most intense line visible in the spectra being attributed to the 0-0 band [70]. This CN transition process is in the violet system and takes the form $B^2\Sigma + -X^a\Sigma +$ [71]. CN is formed by the reaction of the activated nitrogen species in the plasma with the carbon species from the carbon electrodes. Other CN lines were also detected at 358.4nm 385.5nm, 386.2nm and 388.4nm which correspond to the bands 3-2, 3-3, 2-2, and 1-1 respectively [70].

The main features present in the all the OES spectra recorded are the carbon swan bands, C_2. This is the most easily excitable of seven known C_2 systems, and is given the notation of $d^3\Pi_g - a^3\Pi_u$, the potentials for this system can be seen in figure 3.12. The carbon swan band system was initially discovered in 1856 during the study of flames with carbon components and is a predominate feature in many different sources from comets (Richter 1965), to flame spectra (Gaydon 1957).

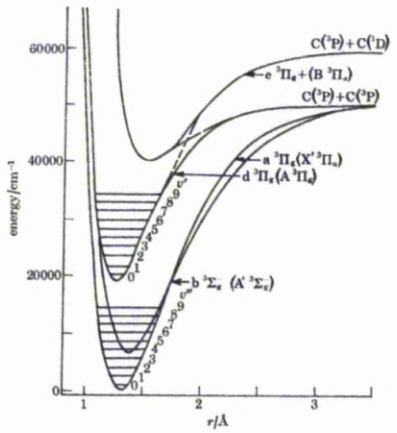

Figure 3.12: Potential Curves for the swan band system ($d^3\Pi_g - a^3\Pi_u$) [72].

This potential data (fig 3.12) is important for analysis of the system, along with transitional probabilities and Einstein co-efficients, many of which have been calculated in numerous publications [73–77]. It can be seen in figure 3.12 that there is a overlap of various systems, within the swan bands. This can produce problems when identifying line or anayalsing data for higher energies when the band exhibit greater rotational extension [72]. The swan band system lies in the wavelength range of 400nm to 600nmm, with the four main band heads at 438.2nm $\Delta v = 2$(labelled CS1), 473.7nm $\Delta v = 1$ (CS2), 516.5nm $\Delta v = 0$ (CS3) and 563.5nm $\Delta v = -1$(CS4), with a smaller fifth band at 600nm $\Delta v = -2$ (CS5) [72, 78].Also visible is the DeslandresD'Azambuja system $C^1\Pi_g - A^1\Pi_u$. these C_2 emisisons require large excitation energies they sit at 358.76nm, 385.22nm and 411.259nm [71].

N_2 molecular peaks can be seen at both ends of the spectrum along with $N_2{}^+$. Table 3.1 shows the main lines. A full list of line assignments can be found in appendix A.

Arc-in liquid nitrogen for variation in current is shown in figure 3.14. The three CN bands; (5, 5) at 384.9nm, (3, 4) at 416.8nm and (0, 2) at 460.6nm and the Carbon swan

Table 3.1: Table showing important wavelengths and band assignments for OES of plasma arc in LN_2

Wavelength (nm)	Structure	Band	Ref
358.421	CN	3,2	[70, 78]
385.517	CN	3,3	[70]
386.186	CN	2,2	[70]
387.189	CN	1,1	[70]
388.36	CN	0,0	[70]
416.926	N		NIST
438.2	Carbon swan band 1 (C_2)		
473.7	Carbon swan band 2 (C_2)		
516.5	Carbon swan band 3 (C_2)		
563.5	Carbon swan band 4 (C_2)		
605.9	Carbon swan band 5 (C_2)		
419.92	N		NIST
437.09	N		NIST
600			
650	H		
717	N_2		
775	N_2		

band system, $d^3\Pi_g - a^3\Pi_u$, is observed. However the whole swan system is not present in the 35A spectra, possibly due to lower intensities. Other lines identified correspond to CH, $C2\Sigma^+ - X^2\Pi$ band of (0, 0) [38], H2, N2 and atomic O [79, 80].

Variation in current leads to changes in the intensities of the spectral lines with reference to line 516.5nm, however it did not lead to new lines appearing. 35 Amps and 60 Amps settings showed approximately the same intensities for the carbon swan bands CS2, CS3, CS4 and CS5 as well as CN 359nm. The 35 amp setting did show higher CN levels at 388.3 but the first carbon swan band, CS1, was very small in comparison to both 60A and 90A settings. The carbon swan bands for 90A where again approximately the same intensities for 60A and 35A however the CN lines showed massive increases. At 359nm intensity was up 56% on 35 and 60 amps while at 388.3nm intensity showed a 144% increase over 35A and a 340% increase over 60A. An increase in the optical emission around the the wavelength of the CN peaks implies higher CN production and possibly higher production of nanotubes incorporate nitrogen. Unfortunately due to the low intensity of the spectra once the data has been corrected for the response

Molecular species	System	Electronic transition	Vibrational transition	Wavelength (nm)
C_2	Deslandres–D'Azumbuja	$C\,^1\Pi_g$–$A\,^1\Pi_u$	(0, 0)	385.22
			(1, 0)	360.73
			(2, 1)	359.29
			(3, 2)	358.76
C_2	Swan	$d\,^3\Pi_g$–$a\,^3\Pi_u$	(0, 0)	516.52
			(1, 1)	512.93
			(2, 2)	509.77
CN	Violet	$B\,^2\Sigma^+$–$X\,^2\Sigma^+$	(0, 0)	388.34
			(1, 1)	387.14
			(2, 2)	386.19
			(3, 3)	385.47
			(4, 4)	385.09
			(3, 2)	358.39
			(2, 1)	358.59
			(1, 0)	359.04

Figure 3.13: Line assignments taken from Acquaviva [71]

function the spectra becomes very noisy from 650 nm onwards making it very difficult to identify specific lines. Towards the end of the spectrum, atomic oxygen, hydrogen and further nitrogen lines are present, however they are difficult to identify due to the noise levels from 650 nm onwards.

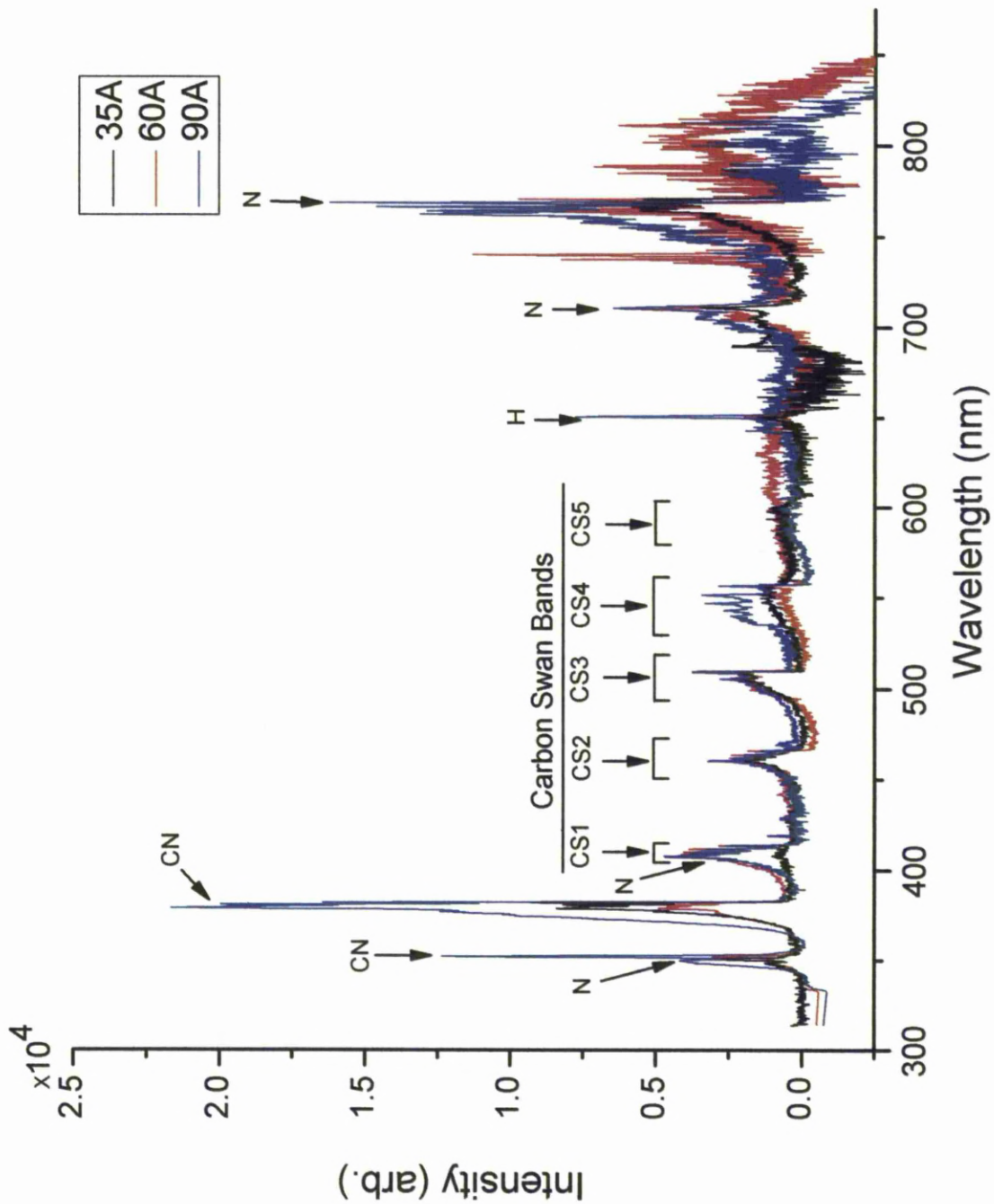

Figure 3.14: Variation in OES spectra for change in current, black) 35A, Red) 60A, Blue 90A

Plasma in H_2O Spectra

Figure 3.15 shows OES of arc plasmas in water for arc currents of 35A 60A and 90A, it can be seen that 60A produces the most intense peaks of the Carbon Swan System, CS1 to 4, this would suggest that more C_2 particles are produced. This spectra displays more noise than that of the other two liquids due to the water absorbing the light more and therefore less light is recorded by the ICCD. This shows that simply upping the current does not produce more carbon, which might affect the production of carbon nanoparticles. This agrees with measured material properties. This maybe due to the 90A plasma expanding more violently than at lower currents. This would result in the vapour bubbles expanding at a faster rate causing lower vapour pressure, and therefore fewer C_2 molecule production and leaving less time for nanoparticle production. Analysing the area under the Carbon Swan peaks shows that there is a 25% increase in production of C_2 molecules at 60A than at 90A whilst 35A has the lowest production. As the area under the curves may represent Carbon production because more excitations will lead to higher peaks and therefore larger areas. This is made more accurate by removing background and the camera response before analysis.

Figure 3.16 shows time resolved data for a 90A water arc (fig, 3.6) which was taken using the timing process describe earlier (fig 2.30), this allowed a delay to be established between the start of the discharge and the period in the cycle to be recorded. This delay could then be varied to record data at 2.5ms intervals. Due to the erratic nature of the plasma data was accumulated over 50 cycles for each time period, in order to average out the data.

H_2 is most intense between 5ms and 7.5ms, showing the breakdown of the OH bonds at the point were the current is highest. The intensity of the carbon peaks reach their highest between 7.5ms and 10ms. It can clearly be seen from the data that the highest production of both C and C_2 with the lowest production being from the peak of the waveform onwards. This suggests that nanoparticles are predominately produced towards the end of the arc discharge.

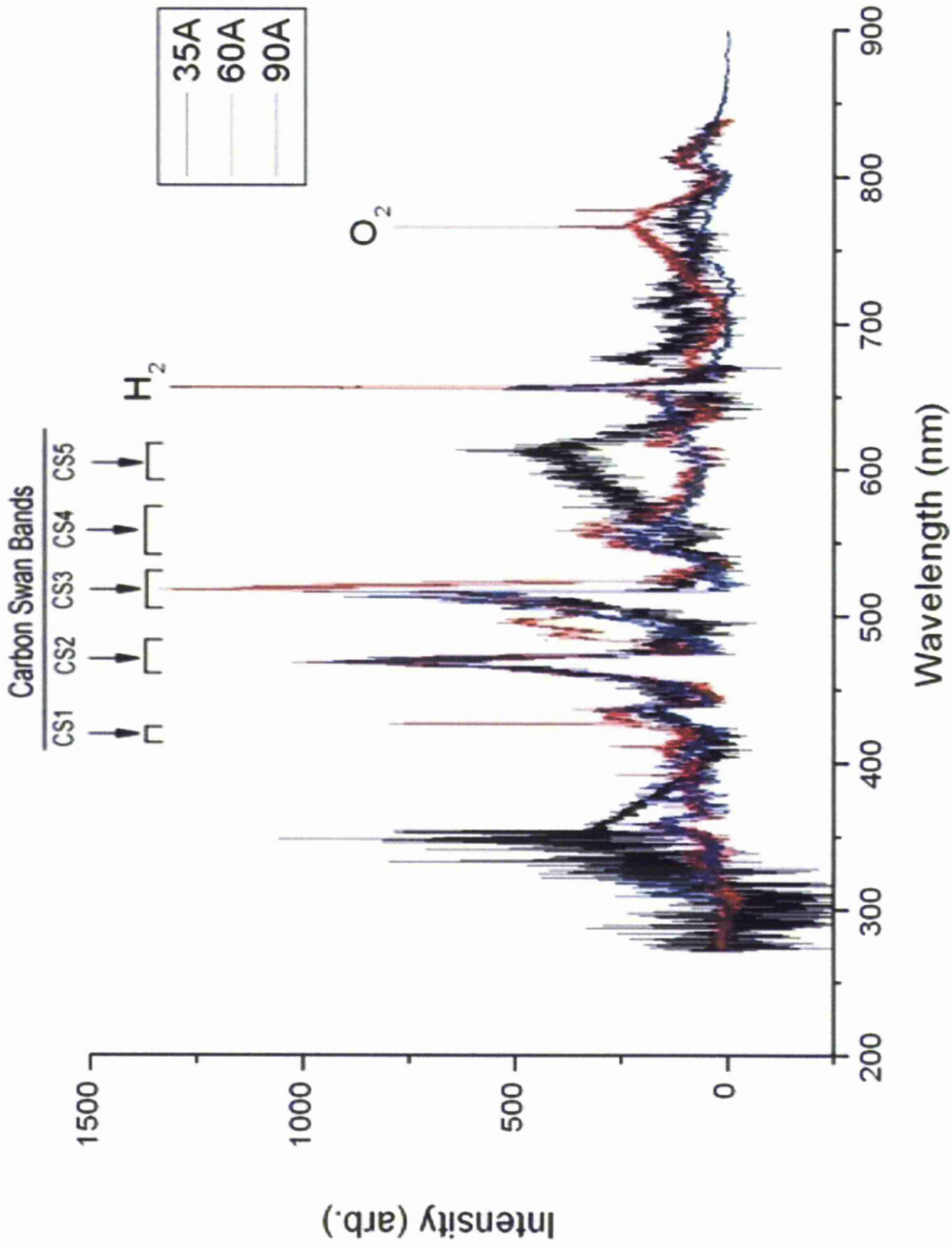

Figure 3.15: H_2O current variation

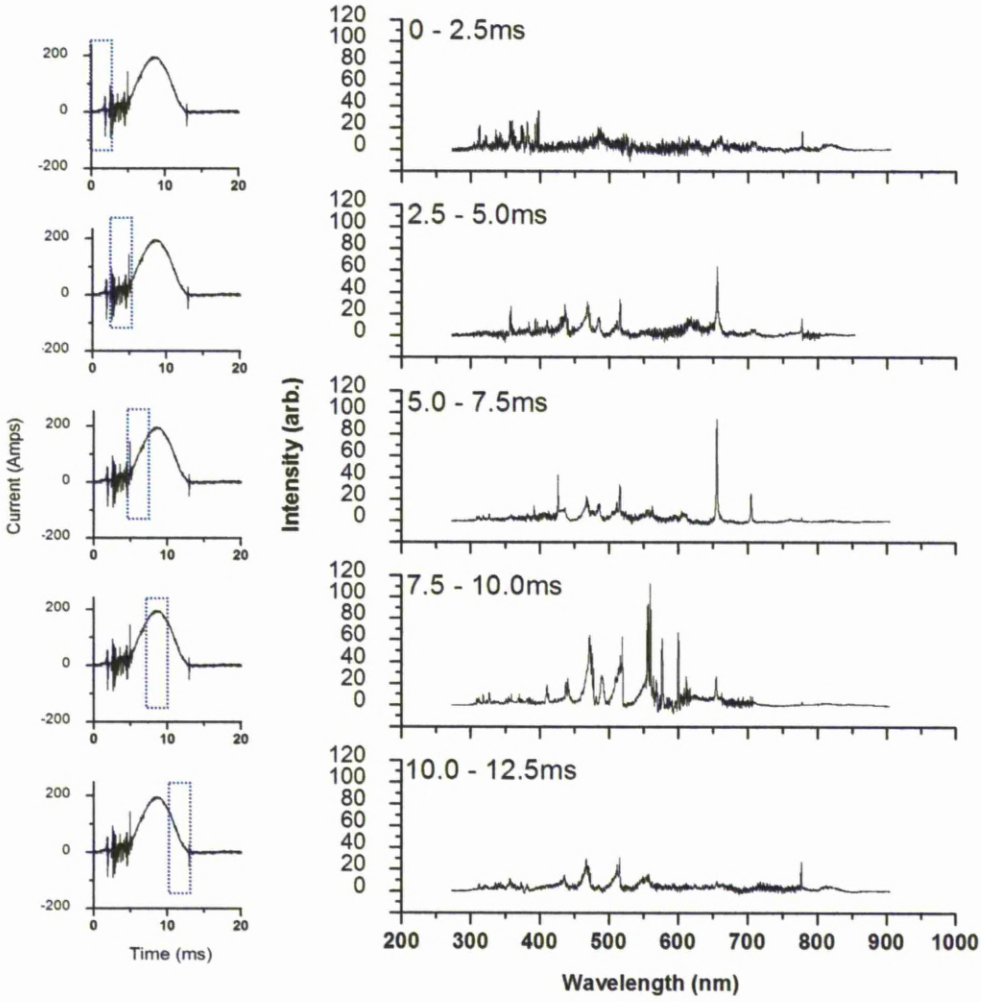

Figure 3.16: Time resolved data for the liquid arc running at 90A 50Hz as seen in figure 3.6. Data taken at 2.5 ms intervals and averaged over 50 cycles. Data collected using the examples technique explained in figure 2.30.

Plasma in C_2H_5OH Spectra

As expected, from the LN_2 and H_2O results, both the DeslandresDAzambuja system and Carbon Swan System are present. O2 is also present at 777.194nm [80]. As you can see from figure 3.17 OH (0, 0) bands groups can be seen between 307.53nm and 312.961nm and again at 316.961nm [81].

The ethanol work was limited due to the extremely volatile nature of the liquid mixture. Although nanotubes have been created in a ethanol/water mixture at 90A due to the lengthy nature of OES experiments it was not safe to run the arc for long enough periods of time to record spectra.

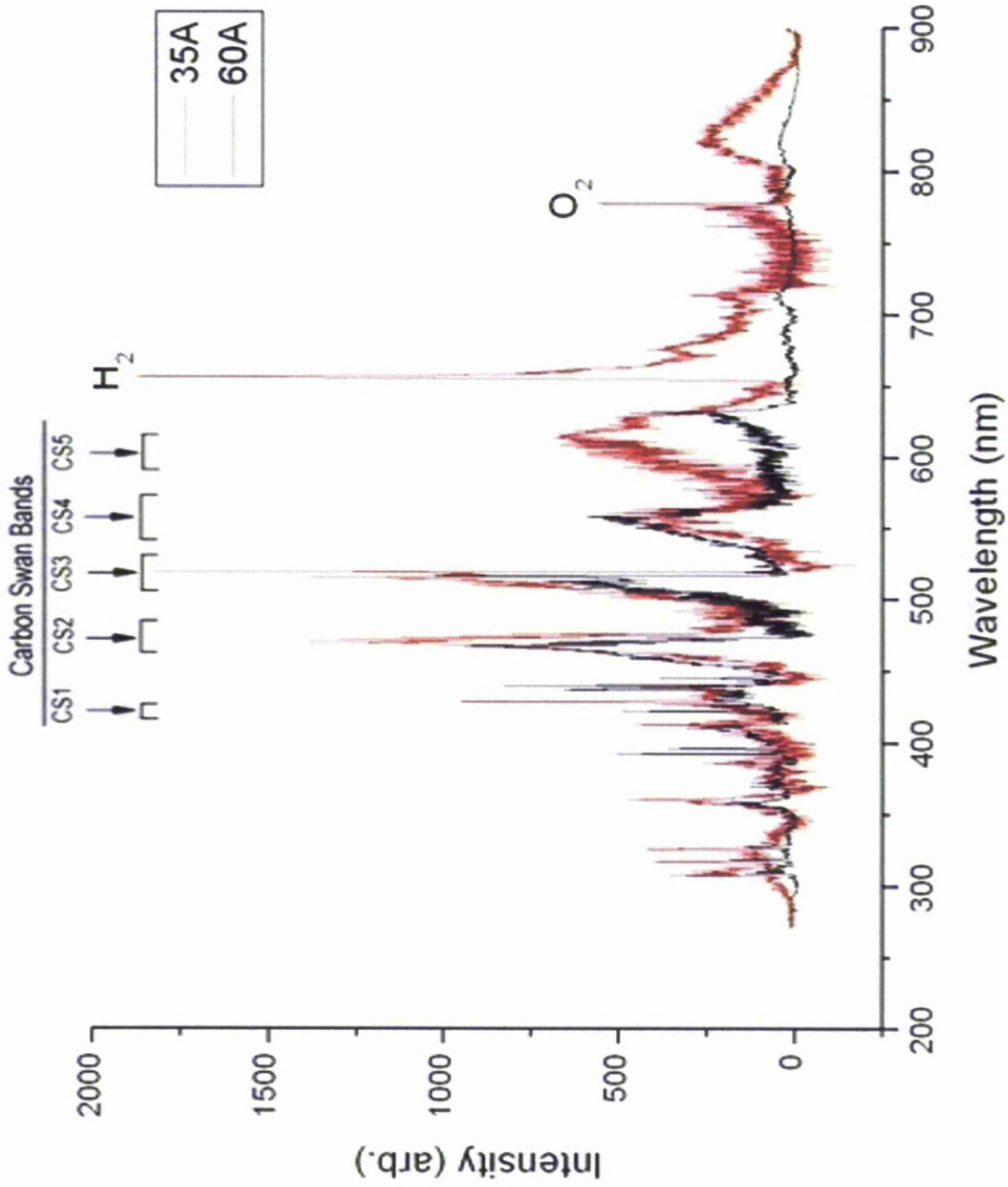

Figure 3.17: OES of plasma in ethanol and water mixture

As can be seen in figure 3.18 when comparing all the various liquids that the liquid nitrogen is the only one to contain CN bands, which is what would be expected. When normalised to 516nm ethanol has the strongest swan band system, i.e. all five bands are present compares to the three and four in liquid nitrogen and water respectively. This ties in nicely with the production results seen earlier, were the ethanol/water mixture produced more material, due to the additional feed stock within the ethanol.

It must be remembered that due to the difficulty of recording the OES in boiling liquids direct comparisons may not be completely accurate. Normalising the data, to a peak, does allow comparisons of what bands are present but does not give an description of intensity variation i.e. the 516nm line for liquid nitrogen maybe half that of the ethanol/water solution.

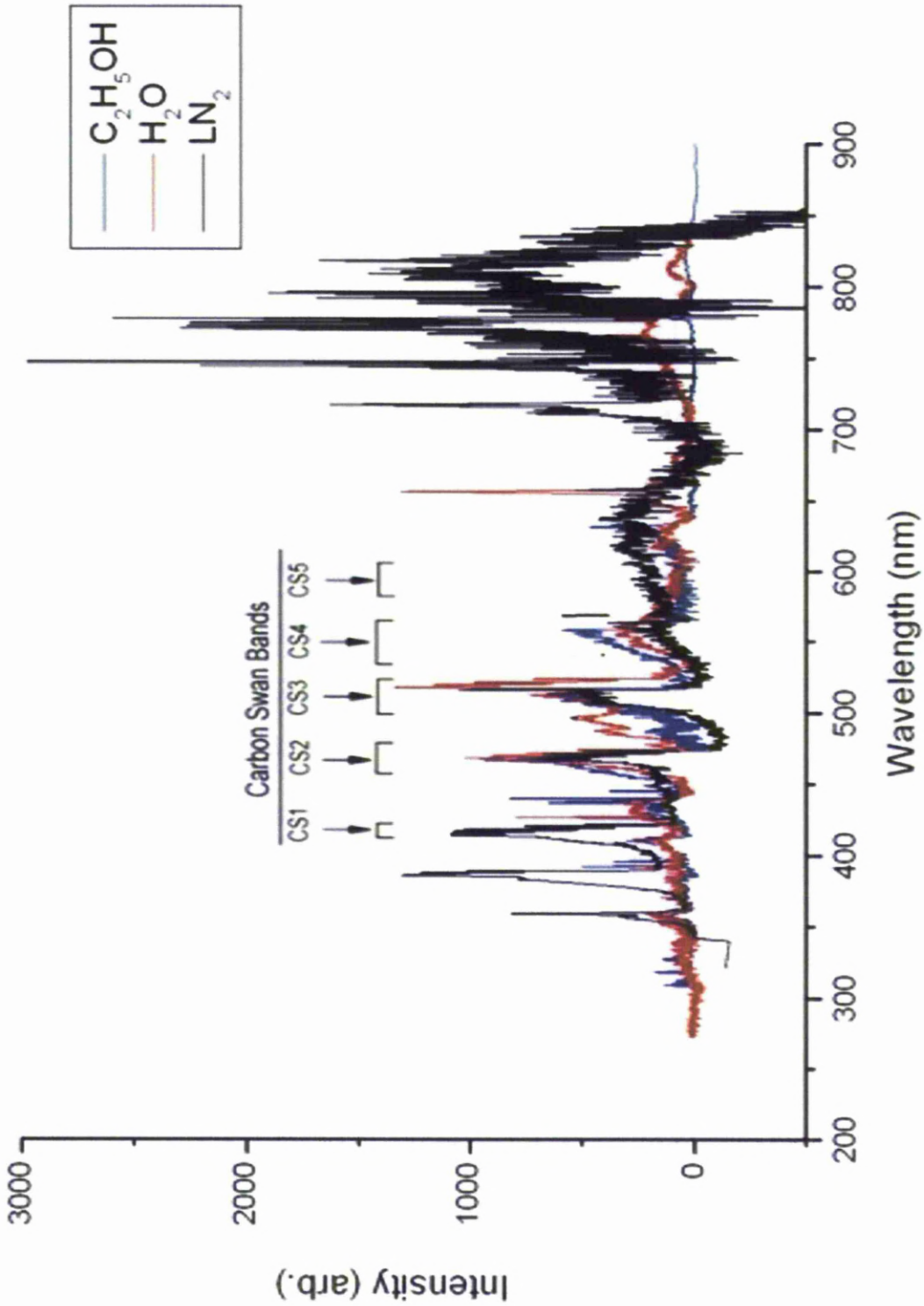

Figure 3.18: Comparison of all data, normalised to 516nm

3.4.1 Summary

This chapter lays down a basis for fine tuning the carbon arc in liquid process to produce higher yield systems. Electrical measurements have been taken and compared to OES spectra and quantities of material produced to give a good base for fine tuning the arc. A theory for the growth are carbon nanotubes within a liquid arc has been suggested and linked to time resolved data which helps explain the growth of the arc bubble and nanoparticle production. Important optical emission lines are identified and explained. Linking CN lines with increased nitrogen incorporation into the carbon lattice allows for the theory that doping of the nano particles can take place during production in the liquid arc depending upon liquids used.

From the OES carried out it can be seen that the arc is a non ideal plasma due to the high electron energy observed in figure 3.9 and low electron temperature estimated. A greater proportion of CN is produced at 60A, but C_2 production remains constant throughout, implying a higher production of nitrogen incorporated nanoparticles. Nanoparticle material (both C_2 and CN) is produced at a higher rate during the start of the arc waveform with production dropping with time. It has also been shown that a more efficient method of producing material is the use of ethanol/water mixture giving additional carbon feed stock to the arc. Time resolved data was collected for the H2O arcs, however due to the scale of the work required to perform this experiment time did not allow for time resolved work to be carried out on the LN_2 or C_2H_6O. This is because of the erratic behaviour of the arc, meaning that data has to be collected over and averaged period for each time window resulting in vast amounts of data.

The experiment could be improved in a number of ways, firstly a more focused OES could allow for spacial spectra to be acquired giving an understanding of data from one electrode to the other. It would also be interesting to image the arc using a high speed camera to view the evolution of the discharge. Lang et al [82] state that higher yield can be achived by using doped electrodes (with Y or Gd) was around 3 to 4 time higher, this would be an interesting experiment.

From the time resolved results it can be seen that Nanoparticles are predominately produced at the end of the arc. However higher currents do not always produce more material, this is due to variations in vapour pressure, and lifetime of the bubble.

It is worth noting that the arc discharge in liquids is erratic and is therefore difficult to precisely maintain the same gap between the electrodes. However common features and trends can be seen. Such features have been used here to form a time evaluation of the phenonenom and also get an introduction aboout reactions within the plasma.

Arc in liquids provide a much bigger challenge to characterise, added complexities such as joule heating of the liquid vapour, convective and conductive heat transfer, boundary conditions between the plasma and the liquid, bubble/liquid turbulence, make it difficult to model (although some have tried [83])

Ethanol produces more materials at lower currents due to addition Carbon feedstock in the ethanol molecules, and displays the same C2 bands as LN2 and H2O suggesting the nanoparticles are still formed by similar methods to those of the other liquids.

Chapter 4

Plasma Diagnosis

4.1 Introduction

In order to understand the processes involved in the modification of the carbon nanotubes it is paramount to characterise the plasma. Understanding the fundamental science behind plasma modification is important in order to consistently create reproducible work. The RF plasma, as discussed in chapter 2.1, used to functionalise the carbon nanotubes tubes has been characterised using a number of diagnosis methods. Current and voltage measurements have been taken from the driven electrode using an electronic sensors. Langmuir probes have been used to collect data from within the plasma such as V_p (plasma potential), V_f (plasma floating potential), n_e (electron density), T_e (electron temperature) etc. A capacitive probe has been employed to confirm some of the inferred data calculated from the langmuir probe measurements. Mass spectrometry was implemented to investigate potentials, fluxes, energies and ion species.

4.2 Plasma Analysis

4.2.1 Electrical Characteristics

Electrical measurements of the discharge parameters were taken in order to aid interpretation of the plasma discharge. The measurements were taken using current and voltage probes which where terminated at the 50Ω input of the digital oscilloscope. Equipment used is discussed in depth in chapter 2.1. Understanding the electrical characteristics are important as this will give an insight into how the system behaves

and will provide a good basis on which to build an understanding of the plasma mechanics. The probes were placed as close to the driven electrode as possible in order to minimise stray impedances. The results are shown in figures 4.1, 4.2, 4.3. The main variables of the system are pressure, power and plate distance. It is therefore important that an understanding of the plasma conditions is established for a variation of each parameter. For each of these variables measurements of RMS voltage applied (V_{rms}), RMS current in the system (I_{rms}) and the phase of the signal (ϕ) of the input was recorded.

Figure 4.1 shows how the I_{rms} and V_{rms} change with variation in electrode separation. It can be seen that there is little change in phase as a result of increasing the electrode separation (figure 4.1(c)). However, both I_{rms} and V_{rms} are effected. As plate distance increases from 20mm to 80mm the I_{rms} (figure 4.1(a)) increases at a rate of $0.004 V mm^{-1}$ and the V_{rms} (figure 4.1(b)) increases at a rate of $0.28 V mm^{-1}$. Once the electrode separation reaches 80mm the I_{rms} and V_{rms} saturate. As expected the electrical behaviour displayed here is characteristic of a capacitor. Changes due to pressure can be seen in figure 4.2, a very slight increase is seen (in both I_{rms} and V_{rms}), as the pressure increases from 1mTorr to 10mTorr after which there is a steady decrease as the pressure increases to 260mTorr, from 2.8A to 1.8A and 287V to 133V. The phase (from V_{rms} to I_{rms}) drops from -79° to -83° quite rapidly between 1mTorr and 15mTorr, as the pressure continues to increase the phase reamains quite constant at -83°. It can be seen that the current leads the voltage which is what would be expected of a capacatively coupled plasma.

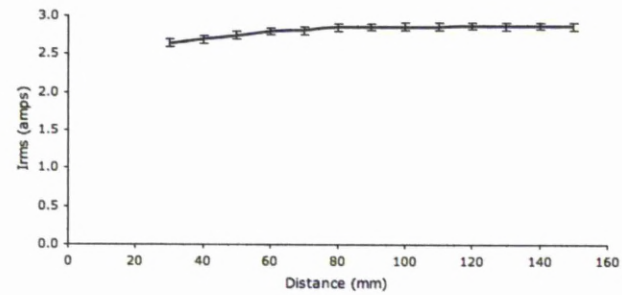

(a) I_{rms} vs Plate distance

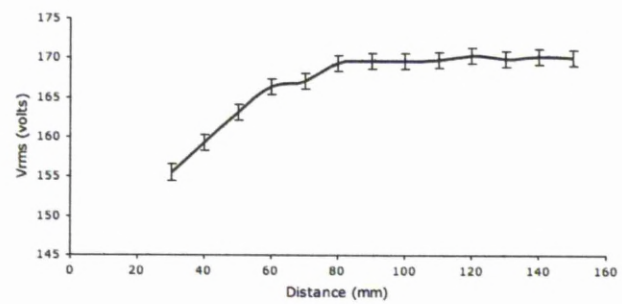

(b) V_{rms} vs Plate distance

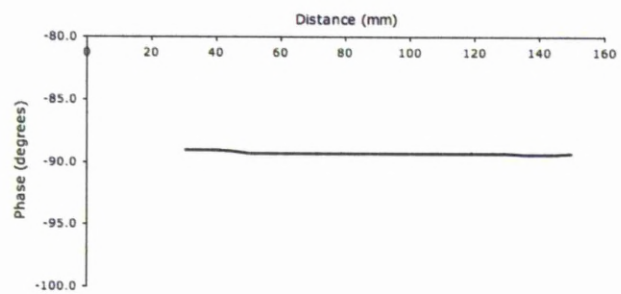

(c) Phase vs Plate distance

Figure 4.1: Change in (a) I_{rms} (b) V_{rms} and (c) phase for variation of electrode separation, at 10 Watts and 10 mTorr. (Error bars display variation of data from the mean and includes ±0.01A current probe resolution).

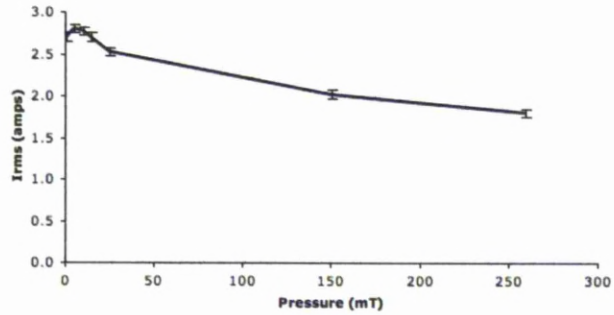

(a) I_{rms} vs Pressure

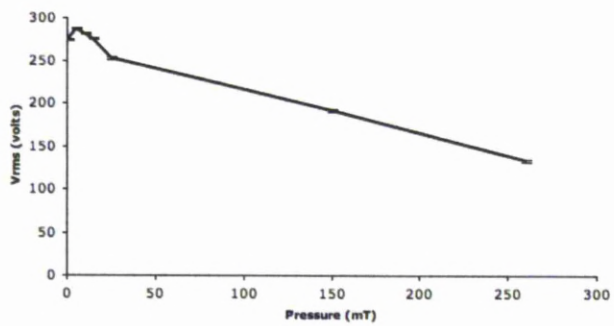

(b) V_{rms} vs Pressure

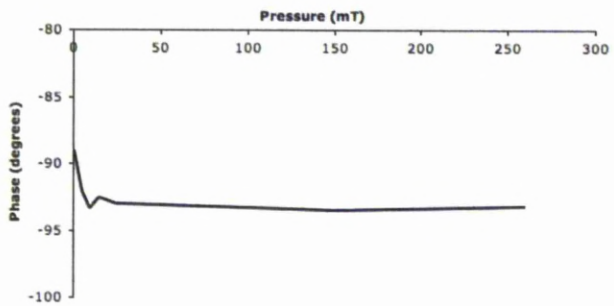

(c) Phase vs Pressure

Figure 4.2: Change in (a) current (b) voltage and (c) phase for variation of pressure, at 10 Watts and with a 6 cm electrode separation (Error bars display variation of data from the mean and includes ±0.01A current probe resolution).

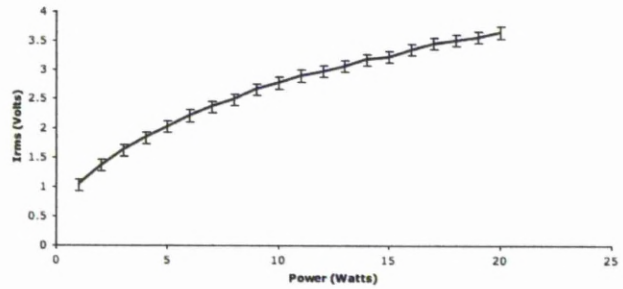

(a) I_{rms} vs Power

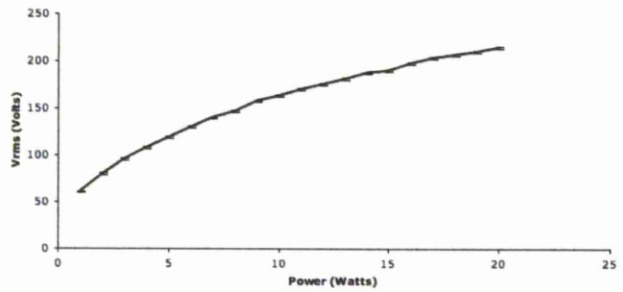

(b) V_{rms} vs Power

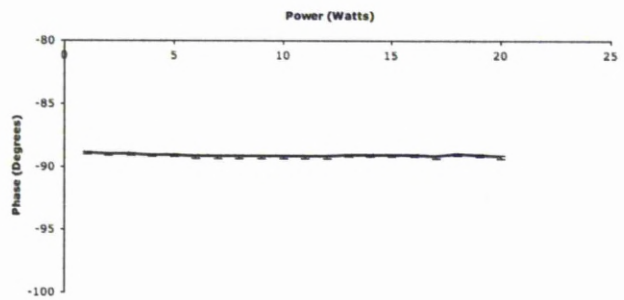

(c) Phase vs Power

Figure 4.3: Change in (a) current (b) voltage and (c) phase for variation of power, at 10 mTorr and with a 6 cm electrode separation (Error bars display variation of data from the mean and includes ±0.01A current probe resolution).

4.2.2 Langmuir probe results

As discussed in chapter 2.2 Langmuir probe measurements have been taken under all the same conditions of the electrical measurements (variation in plate distance, power and pressure). The Langmuir probe is a small current collecting intrusion into the plasma connected to a voltage ramp, the probes used in this work also contain active compensation as described in chapter 2.2.2. The measured currents in the probe tip will allow calculation of the physical plasma parameters. Shown in figure 4.4 are the results for variation in the experimental parameters, each curve is drawn from an average of twenty repeats in order to produce an accurate set of results.

From figure 4.4 a number of parameters can be read off the curve, V_f the floating potential is read of the I-V curves as the point were the current is zero, figure 4.5 shows the variation in floating potential for changes in plate distance, pressure and power.

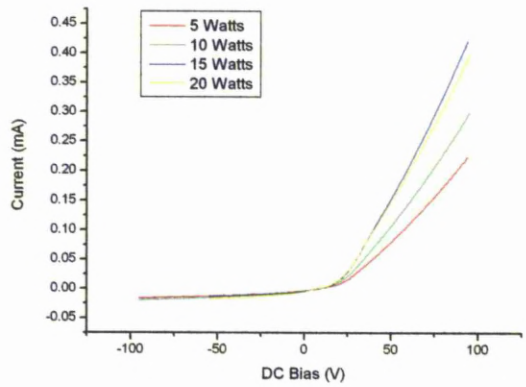

(a) IV for various Power at 10 mTorr and 6 cm electrode separation.

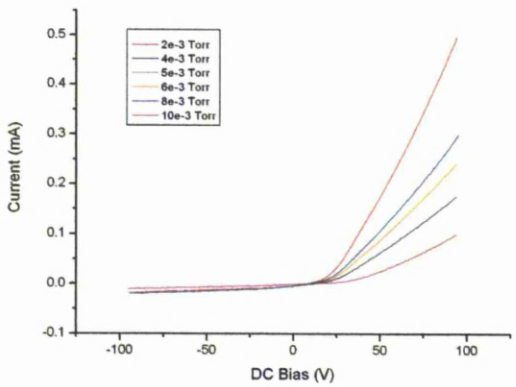

(b) IV for various Pressures at 10 Watts and 6 cm electrode separation.

Figure 4.4: Langmuir probe characteristics for N_2 plasma for (a) Power (b) Pressure (c) Electrode Separation with the probe tip at the centre of the plasma.

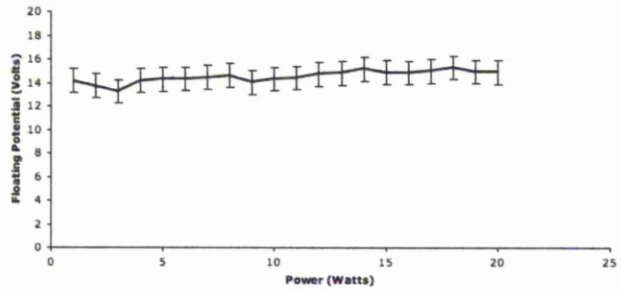

(a) Floating potential vs Power at 10 mTorr and 6 cm electrode separation.

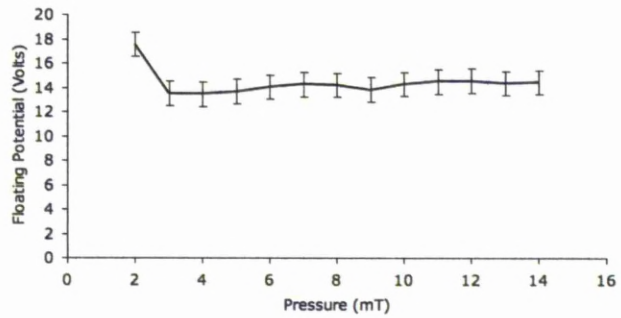

(b) Floating potential vs Pressure at 10 Watts and 6 cm electrode separation.

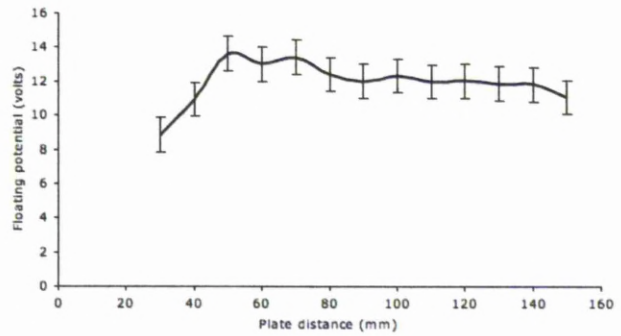

(c) Floating potential vs Electrode Separation at 10 Watts and 10 mTorr.

Figure 4.5: Change in floating potnetial N_2 plasma for (a) Power (b) Pressure (c) Electrode Separation with the probe tip at the centre of the plasma.

The plasma potential, V_p can be seen at the 'knee' of the I-V curve, however to determine a accurate value for the plasma potential the second derivative of the curve is taken. V_p is then the point where the second derivative crosses the x axis, fig 4.6.

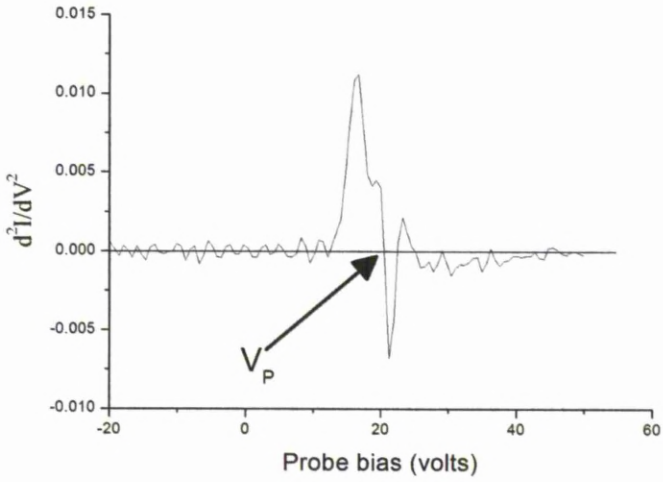

Figure 4.6: Example second derivative of I-V characteristic.

This then allows for V_p to be plotted against the plasma variables, figure 4.7. It must be noted that using the second derivative method to calculate V_p requires a clean probe tip as this method can be sensitive to noise. Cleaning the probe tip is done by either physically changing the tip or electronically within the plasma. To perform the latter method a very large bias is applied to the probe so that the surface is bombarded with ions effectively sputtering the any contaminants off probe surface.

Figure 4.7 shows that more power into the system does not result in changes in the plasma potential, this would be expected. The change in V_p due to variation pressure is largest but only between 3 to 5 mTorr after which it levels out. Change due to electrode distance is a small drop.

Knowing the plasma potential and the floating potential allows us to calculate the voltage drop across the driven electrode sheath, by subtracting the V_f from V_p, figure 4.8 shows this for change in plasma parameters.

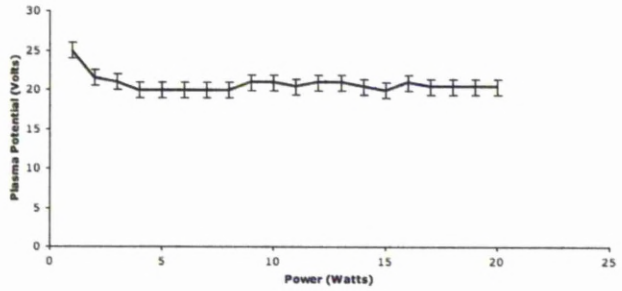

(a) Plasma potential vs Power at 10 mTorr and 6 cm electrode separation.

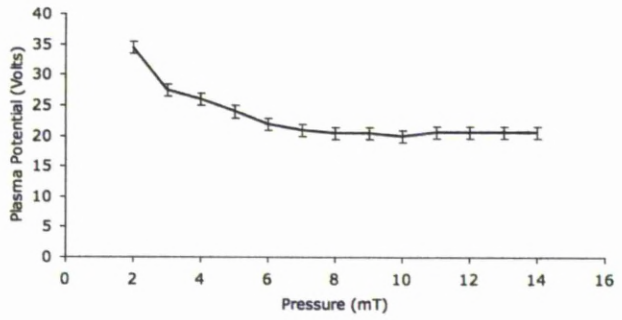

(b) Plasma potential vs Pressure at 10 Watts and 6 cm electrode separation.

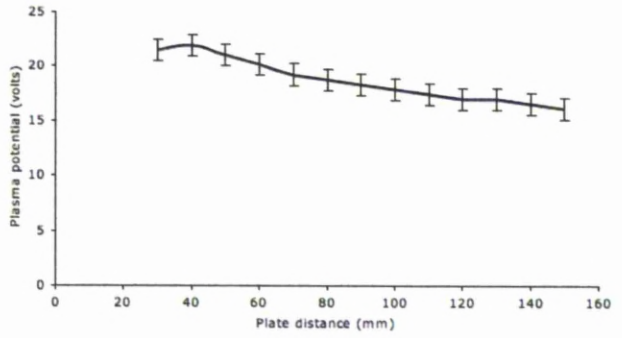

(c) Plasma potential vs Electrode Separation 10 mTorr and 10 Watts.

Figure 4.7: Change in plasma potential for N_2 plasma for (a) Power (b) Pressure (c) Electrode Separation with the probe tip at the centre of the plasma.

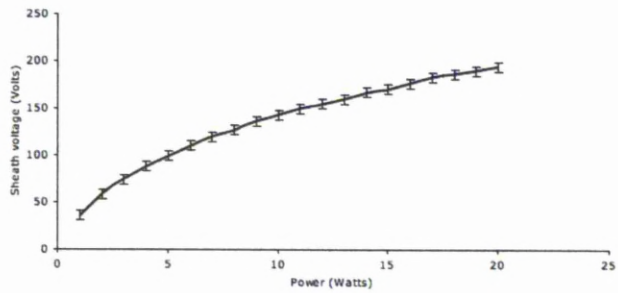

(a) Vsheath vs Power at 10 mTorr and 6 cm electrode separation.

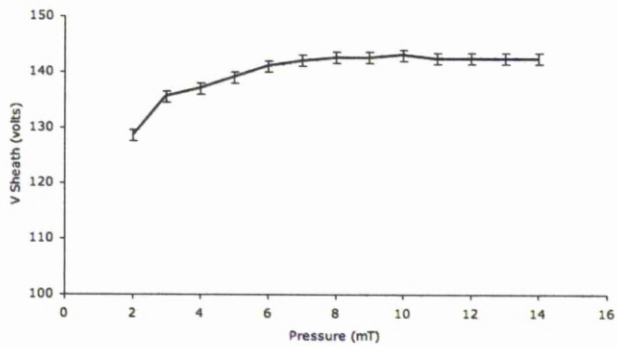

(b) Vsheath vs Pressure at 10 Watts and 6 cm electrode separation.

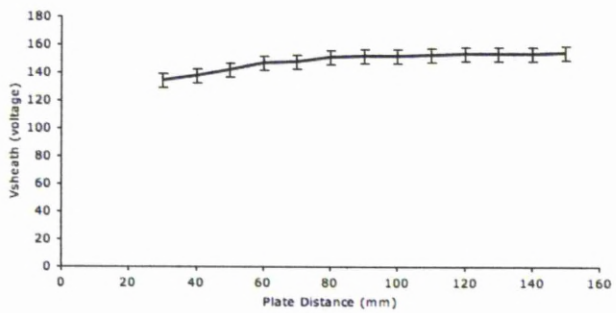

(c) Vsheath vs Plate distance at 10 mTorr and 10 Watts.

Figure 4.8: Change in drop across the driven electrode sheath for (a) Power (b) Pressure (c) Electrode Separation.

Figures 4.7, 4.5, 4.9, 4.10 show the variation in plasma properties calculated from the IV characteristics taken using the langmuir probe. It can be seen that like plasma potential T_e is not a function of power and that it is a function of pressure, T_e decreasing with increasing pressure due to lower mean free paths and therefore more collisions, fitting the global model for plasma. Figure 4.8 shows the voltage drop across the driven sheath.

From theory it is expected that;

$$5T_e \approx V_p - V_f \tag{4.1}$$

(4.2)

this can be seen to be experimentally correct from figure 4.11.

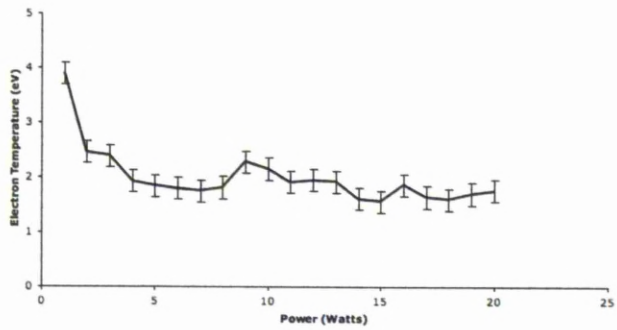

(a) Electron temperature vs Power at 10 mTorr and 6 cm electrode separation.

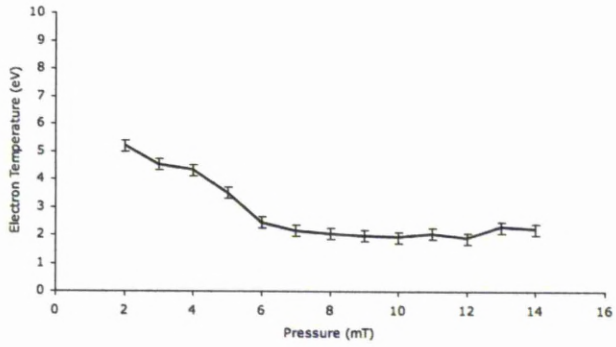

(b) Electron temperature vs Pressure at 10 Watts and 6 cm electrode separation.

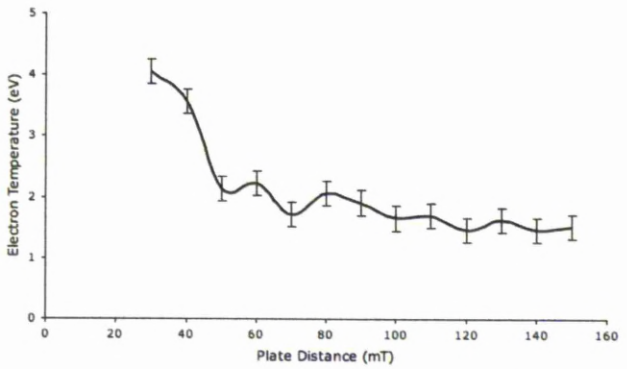

(c) Electron temperature vs Plate distance at 10 mTorr and 10 Watts.

Figure 4.9: Change in electron temperature in N_2 plasma for (a) Power (b) Pressure (c) Electrode Separation with the probe tip at the centre of the plasma.

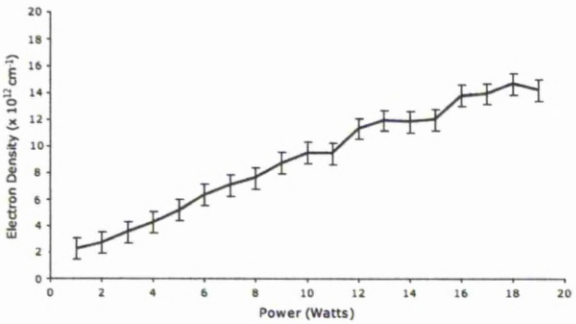

(a) Electron density vs Power at 10 mTorr and 6 cm electrode separation.

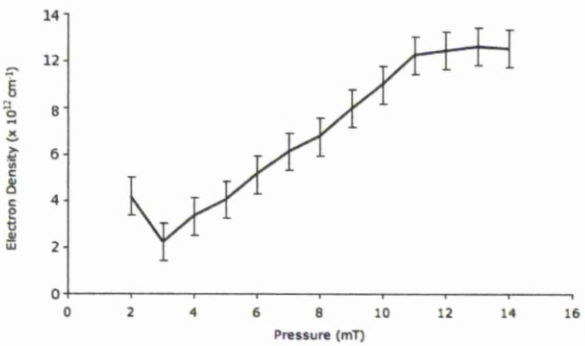

(b) Electron density vs Pressure at 10 Watts and 6 cm electrode separation.

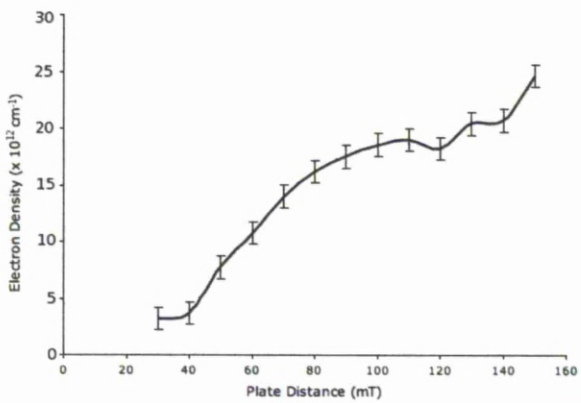

(c) Electron density vs Plate distance at 10 mTorr and 10 Watts.

Figure 4.10: Change in electron density in N_2 plasma for (a) Power (b) Pressure (c) Electrode Separation with the probe tip at the centre of the plasma.

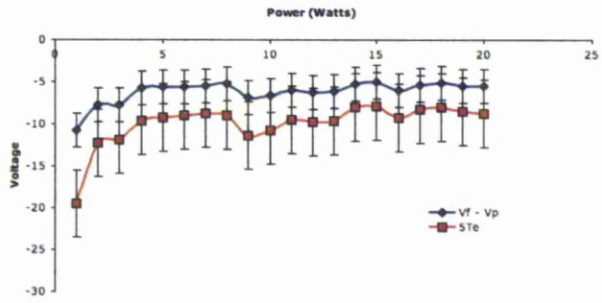

(a) $5T_e$ against V_P-V_f vs Power at 10 mTorr and 6 cm electrode separation.

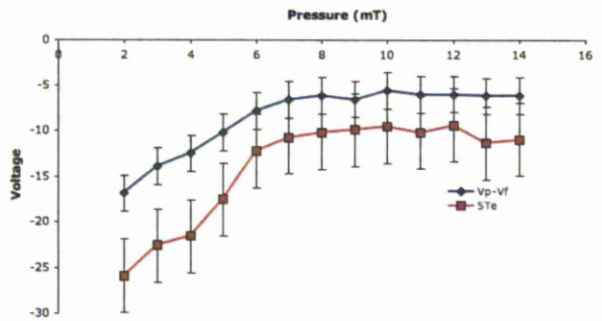

(b) $5T_e$ against V_P-V_f vs Pressure at 10 Watts and 6 cm electrode separation.

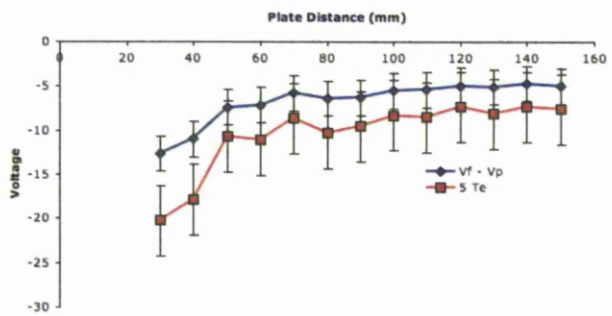

(c) $5T_e$ against V_P-V_f Plate distance at 10 mTorr and 10 Watts.

Figure 4.11: Comparison of $5T_e$ against V_P-V_f for various plasma conditions.

4.2.3 Capacitive Probe Analysis

The RF oscillation of the plasma potential, Vp(RF), can be measured directly by use of a capacitive probe (as well as being inferred by measuring the RF waveforms applied during langmuir compensation). The method used in this experiment is similar to that used in a number of other studies [34, 50, 51], and the experimetal details are discussed in chapter 2.3. The RF components in the plasma give rise to current flow in the unshielded probe tip which is detected by an oscilloscope. An un-calibrated example output waveform for the RF plasma can be seen in figure 4.12. By applying the calibration and doing fast fourier transform analysis lets us see the true harmonic components and their amplitudes, figure 4.12(b).

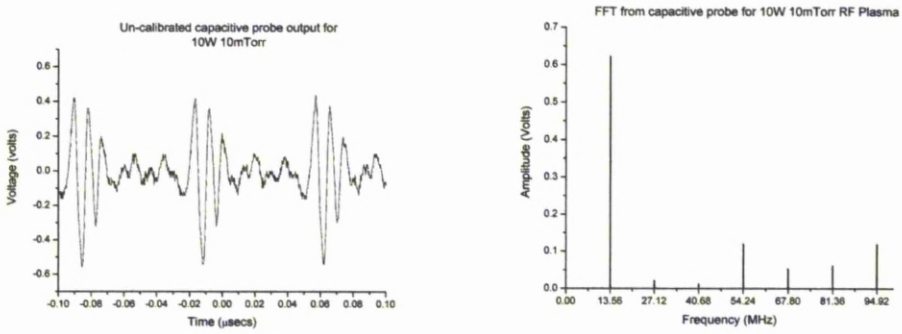

(a) Un-calibrated waveform

(b) Calibrated FFT

Figure 4.12: Un-calibrated 'raw' data from the capacitive probe a) and Calibrated FFT b), at 10 Watt, 10 mTorr plasma with a 6 cm electrode separation.

The effect on Vp(RF) of changing pressure and power can be seen in figures 4.13 and 4.14 respectively. The fundamental harmonic is clearly much larger than the higher harmonics and can be seen to increase with increasing power. A large dip can be seen in Vp(RF) as the pressure increases from 2 to 5mTorr, from this point however Vp(RF) increases to 1.06V. The fundamental plus six harmonics were measured, as shown in figure 4.12, however these are not shown in figures 4.13 and 4.14. The capactive probe results showed harmonics up to 11 (149.16MHz) and in some cases up to 24 (325.44MHz) however these have not been included as a known calibration signal could only be obtained up the 6th harmonic (94.92MHz). This technique does highlight the need for a greater range of harmonics when applying active compensation to the Langmuir

Probe, being able to compensate up to 6 harmonics would produce much more accurate results.

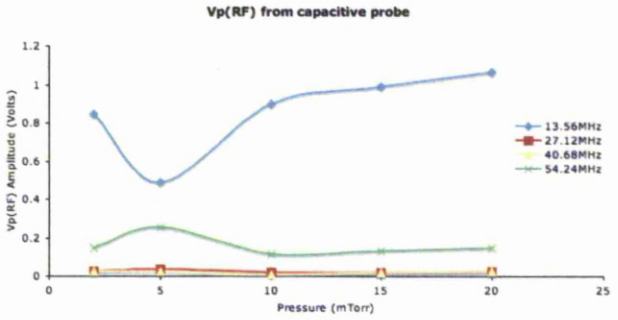

Figure 4.13: Variation in Vp(RF) for change in pressure at 10 Watt with a 6 cm electrode separation.

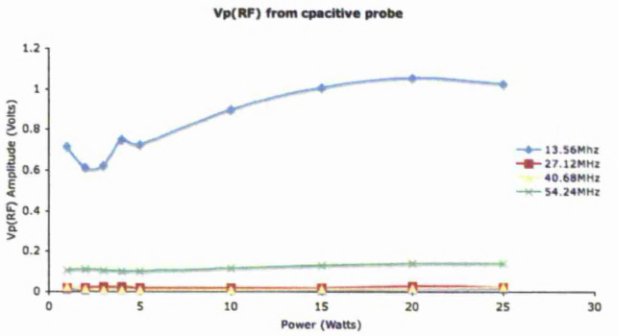

Figure 4.14: Variation in Vp(RF) for change in power at 10 mTorr plasma with a 6 cm electrode separation.

It is expected that V_{RF} is approximately equal to T_e however it can be seen that the total V_{RF} falls a little short of the values of T_e shown in figure 4.9. This maybe explained by the FFT shown in figure 4.12, some of the more influential harmonics are out of range of what can be corrected with the langmuir probe and due to limitations on the equipment used to calibrate the capacitive probe anything above 94.92 Mhz can not be measured. These results show that even though compensation up to the third harmonic was used to obtain the results, probe effects due to higher harmonics play an important part in the plasma properties.

4.3 Mass Spectrometry of a Capacitively Coupled RF Discharge

Understanding the particles and their fluxes arriving at the nanotube surface gives a greater understanding of the interactions between the plasma and carbon nanotubes. Energy resolved mass spectrometry was implemented to analyse the plasma parameters, such as V_p (plasma potential), ion energy and ion species. The mass spectrometer sorts the ions by there mass using a number of electric fields applied to the ions as they travel towards the sensors. The spectrometer used in this work is discussed in-depth in chapter 2.4 it is a Hiden Analytical EQP300 (fig 2.15) and is designed for energy and mass analysis of ions, neutrals and radicals generated in plasmas or for secondary ion mass analysis (SIMS). It allows detailed analysis of mass spectra, energy spectra of positive/negative ions, radicals and neutrals. The mass spectrometer end cap was place in the centre of the grounded electrode to allow analysis of particles at the grounded electrode.

4.3.1 Preliminary Work

Mass spectrometry of the RF Plasma allows for a greater understanding of the ion species and behaviour, as well as standard plasma properties such as V_p.

Using the mass spectrometer in the setup explained earlier Residual Gas Analysis (RGA) was performed to determine the background gases in the chamber at base pressure and operating pressure before excitation. To do this the the inbuilt ion source is used. This allows a more detailed understanding of the vacuum within the constructed rig.

In order to produce accurate results the machine must be re-tunded to view each species contained within the plasma. To do this each species must be known before any other work can take place, taking a scan over the full range will show all the species present and will give understanding when tuning the EQP, the results of which are shown in table 4.1.

Figure 4.15, shows a scan tuned to 14 AMU, showing all of the present species, viewing this on a log scale shows the lower intensity species.

Using 'cracking patterns' it is possible it identify each individual species. When the

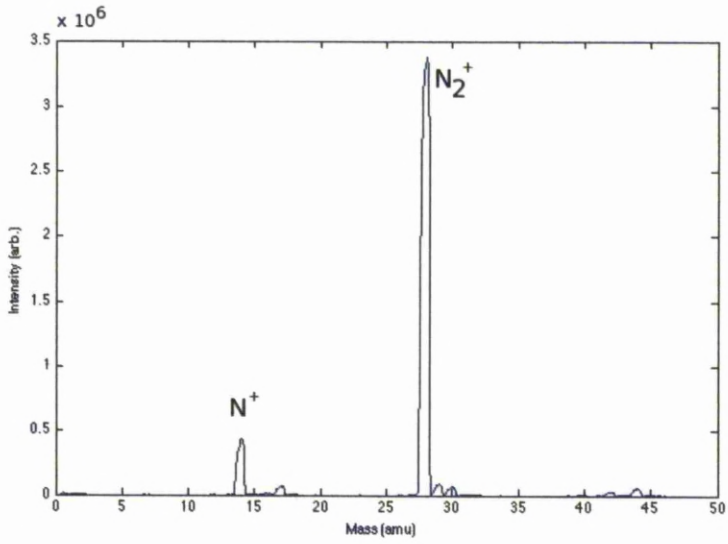

Figure 4.15: Comparative scan over the full mass range, demonstrating raw data from the EQP 300. Tuned to 28 amu, with the plasma running at 6 cm, 10 Watts, 10 mTorr

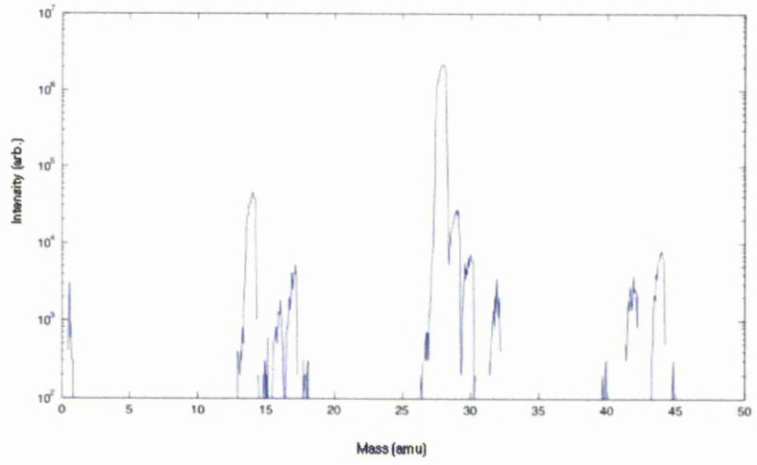

Figure 4.16: Comparative scan over the full mass range, for a log of figure 4.15. Considerable more masses are visible by scaling the y axis, this allows the true particle content to be observed. A table showing line assignment is shown on the next page.

molecules become ionised fragments of several mass to charge rations are created. These mass to charge values produce unique finger prints for each gas species [84]. Giving a main peak at the mass of the molecule and then further peaks for the fragments. These fragments are caused due to disassociation, and multiple ionisation's. To give a simple example Carbon Monoxide would have a mass of 28 amu which is the same as Nitrogen however, the fragments and ratios would be different. CO has three fragments, 12 amu at 5% of the main peak, 16 amu at 2% of the main peak and 14 amu at 1% of the main peak. Whereas N_2 has only two fragments, 14 amu at 5% of the main peak and 29 at 1% of the main peak. An understanding of these cracking patterns enables one to identify various species from the acquired data. Using this technique the following data in table 4.1 was obtained from figure 4.16.

Table 4.1: Table showing mass' observed in the nitrogen RF capacitively coupled plasma

Mass (amu)	Element		Mass (amu)	Element
0.5	CN		29	N
1	H		30	
13			31	
14	N		32	O_2
15	N^{15}		40	
16	O		42	
17	H_2O		44	OIL
18	H_2O		46	
28	N_2		45	

Amongst the expected nitrogen, there is also carbon nitride, hydrogen, oxygen, moisture and some motor oil. Low levels of motor oil can be expected to be found in vacuum systems working in 10^{-7} mTorr range when using rotary pumps to rough out the chamber. A small amount of moisture is also present and can be further reduce by baking out the chamber before experiments. Rotary pump oil can be further reduced by fitting a cold trap and a foreline trap to prevent any oil particles from entering the process chamber. Figure 4.16 shows that oil and water are between 100 and 1000 order of magnitude lower than the process gas, nitrogen. This, respectively, constitutes acceptable levels of contaminates within the plasma species. The presence of hydrogen can be attributed to the relatively lower efficiency of turbomolecular pumps for pumping

hydrogen atoms, this means even after the Hydrogen in the air has been removed any hydrogen desorped from the stainless steel walls will take longer to be pumped from the system than other molecules. N^{15} is also detected, this is one of only two stable isotopes of nitrogen (the other being N^{14}) and consists of 7 protons and 8 neutrons. This information will now allow the machine to be optimised for recording mass spectra of the RF plasma.

4.3.2 Variation of Species Under Different Conditions

Results shown will focus upon the active nitrogen species within the plasma in order to determine the optimum processing parameters for functionalising carbon nano particles. Figure 4.17 to 4.19 show the variation in power, pressure and plate distance for N_2 amu 28, this, as shown in figure 4.15, is the main nitrogen content within the plasma. As would be expected based upon the electrical and langmuir probe characteristics there is a clear increase in counts as power in the system is increased. The increase of pressure however produces a more dense plasma with a lower free mean path and consequently the counts drop due to more collisions within the bulk plasma. Highest counts are seen for all species between 3-4 cm plate distance whilst the highly dense discharge created at 2cm plate distance had the 75% lower counts than the other conditions presented.

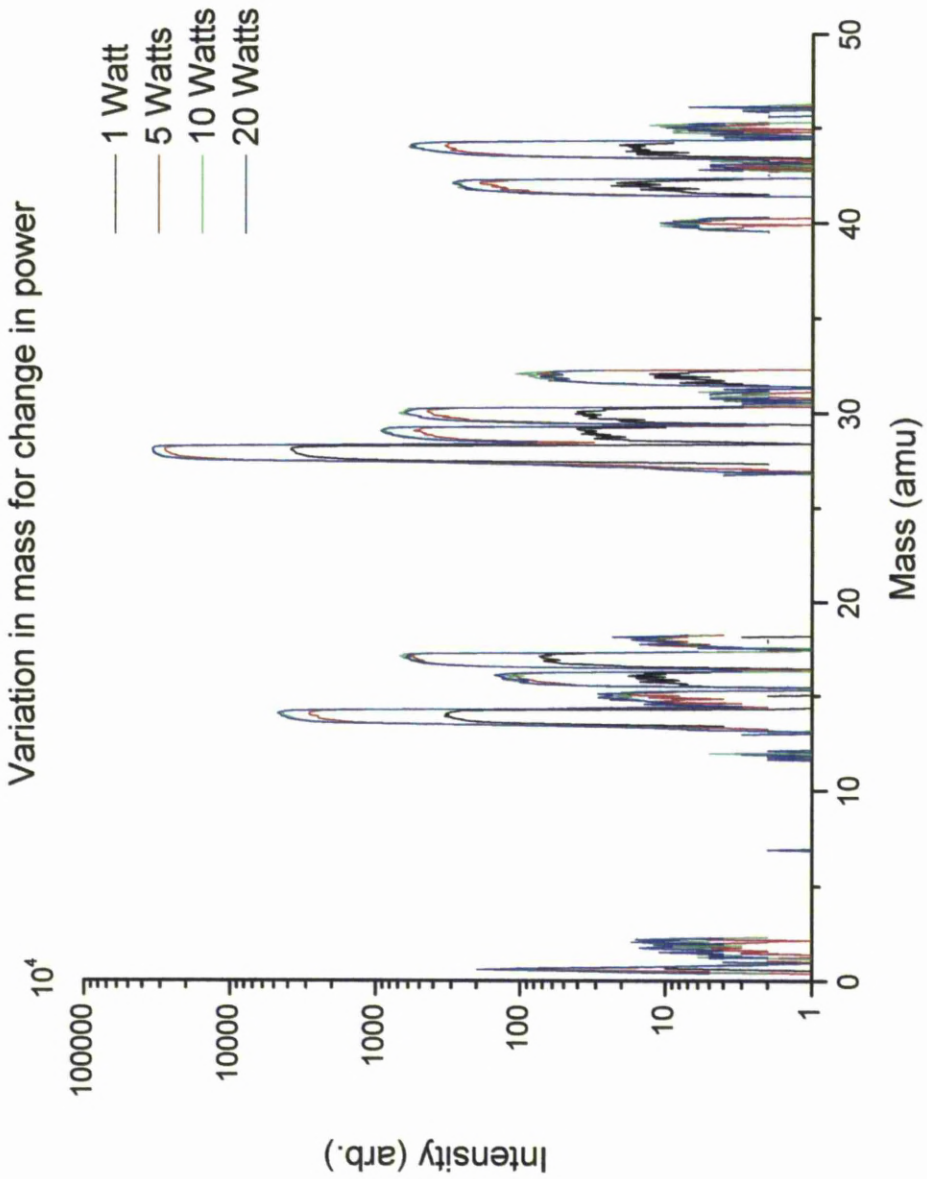

Figure 4.17: Variation in mass for change in power at 10 mTorr and 6 cm electrode spacing.

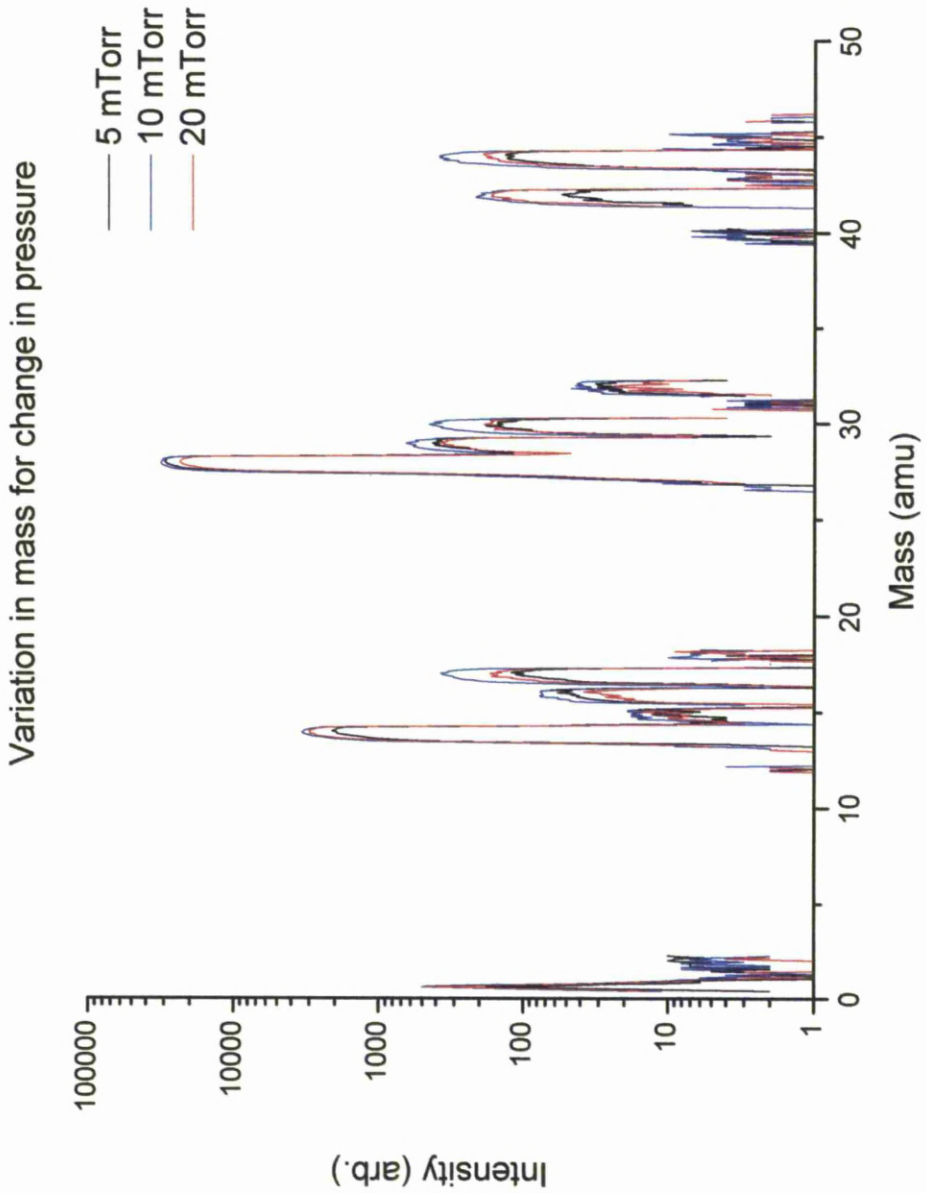

Figure 4.18: Variation in mass for change in pressure at 10 Watts and 6 cm electrode spacing.

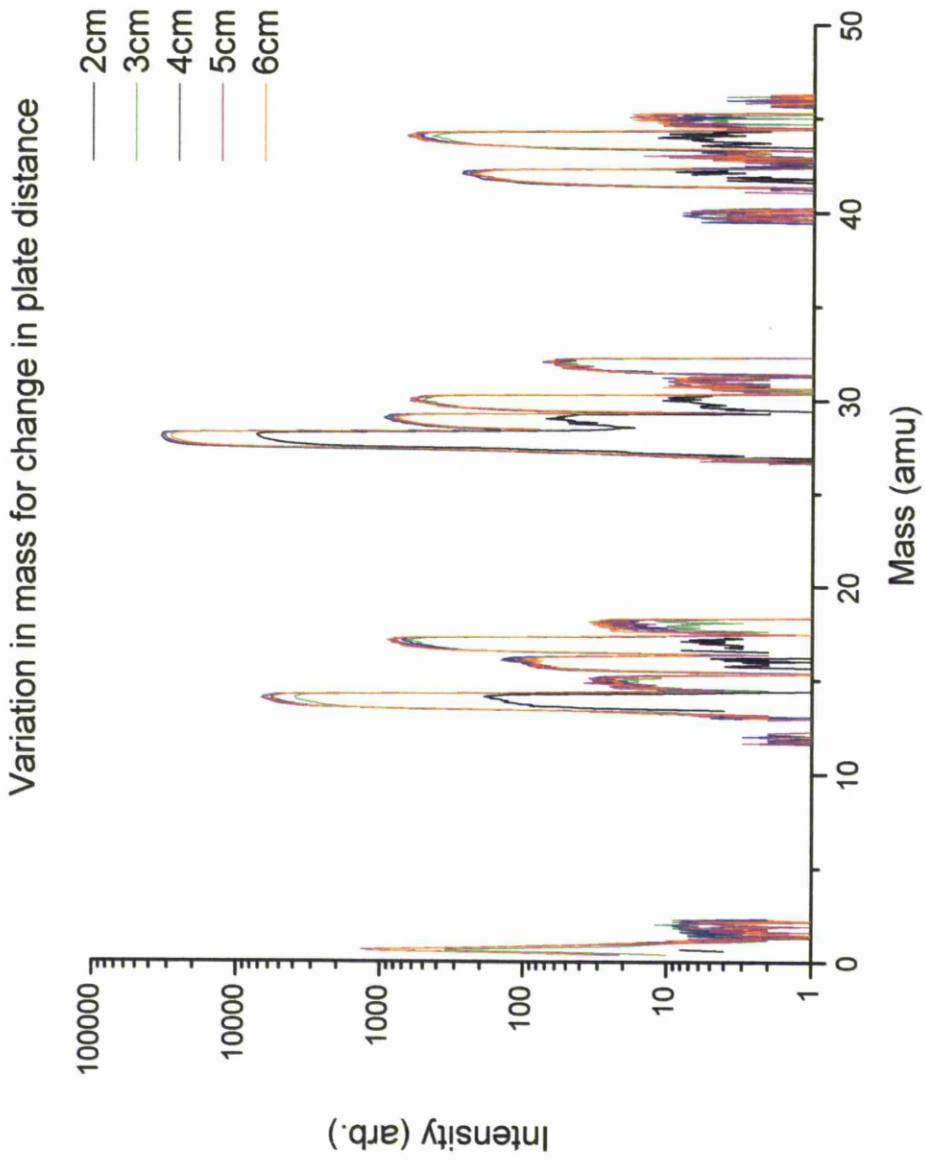

Figure 4.19: Variation in mass for change in electrode spacing at 10 mTorr and 10 Watts.

The collisions which take place within the RF nitrogen discharge can be seen in figure 4.20.

e^- collisions		
$e^- + N_2 \rightarrow 2e^- + N_2^+$	electron-impact ionization	$\sigma(E)$
$e^- + N_2 \rightarrow e^- + N_2^*$	electron-impact excitation to $A^3\sigma_u^+$	$\sigma(E)$
$e^- + N_2 \rightarrow e^- + N_2^*$	electron-impact excitation to $B^3\Pi$	$\sigma(E)$
$e^- + N_2 \rightarrow e^- + N_2^*$	electron-impact excitation to $C^3\Pi$	$\sigma(E)$
$e^- + N_2 \rightarrow e^- + N_2^*$	electron-impact excitation to $a^1\Pi_g$	$\sigma(E)$
$e^- + N_2 \rightarrow 2e^- + N^+ + N$	dissociative ionization	$\sigma(E)$
$e^- + N_2 \rightarrow e^- + N + N$	dissociation	$\sigma(E)$
$e^- + N_2^+ \rightarrow N + N$	dissociative recombination	$k = 4.8 \times 10^{-13}\sqrt{300/T_e}$
N^+ collisions		
$N^+ + N_2 \rightarrow N^+ + N_2$	elastic scattering	$\sigma(E)$
$N^+ + N_2 \rightarrow N + N_2^+$	charge transfer	$k = 4 \times 10^{-17}$
$N^+ + N \rightarrow N^+ + N$	elastic scattering	$\sigma(E)$
$N^+ + N \rightarrow N + N^+$	charge transfer	$k = 4 \times 10^{-17}$
N_2^+ collisions		
$N_2^+ + N_2 \rightarrow N_2^+ + N_2$	elastic scattering	$\sigma(E)$
$N_2^+ + N_2 \rightarrow N_2 + N_2^+$	charge transfer	$k = 1 \times 10^{-17}$
$N_2^+ + N \rightarrow N_2^+ + N$	elastic scattering	$\sigma(E)$
$N_2^+ + N \rightarrow N_2 + N^+$	charge transfer	$k = 1 \times 10^{-17}$

Figure 4.20: Chemical reactions taking place within an N_2 Plasma, taken from [85].

4.3.3 Ion Energy Distribution Functions (IEDFs)

Ion energy distributions for ions at the grounded electrode were measured using the Hiden EQP 300 according to chapter 2 and are given for the Nitrogen species within the plasma. The opening to the mass analyser was placed in the centre of the grounded electrode and as such all measurements are with reference to ground.

Figure 4.21, 4.22, 4.23 shows the ion energy distribution function for change in the various plasma parameters. Each distribution peaks at the plasma potential (V_p) and tails off to the maximum potential within the plasma. At this point the distribution contains the ions with the highest possible energies. This is due to the RF field effect, explain in chapter 1, whereby a if a particle was to be at it's maximum velocity and was reversed due to a collision could reach higher energies. This is also the case for a small proportion of ions with lower energies than V_p, (only in reverse), however if this was the only reason for lower energy ions, than the peak energy (Vp), then a the energy distribution would have a more symmetrical shape. This means that these lower energy ions must be created within lower energy regions of the plasma, i.e. the plasma sheath. That is to say that any ions with a lower energy than the plasma potential will have been created within the sheath or pre-sheath. The shift in energy distribution peak should align with the V_P measured from the Langmuir probe results as shown in section 4.4.

4.4 Comparison to Langmuir Probe Results

The langmuir probe and and mass spec results are in good agreement as can be seen in 4.28. It must be noted that due to the configuration within the chamber the largest electrode separation possible with the mass spec in place was 6 cm.

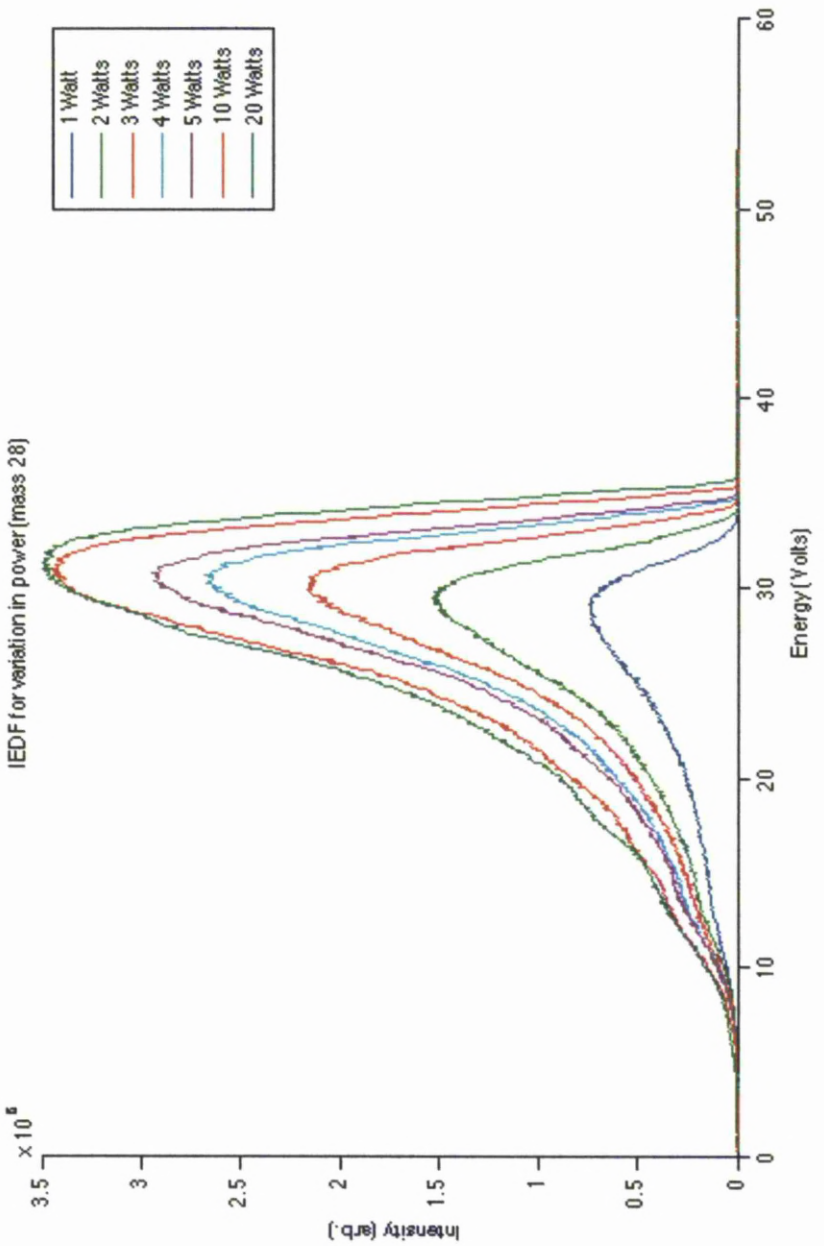

Figure 4.21: Variation in N_2^+ IEDF for change in power at 10 mTorr and 6 cm electrode spacing.

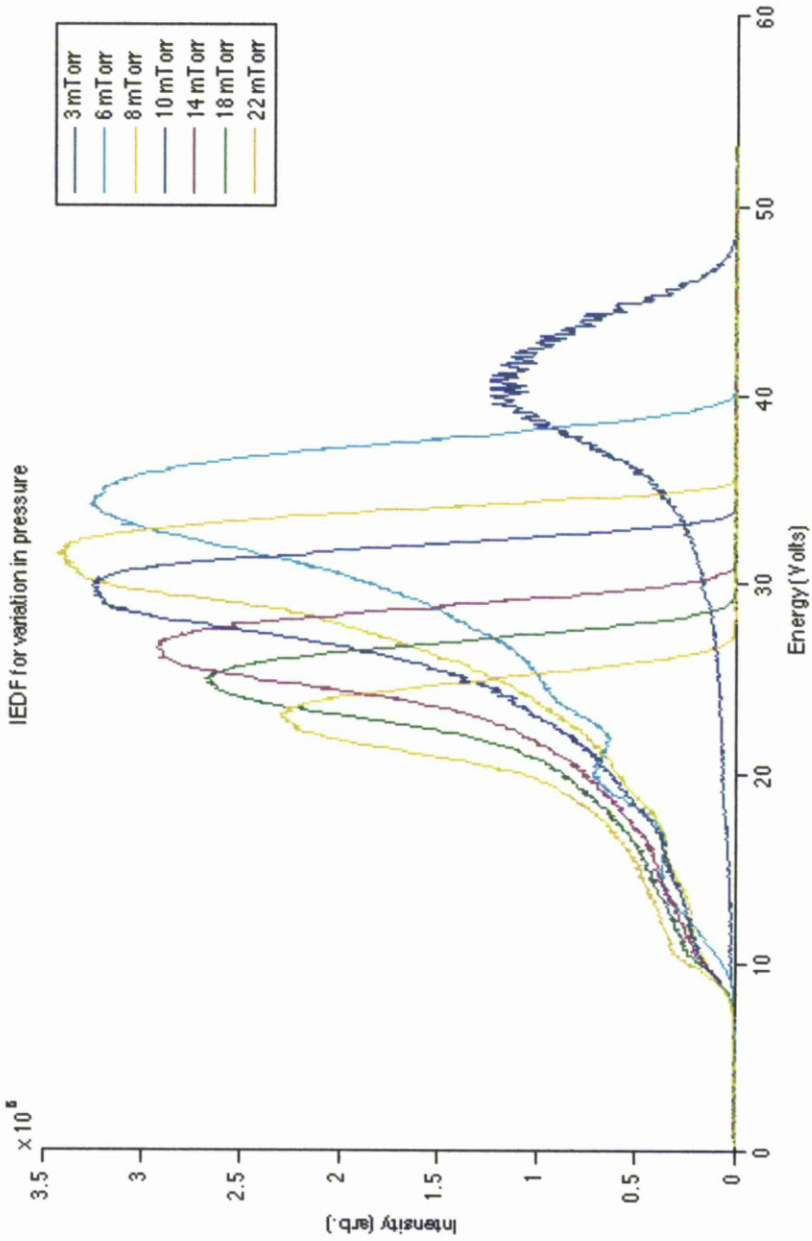

Figure 4.22: Variation in N_2^+ IEDF for change in power at 10 Watts and 6 cm electrode spacing.

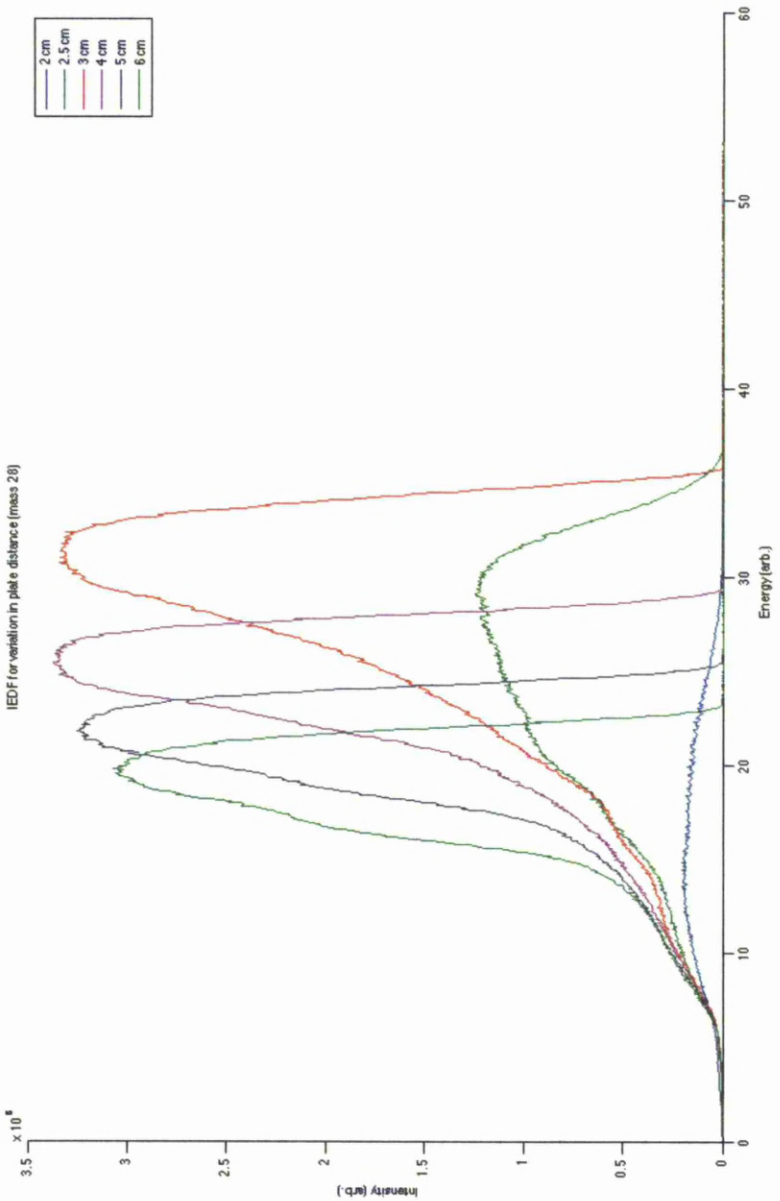

Figure 4.23: Variation in N_2^+ IEDF for change in power at 10 mTorr and 10 Watts.

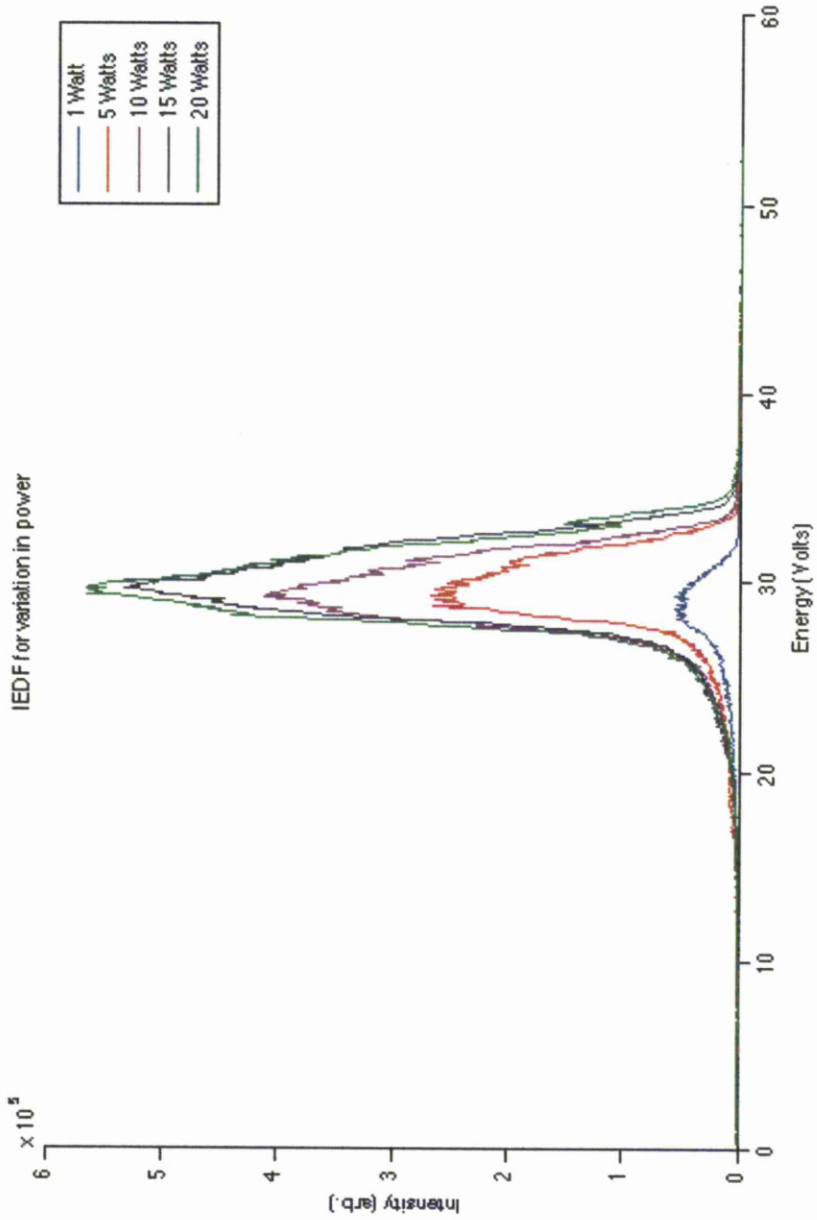

Figure 4.24: Variation in N^+ IEDF for change in power at 10 mTorr and 6 cm electrode spacing.

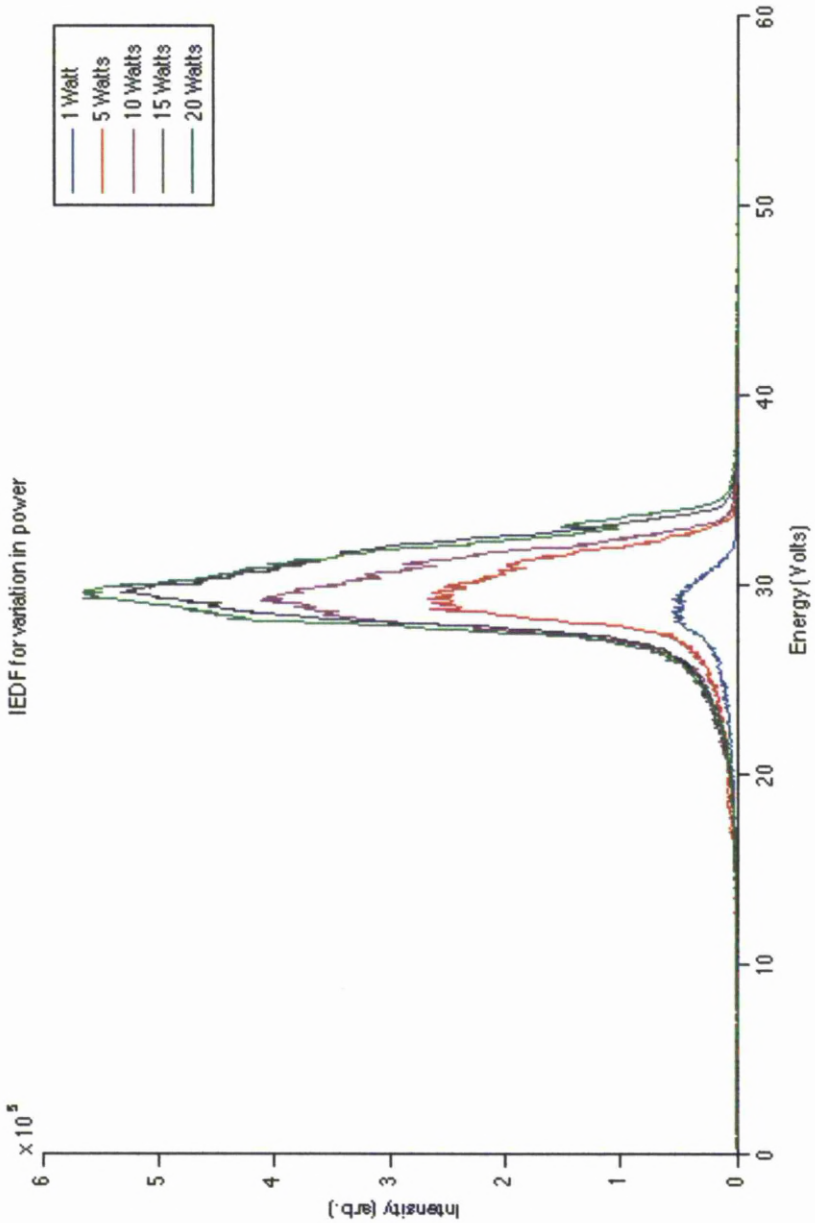

Figure 4.25: Variation in N^+ IEDF for change in pressure at 10 Watts and 6 cm electrode spacing.

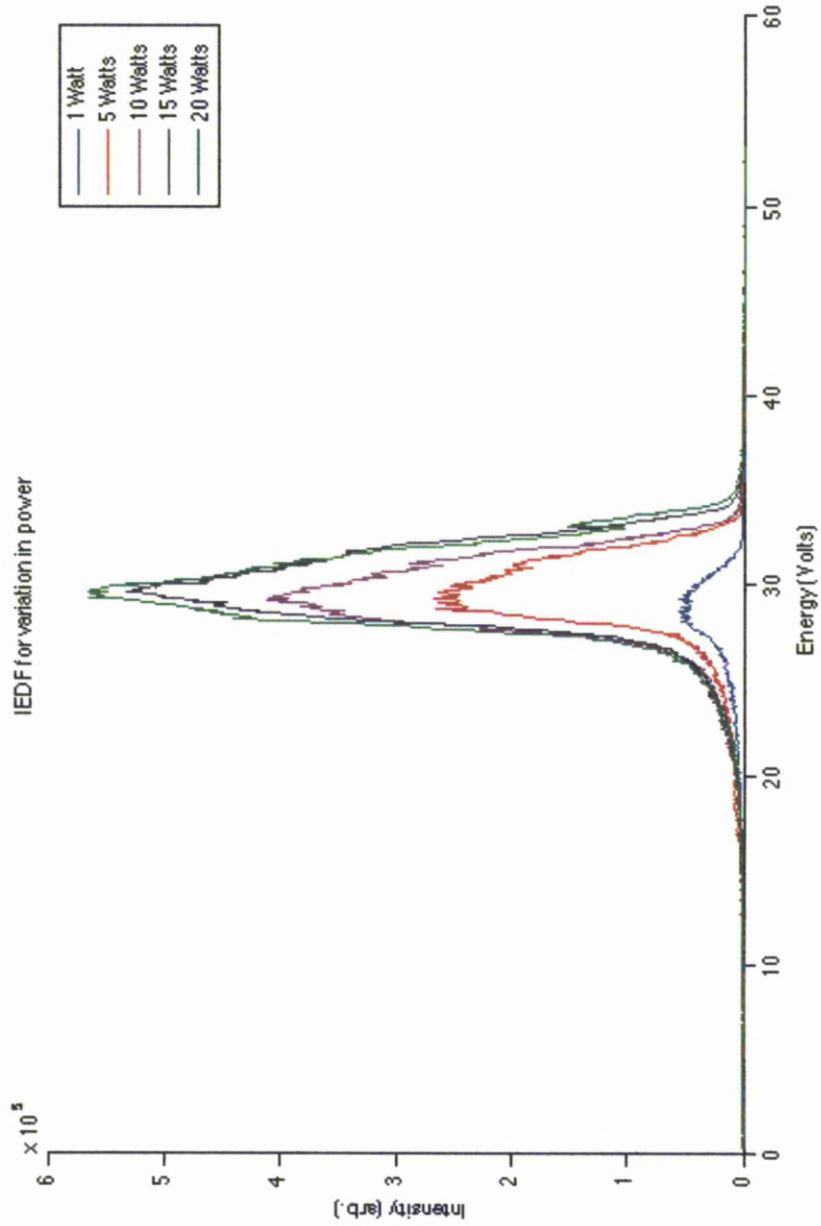

Figure 4.26: Variation in N^+ IEDF for change in electrode separation at 10 mTorr and 10 Watts.

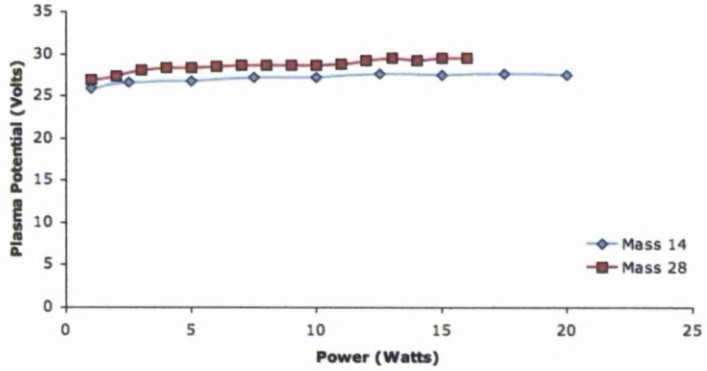

(a) Variation in N_2^+ and N^+ V_p for change in power at 10 mTorr and 6 cm electrode spacing.

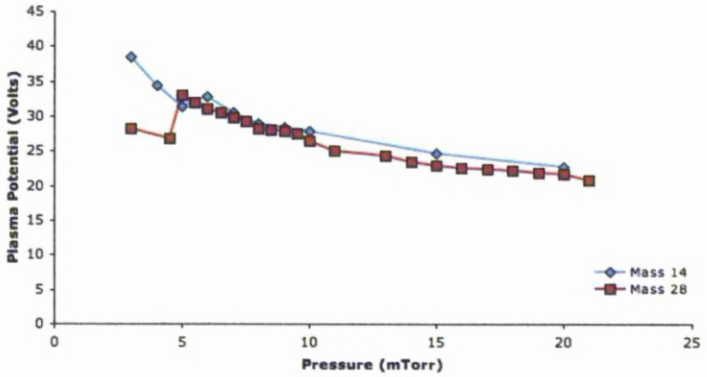

(b) Variation in N_2^+ and N^+ V_p for change in pressure at 10 Watts and 6 cm electrode spacing.

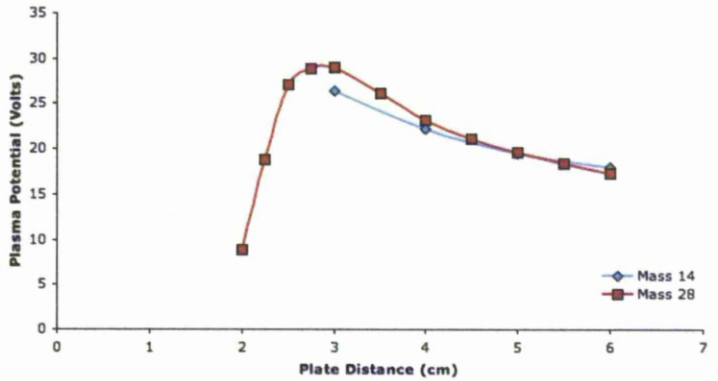

(c) Variation in N_2^+ and N^+ V_p for change in electrode separation at 10 mTorr and 10 Watts.

Figure 4.27: Change N_2 V_p with a) power b) pressure and c) plate distance, comparing N_2^+ and N^+ V_p.

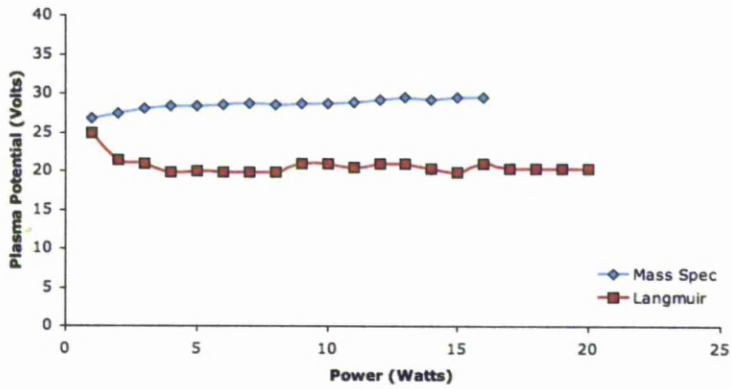

(a) Variation between Langmuir probe V_p and Mass Spec V_p (N_2^+ and N^+) for change in power at 10 mTorr and 6 cm electrode spacing.

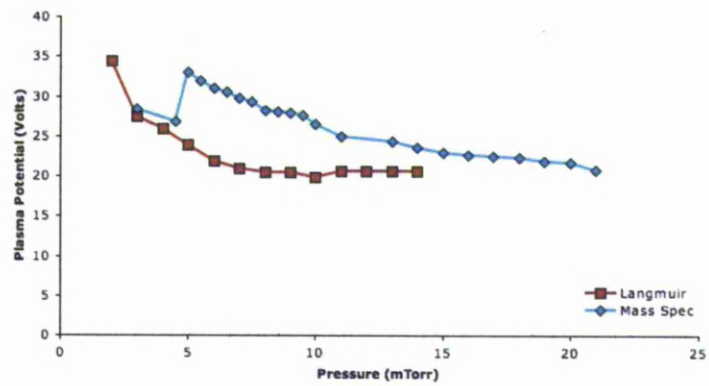

(b) Variation between Langmuir probe V_p and Mass Spec V_p (N_2^+ and N^+) for change in electrode separation at 10 mTorr and 10 Watts.

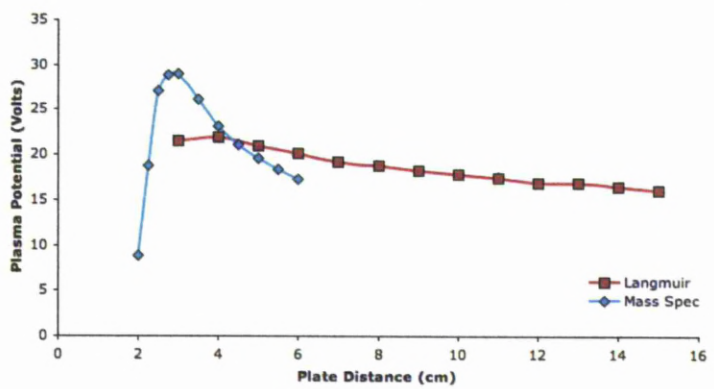

(c) Variation between Langmuir probe V_p and Mass Spec V_p (N_2^+ and N^+) for change in electrode separation at 10 mTorr and 10 Watts.

Figure 4.28: Change N_2 V_p with a) power b) pressure and c) plate distance compared to langmuir probe data

4.4.1 Ion Transient Time

It has been described in numerous other works that a bimodal ion energy distribution is often observed.

In collisionsless sheaths the crucial parameter determining the shape of the IEDs is

$$\tau_{ion}/\tau_{rf} = \omega/\omega_{ion} \tag{4.3}$$

where

$$\tau_{rf} = 2\pi/\omega \tag{4.4}$$

is the RF period and

$$\tau_{ion} = 2\pi/\omega_{ion} \tag{4.5}$$

is the time an ion takes to traverse the sheath when the sheath drop is at it's DC value, were the plasma frequency is given by

$$\omega_{ion} = \sqrt{\frac{ne^2}{\varepsilon_o m_{ion}}} \tag{4.6}$$

$$\tau_{ion}/\tau_{rf} = 3s\omega/2\pi(m/2es)^{1/2} \tag{4.7}$$

When

$$\tau_{ion}/\tau_{rf} << 1 \tag{4.8}$$

then the ions cross the sheath in a small fraction of the RF cycle and respond to the instantaneous sheath voltage, and therefore their final energies depend upon the phase of the RF cycle in which they enter the sheath. This results in a broad bimodal IEDF with each peak corresponding to the minimum and maximum voltage drops across the sheath. However when

$$\tau_{ion}/\tau_{rf} >> 1 \tag{4.9}$$

the ions take a long time to traverse the sheath and no longer respond to the instantaneous sheath voltage only responding to the time averaged sheath voltage, meaning

that the phase of the cycle in which they enter the sheath becomes unimportant resulting in a narrow IEDF. It is therefore possible to calculate from Langmuir probe results weather a bimodal distribution is to be expected.

The ion transient time must be calculated to calculate if a bimodal distribution is expected.

Sheath thickness,

$$\overline{s} = \sqrt{2/3}\lambda_{DE}(2V_o/T_e)^{3/4} \tag{4.10}$$

Where

$$\lambda_{DE} = (\epsilon_o T_e/en_e)^{1/2} \approx 740\sqrt{T_e/n_e} \tag{4.11}$$

and

$$\omega = 2\pi f \tag{4.12}$$

Figures 4.29(b) and 4.29 show that the ion transient time is always greater than one and therefore fits the condition 4.9 whereby a single peak distrobution is expected, which agrees with the experimental results collected using the mass spectrometry.

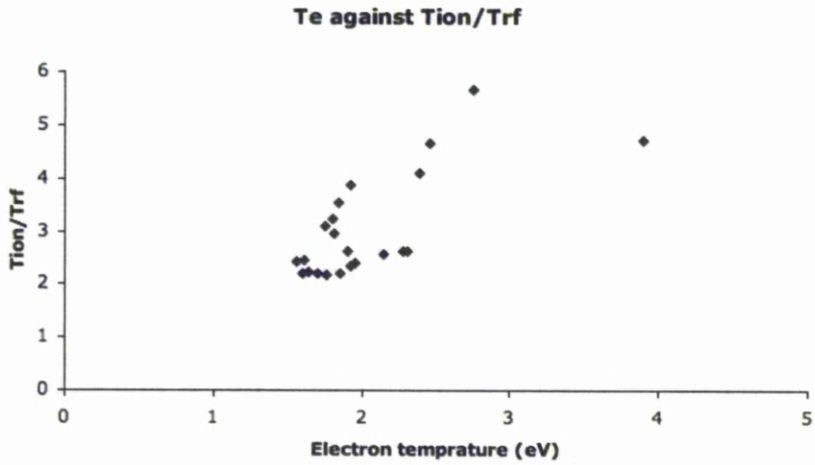

(a) Tion/Trf against plasma electron temperature.

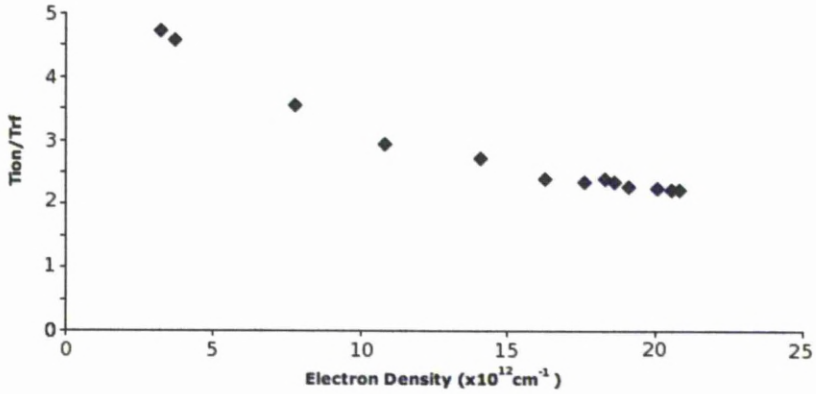

(b) Tion/Trf against plasma electron density.

Figure 4.29: Change Tion/Trf against a) Electron temprature and b) electron density

4.4.2 Correction of IEDF

The IEDF shown in the previous section only apply to a grounded surface due to the grounded orifice of the Mass Spectometer whereas the nanotubes to be exposed to the plasma sit on a silicon substrate which will insulate the tubes from ground. This means that the nanotubes exposed to plasma will be at a unknown floating potential. Unfortunately however due to the geometry and construction of the Mass Spectrometer floating the orifice is impossible and therefore in order to obtain a IEDF which is relative to the nanotubes corrections to the IEDF measured must be made. To do this the floating potential of a sample must be applied to the IEDFs, to do this the floating potential at the ground plate is measure directly using small floating disk probes on the grounded electrode.

Knowing the floating potential of the sample, self bias for 1mm above ground electrode, lets us shift the IEDFs in order to observe the bombardment energy for nanotubes on an insulted surface within the sheath. Correction values for each IEDF sweep shown in figure 4.31.

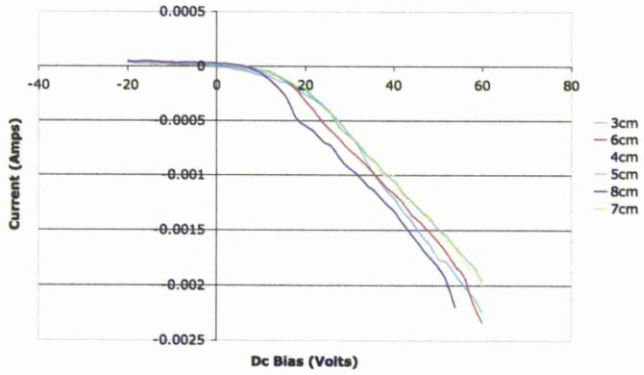

(a) DC Sweep of insulated surface at grounded electrode for plate distance with 10 mTorr 10 watts plasma.

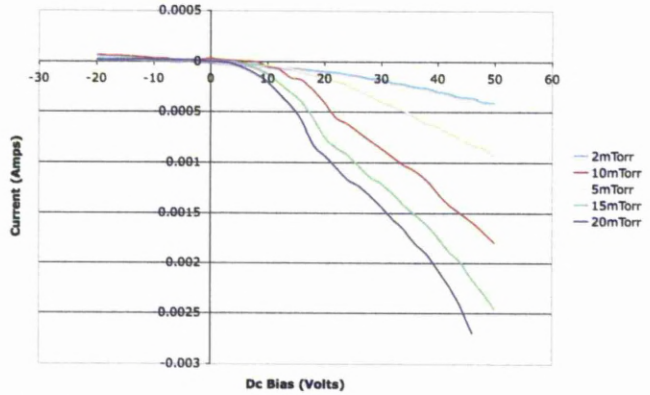

(b) DC Sweep of insulated surface at grounded electrode for pressure with 6 cm 10 watts plasma.

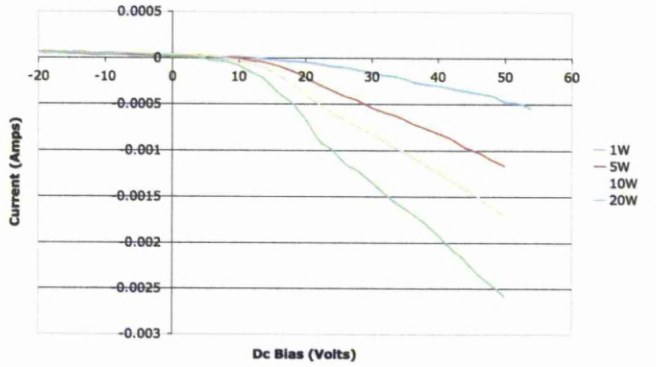

(c) DC Sweep of insulated surface at grounded electrode for power with 6 cm 10 mTorr plasma

Figure 4.30: DC Sweep of insulated surface at grounded electrode for, a) Plate distance b) Pressure and c) Power

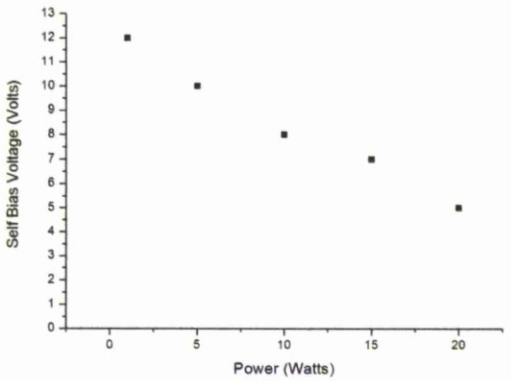

(a) Self bias for change in power at 10 mTorr and 60 mm electrode separation.

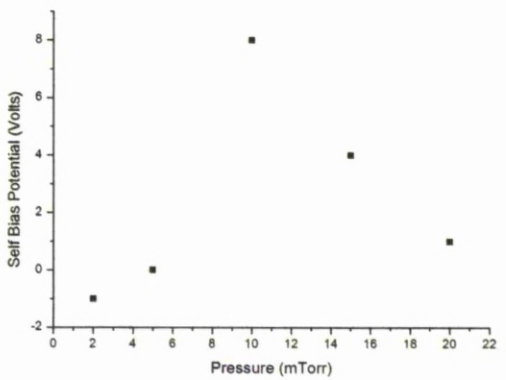

(b) Self bias for change in pressure at 10 Watts and 60 mm electrode separation.

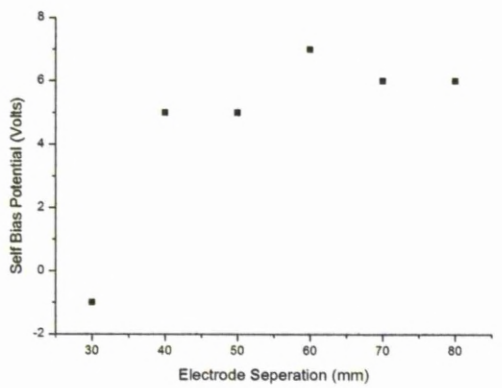

(c) Self bias for change in electrode separation at 10 mTorr and 10 Watts.

Figure 4.31: Self Bias of insulated surface 1 mm above grounded electrode for, a) Plate distance b) Pressure and c) Power

4.4.3 Plasma Analysis Summary

Analysis of the plasma RF plasma (at 13.5Mhz) has taken place, giving a greater understanding of the physical processes that take place. This detailed analysis of the system confirms that the plasma system designed operates correctly and the RF plasma generated within it behaves as expected and compares well to with literature [32–34,86].

From the analysis carried out here the physical properties of the plasma have been correlated to the operating parameters this allows plasma properties to be selected by changing system variables. For instance at 10 W, 6 cm plate distance and at 10 mTorr the plasma properties would be; V_f = 14 V, V_p = 20V V_{sheath} = 145 V T_e = 2eV n_e = 10^{12} cm^{-1} and specificly for N^+; V_p = 26 V and N_2^+ = 24 V and most importantly the ion transient time (t_{ion}/t_{rf}) >1. This should allow for tuning to the plasma via the system properties to select a plasma regime which will not cause damage to the nanotube, due to a large energies, or limited bombardment, due to low energies.

It has also been shown however that although active RF compensation does improve langmuir probe analysis considering only three harmonics does reduce accuracy. This was concluded after measuring the RF plasma potential directly using a capacitive probe. A much more accurate active RF compensation would be to include up to at least 6 harmonics although a further look into the electrical characteristics could allow improved power transfer to reduce the number of harmonics within the system.

The chapter has also shown the Mass Spectra of the RF plasma contained within the system. This allows us to ensure that there is a) active nitrogen species within the plasma (N^+, N_2^+) to interact with the carbon and b) that the levels of contaminate particles are within an acceptable range.

This chapter fill the void preventing the plasma from being operated as a 'black box' style system whereby the process taking place within are unknown. This will allow for much more accurate a detailed modification of nanotubes allowing modified nanotube properties to be directly linked to plasma properties, i.e. would allow selection of T_e (or any other plasma parameter) which would correspond to a specific set of CNT properties.

Chapter 5

Characterising Carbon Nanotubes

Once produced and after exposed to the RF plasma the CNTs must be charaterised in order to get an understanding of the CNT properties, and the changes that have taken place in their electronic structure. The methods for characterising the functionalised CNTs include; output charcteristics of CNT thin film transistors (TFTs), Fourier transform infrared spectroscopy (FTIR), X-Ray photoelectron spectroscopy (XPS) and Raman spectroscopy. CNTs created have been imaged however it is not expected that any changes will be able to be seen on the resolutions which can be achieved on TEM. High resolution images of the purified powder have shown that it contains carbon onions, multiwall, double and single walled nanotubes as well as nano horns, an example of the images of MWNTs produced during this study are shown. By creating CNT TFTs, from the functionalised CNTs properties such as conductance, gate dependance and mobility can be calculated; allowing correlation between plasma parameters such as ion energy, plasma potential, exposure time etc. FTIR, XPS and Raman have been implemented to observe the content and bonding in the CNTs.

5.1 Carbon Nanoparticle Images

The carbon nanotube bundle shown in figure 5.1 shows nanotubes created in liquid nitrogen at 90 A, this image shows nanotubes that have been used to create transistors. However it must be noted that the concentration, i.e. nanotube density over the substrate surface, is much higher in these pictures to aid imaging. The image was taken

with a Zeiss Supra 40 VP FEG Scanning Electron Microscope (SEM) microscope at Manchester Metropolitan University in The Dalton Research Institute DRIAM Analytical Service. The image shows a long bundle of nanotubes running from top to bottom and a wide bundle of nanotubes which are much more clear lay across the first from left to right. It can also be seen that the surface around the bundles contain nanotubes and this is more representative of what would be seen on a transistor substrate.

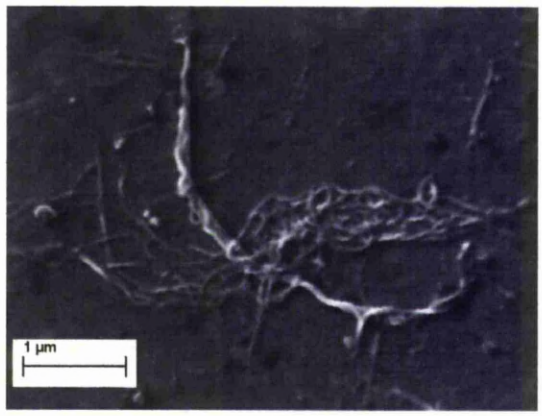

Figure 5.1: Bundle of nanotubes cast on a silicon substrate.

Nanotubes, Onions and other Nano structures were observed under TEM to ensure that the materials produced contained large amounts of high quality carbon nanoparticles. The images in figures 5.2 to 5.6 were taken using a FEI 120kV Tecnai G2 Spirit BioTWIN TEM in the Biomedical department at the University of Liverpool and shows in much more detail the various nanoparticle structures for different production conditions. The images are labelled showing 5 different types of carbon structures;

A	Larger carbon nanotubes, (10's of walls)
B	Featureless carbon structures
C	Smaller diameter carbon nanotubes tubes, (less than 10 walls)
D	Carbon web like structure
E	Carbon Onions

It should be noted that due to the magnification of the TEM it is impossible to distinguish between amorphous carbon and single graphene structures such as carbon nanohorns. Although it is difficult to analyse bulk properties of the produced materials

through TEM these images indicate the regimes at which different materials are created.

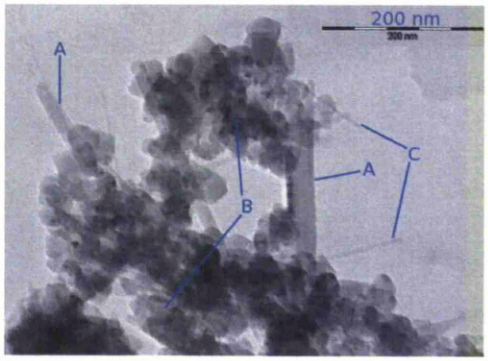

(a) 35 Amps

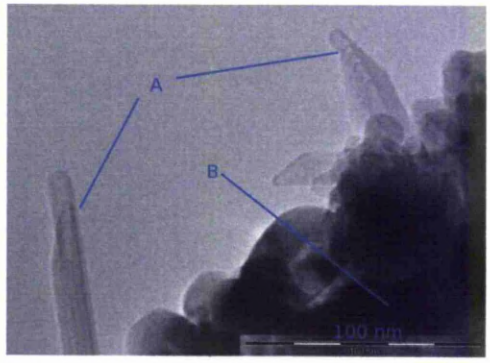

(b) 60 Amps

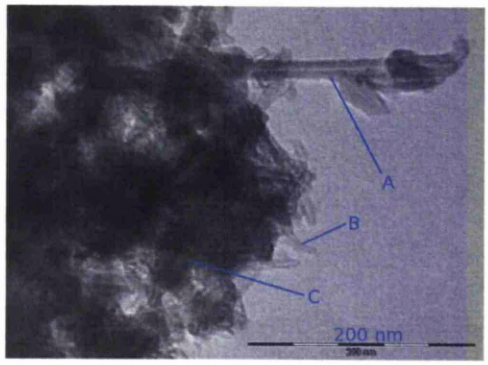

(c) 90 Amps

Figure 5.2: Ethanol/Water mix material produced under different conditions.

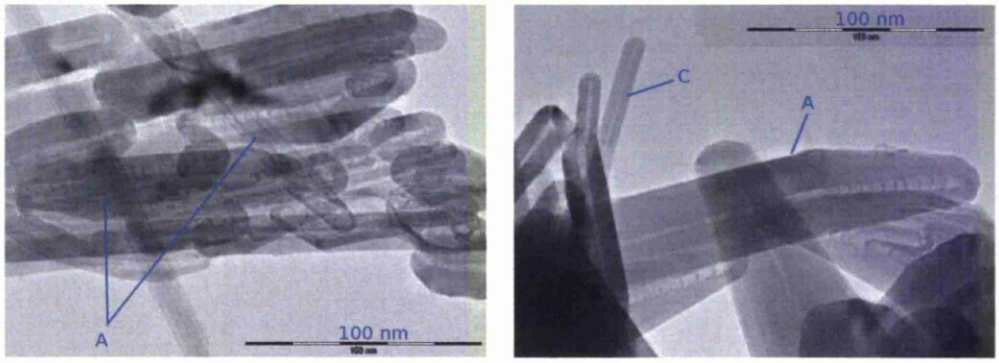

(a) Example 1 (b) Example 2

Figure 5.3: Liquid Nitrogen material produced at 90 Amps.

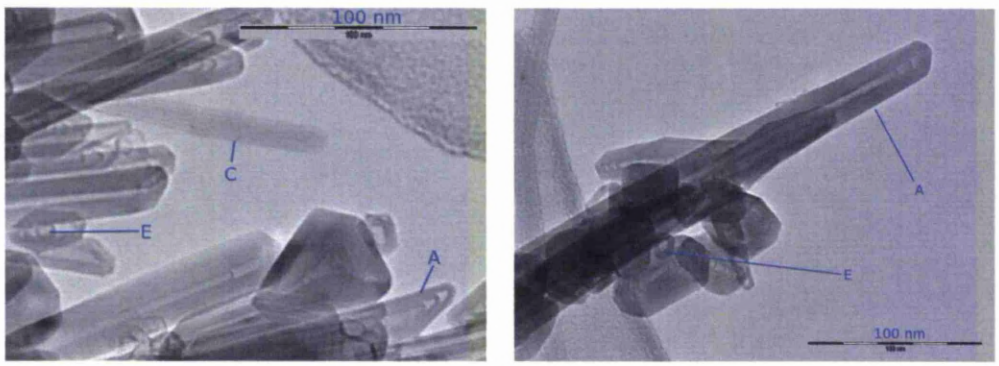

(a) Example 1 (b) Example 2

Figure 5.4: Liquid Nitrogen material produced at 35 Amps.

During the production process it was noted that condensation which formed around the protecting beaker (as shown in figure 2.22., chapter 3.4) contain a very fine black soot like powder, this material could also be found on the condensation of the inner pyrex beaker, it is here were samples of the material was taken. It was possible to allow the condensation to melt to water, which contained some carbon materials, however a much larger amount of material remained on the beaker after the condensation had melted. This was cleaned off using acetone and collected for imaging. Figures 5.5 and 5.6 show that this material does contain carbon nanotubes, suggesting that some CNTs are airborn during the production process. Although carbon nanotubes were present within the 'airborn' material they did not form a significant proportion, the majority of material was a web like structure which can be seen most clearly in figure 5.6(a). This material was unique to the Liquid Nitrogen production process and is most likely to be airborn due to it's thin structure and because of the volatile nature of the constantly boiling liquid. This material probably contains carbon nanohorn agglomerates about 20-30nm in size similar to those seen by N. Sano et al [63].

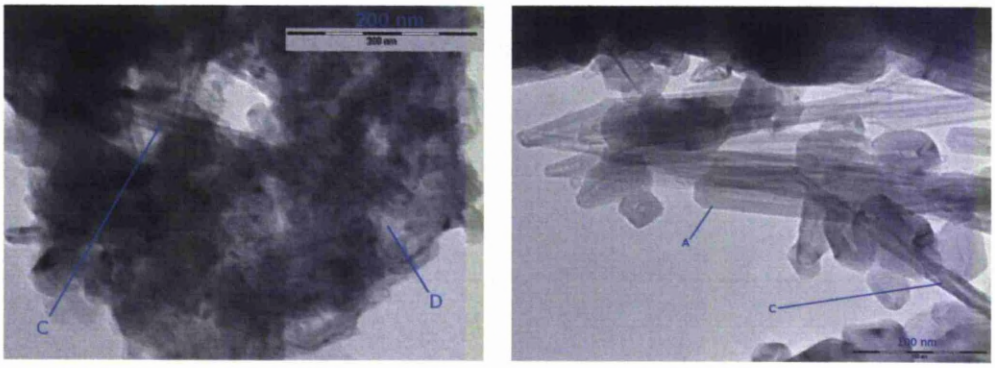

(a) Example 1 (b) Example 2

Figure 5.5: Liquid Nitrogen material from outside the beaker produced at 90 Amps.

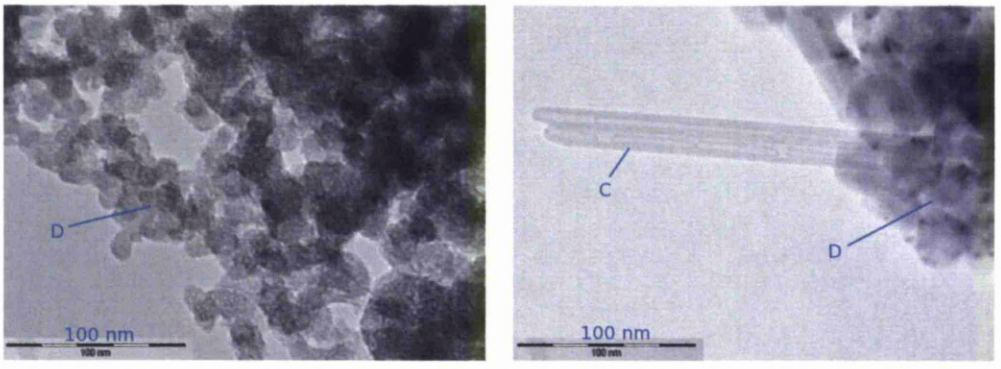

(a) Example 1

(b) Example 2

Figure 5.6: Liquid Nitrogen material from outside the beaker produced at 35 Amps.

5.2 Preparation of Carbon Nanotube Transistors

One of the main tools for characterising the functionalised CNTs has been the creation and study of CNT transistors. The method used to create the channel between source and drain is different than in traditional thin film transistors. A nanotube solution is drop cast on the sample and therefore nanotubes are distributed randomly on the channel to form a percolation network. In traditional field effect transistors (FET)s the carriers travel inside a continuous material, whereas in nanotube transistors the carriers travel through a percolation network. The charge transport and density of states within the percolation path across the channel is dependent upon the electronic properties of the individual CNTs an the contacts between them. However as CNTs appear in large bundles it is expected that variation between CNT transistors produced from the same CNT material will vary due to the density of CNTs cast over the surface.

MWNT transistors have been constructed on silicon substrate supplied from Si-Mat Silicon Wafers with a 200nm thermally grown oxide (SiO_2) layer on top. The substrate is n-doped with arsenic and in the [100] orientation. The gold source and drain contacts are evaporated on to the surface using a in-house built mask. Once contacts have been deposited CNTs are drop cast from the pre prepared dichlorobenze/CNT solution. Varying the concentration by weight of nanoparticles in the solution allows for controlling of the nanoparticle concentrations in the molecular devices. The sample is then left to evaporate leaving only CNTs on the substrate. Once created the devices have been characterised by recording the transfer and output characteristics to show current in the channel against voltage on the drain and voltage on the gate. After characterisation the devices were placed within the nitrogen RF plasma in order to be functionalised, these same devices were then characterised again and comparisons between the non-functionalised and functionalised samples are drawn.

5.2.1 CNT Transistor Design

A mask made of glass fibres and steel was constructed, slots were cut into the steel, to create the contacts and glass fibres were placed perpendicular over the slots to form the channels. The back surface of the n^+-Si substrate is carefully cleaned with HF to remove the native oxide layer and an aluminium layer is evaporated to serve as back

contact, figure 5.7.

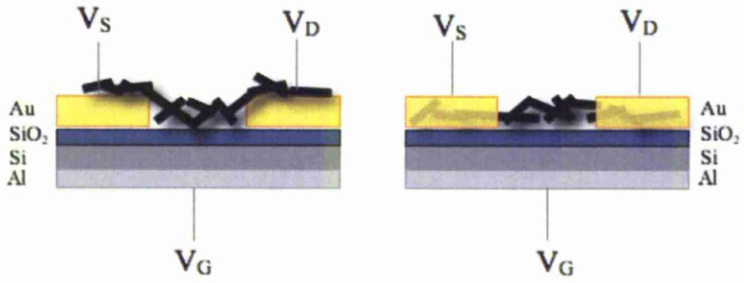

Figure 5.7: MWNT field effect transistor structure on the left is the final structure used for producing CNT transistors.

Figure 5.7 shows two different approaches used to create the CNT transistor structures, the first is a diagram of the final design whereby the nanotubes are deposited over the gold contacts, the second is an alternative design which was used in order to minimise the contact resistance between CNTs and the Au by increasing the contact area. In the latter approach the CNTs are deposited first and the Au contacts deposited afterwards, however this design was not after issues with the fabrication.

The channels defined in this process are long compared to those that can be achieved using a photolithography process as a result there is a need to use much larger concentrations of carbon nanotubes in the solution to obtain a percolation path between the source and drain, than was originally expected. The source/drain mask produced contact pads which were 1mm by 2mm meaning that the leakage current through the SiO_2 gate dielectric that was equivalent to that of the drain current was present. This was overcome simply by reducing the area of the contact pads to 0.1mm by 2mm. As seen in figure 5.8 the leakage is reduced and the gate current does not depend upon the drain voltage, showing that the drain to gate leakage current is minimised.

Large area deposition of nanotubes was also contributing to added leakage. When the material was cast across the whole testing substrate which contained 10's of transistors the nanotubes were becoming charged as the tested device was in use, this also produced small amounts of source-gate leakage. This leakage due to charging of nanoparticles can be lowered by cleaning around the device to isolate it from the rest of the sample, and thereby isolating each transistor from the collective. Figure 5.9 shows a

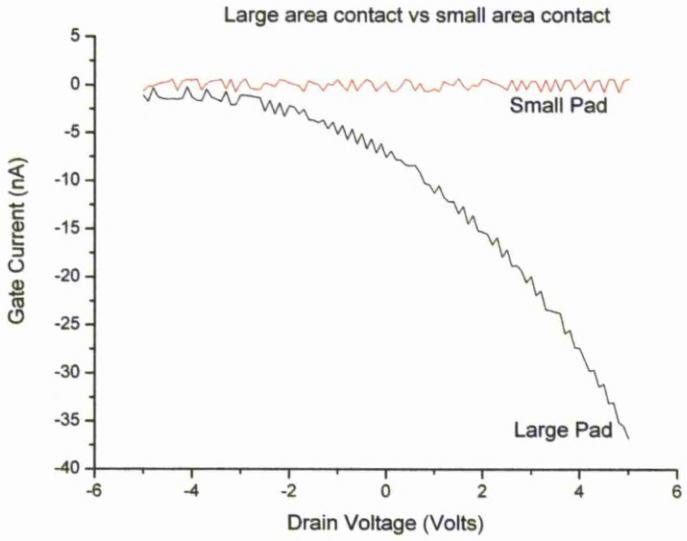

Figure 5.8: Leakage difference between large and small contact areas.

device under a microscope, the dotted area represents the area which is isolated before measurements take place, with the channel, source and drain sizes also being marked. The concentration of nanotubes on this sample has been exaggerated for illustrative purposes.

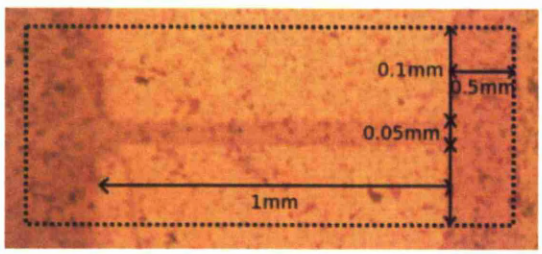

Figure 5.9: RN-MWNT TFT under microscope. Dotted area represents the area which is isolated before measurements take place.

The dispersion of the nanotubes before casting is vitally important to the creation of random network CNT transistors. If the CNTs are not dispersed correctly then the concentration could vary over the substrate giving CNT transistors which are expected to have the same characteristics different properties. This can be seen in figure 5.10 which shows variation of conduction of p-type SWNT-TFTs, cast from a solution of toluene, over the surface of the device, each device is separated by 3mm. Figure 5.11

shows an exaggerated example of poorly dispersed nanotubes over the surface of the substrate.

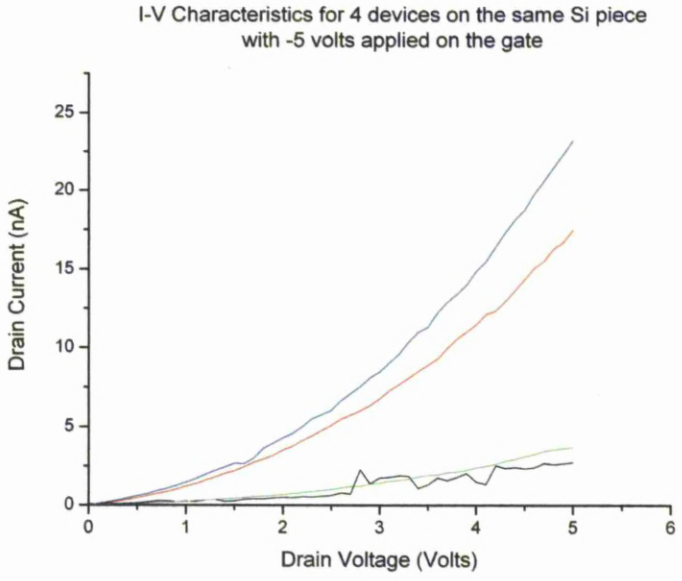

Figure 5.10: Example to show importance of dispersion over the Si area.

A number of different solvents have been tested in order to improve dispersion; acetone, toluene, xylene, chloroform and dichlorobenzene. Each solution is prepared in a small vial and placed in a small custom made stand, which has been designed to fit in the ultrasonic bath. Figure 5.12 shows the variation over time of the CNT dispersion in the solution for 1% of MWNTs by weight. The difference between xylene and chloroform is not shown here but no difference between the two was observed. As the dichlorobenzene proved to have the best carbon dispersion properties it was selected to be used to produce the nanotube transistors. By mixing the nanotubes by weight with the dichlorobenzene they be accurately drop cast over the surface of the substrate using a micro pipette. Having a long dispersion time was desirable as this meant that the nanotubes would not group or bundle whilst the solution is evaporating, this would leave an even distribution over the surface of the substrate.

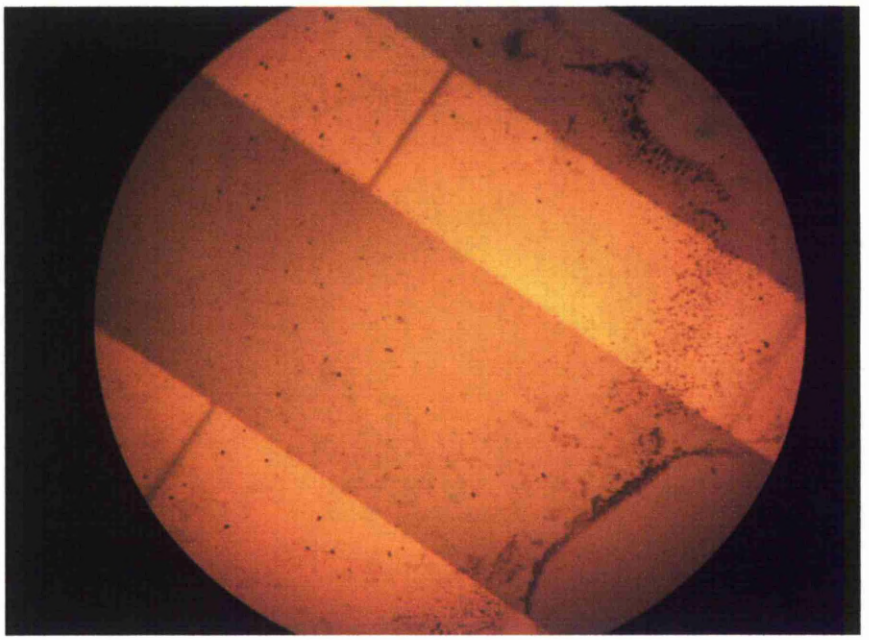

Figure 5.11: Image of poorly dispersed nanotubes over the surface of the substrate.

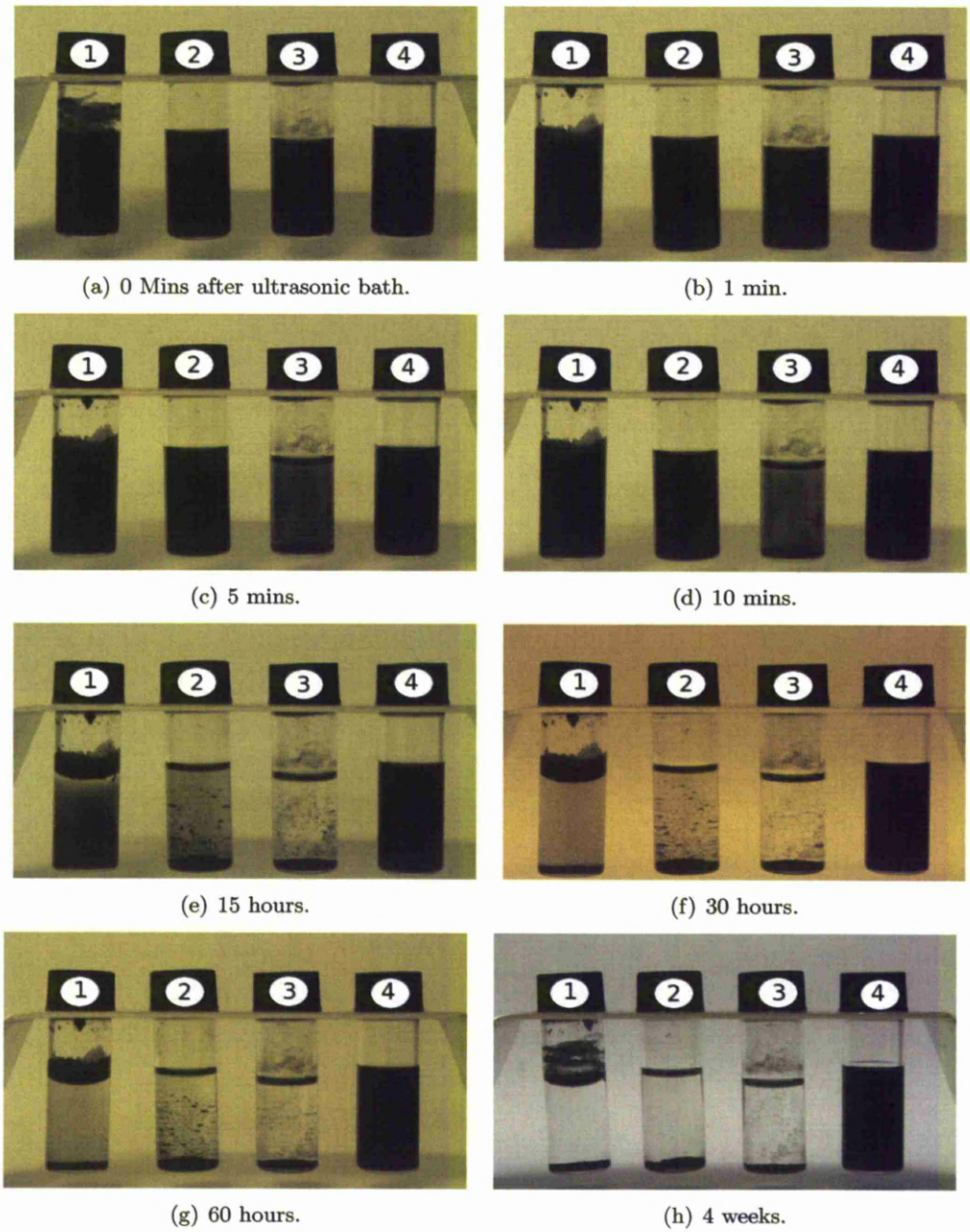

(a) 0 Mins after ultrasonic bath.

(b) 1 min.

(c) 5 mins.

(d) 10 mins.

(e) 15 hours.

(f) 30 hours.

(g) 60 hours.

(h) 4 weeks.

Figure 5.12: Various solvent comparison over time after 30mins ultrasonic bath. MWCNTs in 1) Toluene, 2) Xylene, 3) Acetone, 4) Dichlorobenzene.

The nanotubes would not disperse very well in acetone. Xylene and chloroform dispersion was good but only whilst being subjected to ultrasonic vibration, which resulted in the nanotubes regrouping whilst the solution was drying on the sample. Toluene and dichlorobenzene showed the best dispersion of nanotubes. In the former the nanotubes would re-combine after a few hours however in the latter the nanotubes would stay dispersed for weeks. Therefore dichlorobenzene has been selected to be used as the casting solvent, meaning that the nanotubes cannot recombine on the surface of the sample while the solution is drying. However it is not perfect and variation across the device can still occur. Another method to improve dispersion is simply by ensuring that the solution is in an ultra sonic bath for around 30 minutes. In order to improve consistency micro pipettes have been acquired which allow very accurate measurements. A high concentration of nanotubes in the solvent is produced from the carbon nanotube powders, around 1%, this is diluted to produce useable concentrations. Using this method it is possible to drop cast the exact same amount every single time ($300\mu l$), and because the surface area of the silicon sample is known the density of nanotubes on the surface can be easily calculated. A sample cast with this solution will have the appearance of a dark matt finish on the silicon sample.

Another method of improving nanotube distribution over the surface is to alter the surface properties of the substrate. Using an oxygen plasma treatment it was possible to change the wettability (contact angle) of the substrate from 25% to 5%. That is to say that with a decrease in contact angle the tendency of a drop to spread out over a flat increases. The advantage of this modification means that the dichlorobenzene on the surface dries more evenly as the lower wettability prevents the forming of droplets as the liquid evaporates, i.e. the dichlorobenzene is constantly spread over the entire surface of the substrate rather than drying to an increasingly smaller size drop.

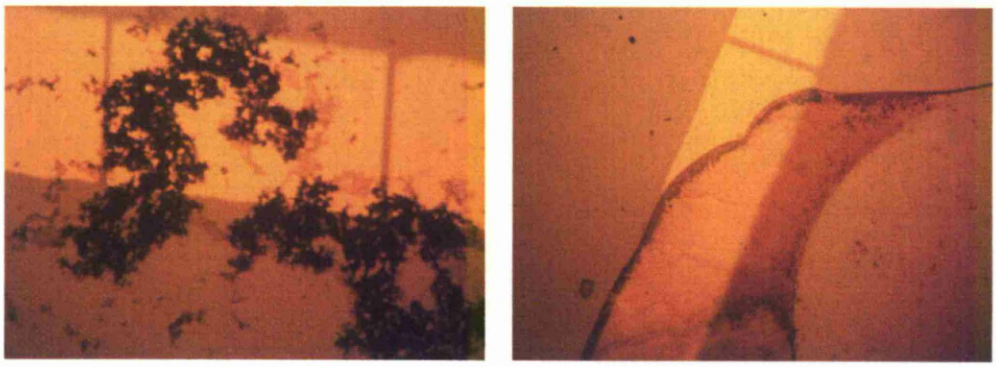

(a) Example 1 (b) Example 2

Figure 5.13: 25% contact angle.

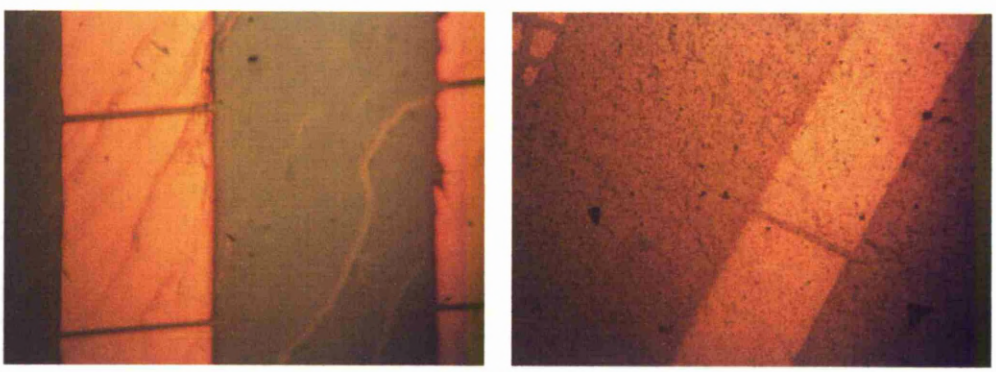

(a) Example 1 (b) Example 2

Figure 5.14: 5% contact angle.

Percolation Theory

When a nanotube solution is drop cast on the substrate the nanotubes within the solution form a percolation network across the channel. A percolation network is a collection of randomly distributed connections which lends it's self well to material science in relation to carbon nanotubes. Percolation theory describes the random nanotubes which are distributed over a two dimensional, [87], surface and the percolation paths, connections between each nanotube, that are formed [88, 89]. Frank et al [87] discuss the conductivity of randomly placed resistors in two dimensional lattices, this is not unlike the nanotube network which are created when drop casting solution over source and drain contacts. A critical component of the percolation theory is the percolation threshold, p_t, this is the point wherby a network will become electrically conducting,

$$G_{total} \approx G_n(p - p_t)^C \tag{5.1}$$

$$\tag{5.2}$$

where G_{total} is the network conductivity, G_n is the individual nanotube conductivity, p is the concentration, p_t is the threshold concentration and C is the conductivity exponent. This means that the network will become conductive once the percolation threshold has been reached. The exponent factor C as calculated by Frank et al [87] by using a large cell renormalisation group approach to be approx 1.3 for a two dimensional network. The percolation threshold is the mass of nanotubes per unit area on the device.

Percolation paths in the transistors form three types of paths, due to the semi-metal nature of the nanotubes created. The first is the semi-conducting paths, these paths are created entirely of semi-conducting nanotubes and form the longest channel lengths. The second is the metallic/semiconducting paths, these paths form channels with semi-conducting properties but do contain metallic nanotubes. Due to the metallic components in this type of path it forms the shortest channel lengths, this is expected to be the most common path. The last is the simple metallic paths whereby the paths are formed entirely of nanotubes with metallic behaviour. These paths are not desirable and can be removed by a process known as nanotube burn off.

5.2.2 Nanotube Burn Off

Devices have been created out of a number of different types of nanotubes. The first devices to be constructed were those which contained the H_2O and LN_2 MWNTs created in the lab, chapter 3. The other types of CNTs which have been tested are MWNT from Manchester University which have been functionalised with chemicals to help improve dispersion, pure MWNTs from Patras in Greece and some SWNTs from Manchester University have also been tested. Details of the construction of these devices can be found in chapter 2.

If a device shows some gate voltage dependence, i.e. contains some semi-metalic CNTs, it can be possible to increase this dependence by removing any purely metallic paths through the channel. In order to do this any semi-conducting nanotubes must be turned off, this is achieved by applying a high positive gate voltage for p-type, (a high negative voltage is required for n-type) for a long period of time. During this period a large source - drain current is passed then when this current starts to drop some of the metallic nanotubes will have been damaged and therefore no longer conduct. This is known as metallic 'burn off' and increases gate dependance. Percolation paths containing semi-conducting CNTs will not be passing current during the burn off procedure as they will be turned off due to large gate voltage. This means that only paths which contain just metallic CNTs will be destroyed. Figure 5.15, shows IV characteristics for both before and after this burn off procedure has taken place.

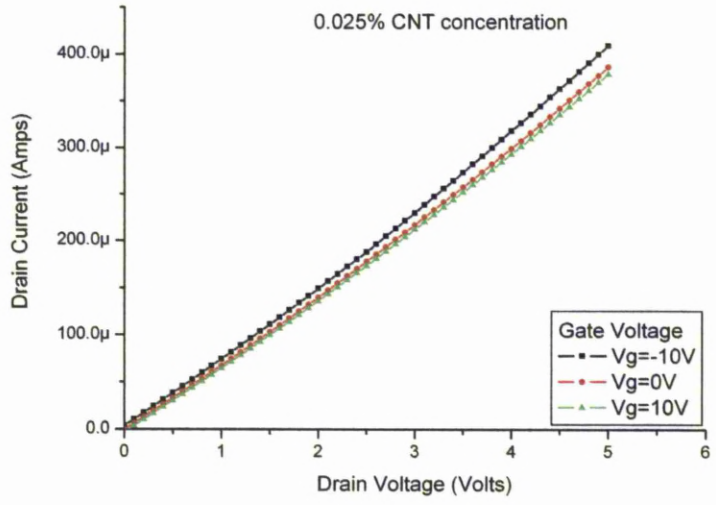

(a) IV characteristics before burn off.

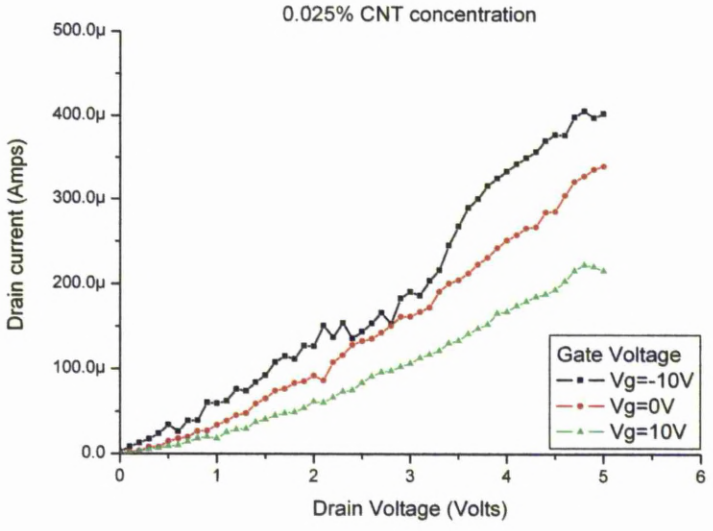

(b) IV characteristics after burn off.

Figure 5.15: Difference before and after burn off of LN_2 MWNTs, via high current passed through the metallic paths whilst semi-conducting paths are turned off.

Nanotube Transistor Operation

In traditional FETs the carriers travel inside a continuous material, whereas in nanotube transistors the carriers travel through a percolation network. Every nanotube of the network is expected to have different density of states. At the contact, the potential barrier and contact resistance limit the overall carrier mobility and affect the measured current. As the density of the tubes increases, a continuous path between the two electrodes is formed. As mentioned earlier there is a critical density for which the first complete path between the electrodes forms. Due to the nature of the nanotubes created it is possible to have the paths containing both semi conducting nanotubes and metallic nanotubes. This means that the contact between the nanotubes and both the source and drain electrodes could be constructed from semiconducting nanotubes, giving rise to a Schottky barrier.

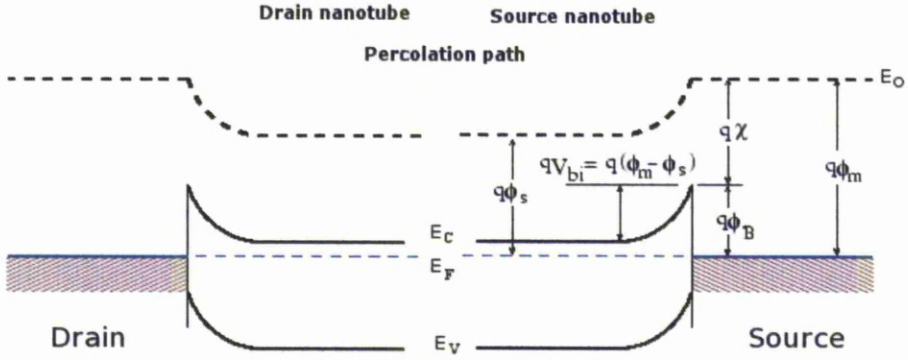

Figure 5.16: Band diagram example and labelling of back to back schottky barrier transistor.

Were E_c is the conduction band, E_F is the Fermi level, E_0 is the energy at the top of the barrier and E_V is the valence band. It can be said that schottky barriers are formed between nanotubes and the Au electrodes due to the nature of the metal/semiconductor contact, assuming the first and last nanotubes in the percolation path to be n-type semiconductors (i.e. those which connect the percolation path to the electrodes). An n-type semiconductor is consider in this example, as n-type conduction in MWNTs is created with the injection of carriers, in this case electrons from the nitrogen modification. However it is also noted that the contacts between the nanotubes

is expected to be ohmic, or at least a schottky barrier with a very thin depletion layer, and as such a schottky analysis of nanotube transistors only applies to channel paths where semiconducting nanotubes at the start of a path are in contact with the source or drain contacts. A Schottky barrier is created when a difference in work function produces a large barrier height, defined as; $q\phi_B >> kT$. Au is used as the electrodes, giving a metal work function, $q\phi_m$, of 5.3eV, and assuming the nanotube is a n-type semiconductor with a work function, $q\phi_s$, of 4.5eV this gives a barrier height, $q\phi_B$, of 0.8eV. Satisfying the Schottky definition of $q\phi_B >> kT$ (where kT is 4.14×10^{-21} at 300K). This therefore means that the nanotube transistors created consists of two back to back Schottky barriers with a percolation path between them. The barrier at the source can be treated separately to that at the drain because the long channel length means that the field at one will not effect the other.

The Schottky barrier theory of operation requires that the conditions at source and drain are such that carriers injected at the source can exit at the drain.

To begin with, the case where V_g is fixed at zero will be examined. When the drain voltage is positive the barrier height decreases, figure 5.17 top, and the electric field is from the metal to the semiconductor allowing electrons to move easily from the semiconducting nanotube to the Au, this is known as forward bias. At the source the local field is very weak since $V_g = V_s = 0$ although there is weak influence due to positive V_d. The current through the device is therefore limited as the barrier at the source does not change because V_s is grounded and therefore is (approximately) equal to the gate voltage. So in this situation the drain Schottky is forward bias and the source Schottky is still zero biased. Applying a negative voltage to the drain will result in drain Schottky contact becoming reverse biased and therefore only leakage current, due to tunnelling through the Schottky, will flow through the device. In this case the biggest limiting factor in current flow is the reverse Schottky at the drain as the source contact barrier has not changed. This case results in no current flow due to the drain Schottky being reversed bias, figure 5.16 bottom, and the source Schottky is again zero biased. Therefore a very small current will flow when V_d is negitive due to tunnelling though the Schottky barrier at the source. No current will flow in the desired direction (V_s to V_d) when V_d is negative, although a small current may flow due to tunnelling

though V_d which will have been aided by the lowering of the conduction band below the Fermi level. However this is limited by V_s being zero biased.

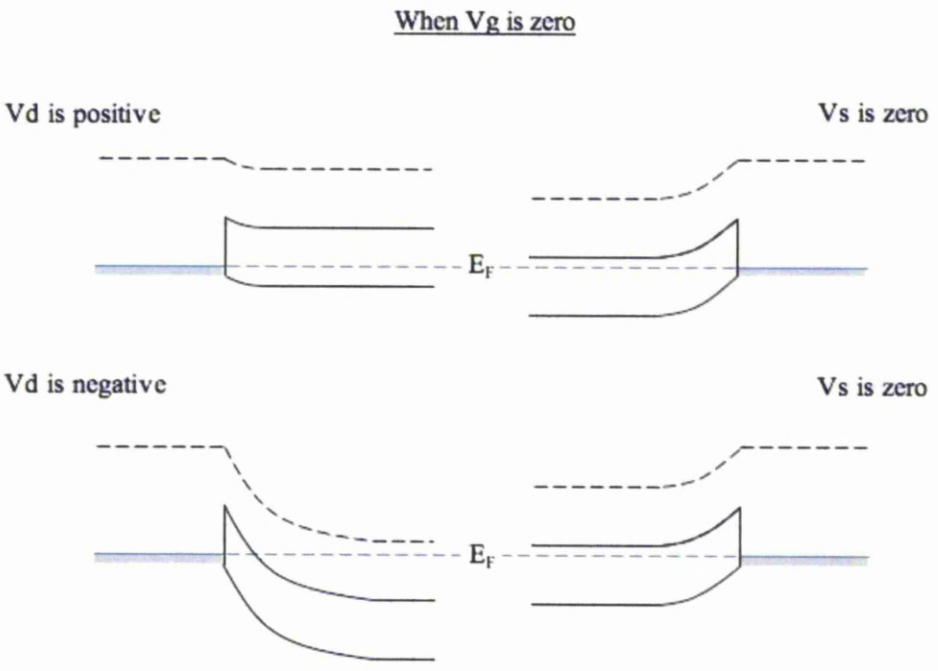

Figure 5.17: Gate voltage is zero, top) positive drain, bottom) negative drain.

When V_g is negative, figure 5.18, a positive voltage is applied to the semiconductor, applying a positive voltage on the drain which is greater than the voltage on the semiconductor (i.e. V_g) will result in an electric field from the metal to the semiconductor, therefore electrons in the n-type nanotube may acquire enough energy to overcome barrier, creating a forward bias Schottky barrier at the drain. The source however is still grounded, thus applying a negative V_g will result in the electric field from the semiconductor to the metal and therefore creating a reversed bias Schottky barrier. When V_d is less than V_g then the Schottky barrier at the source is reversed bias, as is the source barrier. The final situation for V_g is positive is when V_d is equal to V_d. The source barrier is now zero biased and the source Schottky barrier is still reversed biased.

In molecular devices it is generally assumed that the Fermi level is pinned to the

electrode Fermi level. This pinning of the Fermi level means that when a negative voltage is applied to the gate, when V_d is bigger than V_g, the surface of the nanotube is overpopulated with electrons (accumulation). The conduction band of the nanotube, at the source electrode, bends downwards to come progressively closer to the Fermi level. At certain value of V_g, the conduction band bends below the Fermi level from some distance x from the contact. The strong accumulation of electrons means that electrons can tunnel through the junction for positive V_d. As Vg decreases (i.e. an increasing negative voltage), x decreases leading to a sharp increase in current. The device is now forward bias at the drain and reversed bias at the source, however due to the pinning of the Fermi level the main conduction method is via tunnelling through the Schottky. This configuration of forward biased at Vd and reversed biased at Vs should be the optimum situation for passing current though the device.

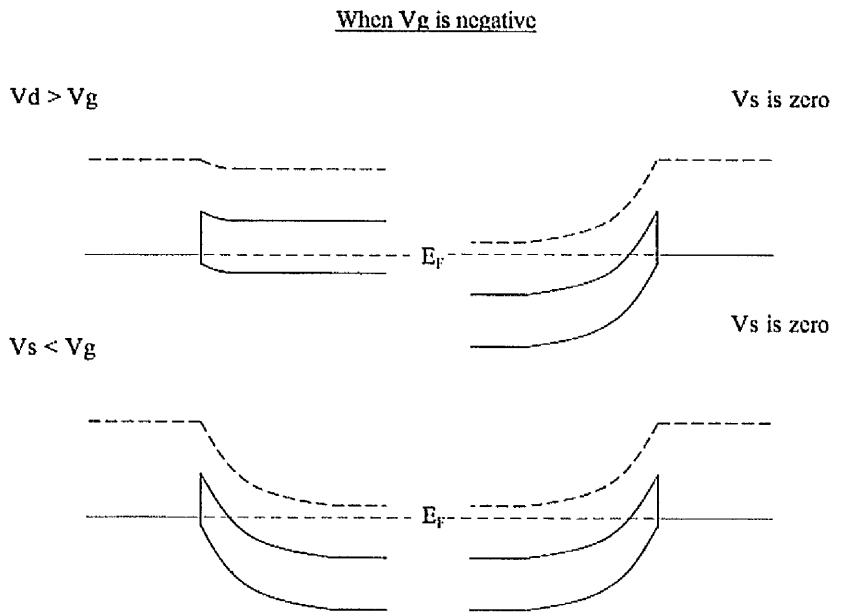

Figure 5.18: Gate voltage is negative, top) positive drain, bottom) negative drain.

The situation on the drain is not much different when the voltage on the gate is negative. The Schottky barrier at the drain is still forward bias when V_d is greater than

V_g. The source however is now forward bias as well due to the electric field, which is now from the metal to the semiconductor. This means that electrons will want to flow out of the device at both the source and the drain, (more so at the drain depending on how much greater V_d is than V_g) as there is no fourth contact as used in other FETs no current will flow. When the drain voltage is lower than the gate voltage the then the Schottky barrier at the drain is reversed biased, the source barrier is still forward bias. As before the Schottky barrier at the drain is zero biased when V_d and V_g are equal and because the source is grounded the barrier here is still forward biased. This will result in a current flow which is similar to the situation when $V_g = 0$ and V_d is negative. A leakage though the device will flow via tunnelling though the barrier at the drain this is made easier by electrons escaping though the forward biased source schottky.

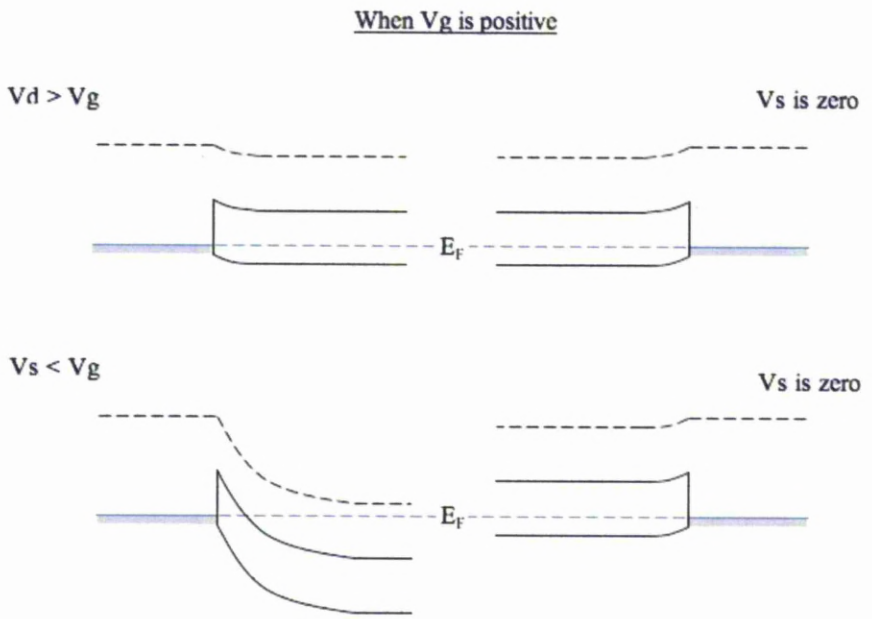

Figure 5.19: Gate voltage is positive, top) positive drain, bottom) negative drain.

The channel current is controlled via the tunnelling of carriers at the junction of the source/drain with the nanotubes.

In summary:

When $V_g = 0$ and $V_d > 0$ then drain is Forward Bias and source Zero Bias. When $V_g = 0$ and $V_d < 0$ then drain is Reversed Bias and source Zero Bias.

When $V_g > 0$ and $V_d > 0 > V_g$ then drain is Forward Bias and source Reversed Bias. When $V_g > 0$ and $V_d < 0 < V_g$ then drain is Reversed Bias and source Reversed Bias.

When $V_g < 0$ and $V_d > 0 > V_g$ then drain is Forward Bias and source Forward Bias. When $V_g < 0$ and $V_d < 0 > V_g$ then drain is Reversed Bias and source Forward Bias.

5.3 Plasma Treatment of CNTs

CNT FETs were fabricated as described earlier however the effects of exposing the silicon substrate to the plasma must be first understood. To test the effect of plasma exposure a silicon substrate with a thermally grown oxide the gate contact was prepared using the same process described earlier, and 1mm gold dots were evaporated onto the surface of the SiO_2. Once fabricated oxide capacitance (between the source and the gate) was measured. More gold dots were then evaporated onto the areas of the SiO_2 which had been exposed to the plasma i.e. areas which were not covered by the first set of gold dots. This test should be repeated for some longer exposure times for completeness. Figure 5.20 shows that there is a small but clear increase in the capacitance. The capacitance of a parallel plate capacitor of plate area A separated by a distance d is given in equation 5.3 (were ϵ_r the dielectric constant of the SiO_2 layer). Therefore as the area and dielectric constant remain unchanged the distance between the source and drain must drop in order to maintain the relationship. This implies that the SiO_2 is being sputtered by the RF plasma and will therefore affect the capacitance in the channel between the nanotubes and the gate, but will not have any effect to the SiO_2 which is protected by the Au contacts.

$$C = \epsilon_r \frac{A}{d} \epsilon_0 \tag{5.3}$$

Another effect on the device due to plasma exposure (and sputtering) was an increase in leakage current from the source to the gate, 5.21. As expected leakage through the device increases with drain voltage up to approximately ±10nA for unexposed devices and up approximately ±25nA, for devices exposed to RF plasma. However this

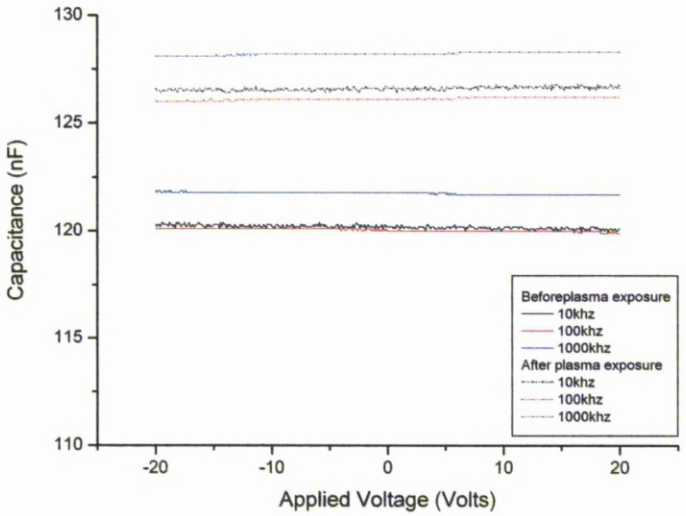

Figure 5.20: Effects of exposing the SiO_2 to the plasma. Capacitance of 1mm dots before and after 5mins of plasma exposure (6cm, 10 Watts, 10 mTorr)

leakage does not increase with plasma exposure time as can be seen in figure 5.21(c) where the leakage is approximately the same for 5, 10 and 15 mins plasma exposure for -5V on the gate.

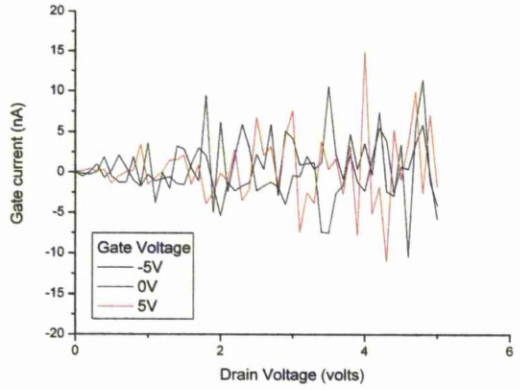

(a) Leakage through the device before 5 mins plasma exposure at 10mTorr 10 Watts and 6cm.

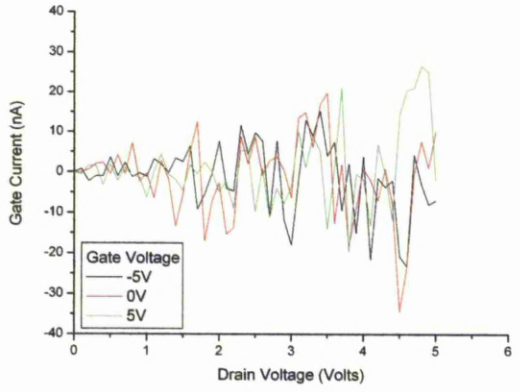

(b) Leakage through the device after 5 mins of plasma exposure at 10mTorr 10 Watts and 6cm.

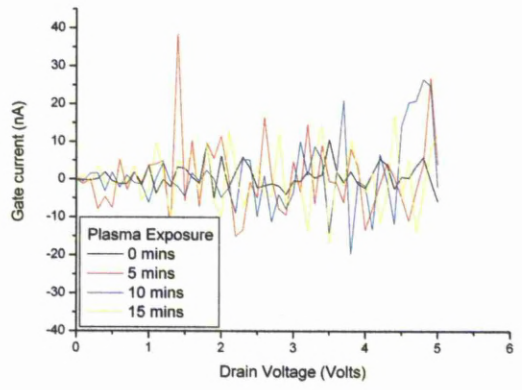

(c) Leakage through the device for variation in plasma exposure time at 10mTorr 10 Watts and 6cm.

Figure 5.21: Leakage current before and after plasma exposure.

5.3.1 Multi Wall Carbon Nanotube Transistor Analysis

A 350uL dichlorobenzene solution containing 0.0016% w.t. of MWNTs was cast onto the surface of prefabricated source and drain contacts (as described earlier). The MWNTs used here were formed by thermal CVD process and were supplied by the University of Patra, Greece. Before drop casting, the MWNT solution was stirred in an ultra sonic bath for twenty minutes to ensure uniform dispersion. MWNTs used here are expected to contain catalyst particles at the inside of their tip and because the diameter of the outside shell is more than 20nm, the nanotubes are expected to be semi-metallic. The resulting three terminal devices had a channel width of 1mm and length of about 200μm. The electrode area was 0.1mm^2. The total surface area of the Si chip used was 225mm^2, resulting in a MWNT concentration of 2.07 x 10^{-8} g/mm^2 over the SiO2 surface. The cast devices were left in air overnight to dry then stored in a vacuum vessel for another day before measurements were carried out. Following the recording of FET characteristics, the samples were treated in N^2 plasma. The plasma conditions were: N_2, pressure 10mT, plasma power 10W and exposure time 5mins. The FET characteristics were recorded immediately after plasma exposure and the samples were stored in vacuum. Another two plasma treatments of 5 minutes each followed, with the FET characteristics recorded after each exposure. The cumulative plasma exposure time was therefore 15 minutes. The FET characteristics were recorded again after the devices had been stored for 1 week in vacuum. This was done in order to investigate the effect of possible desorption of loosely bonded nitrogen species from the nanotube surface.

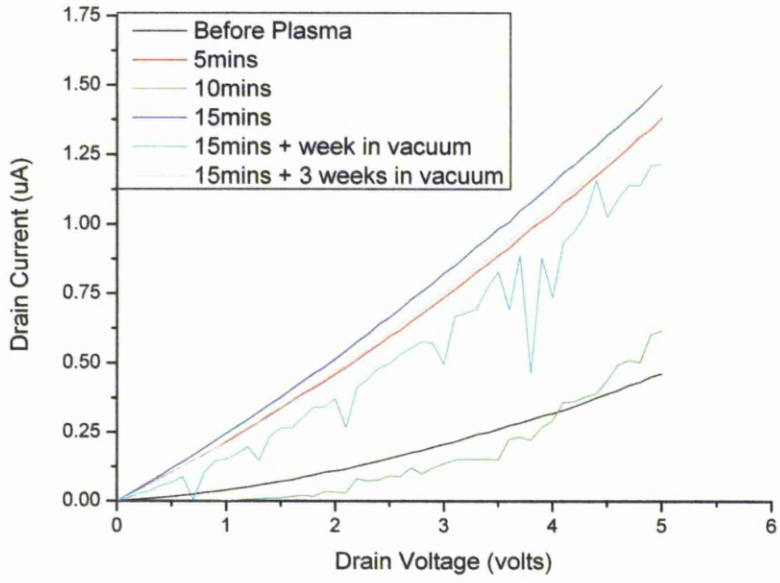

(a) Variation in conductivity, device N°93, (plasma exposure 10mTorr 10Watt 6cm)

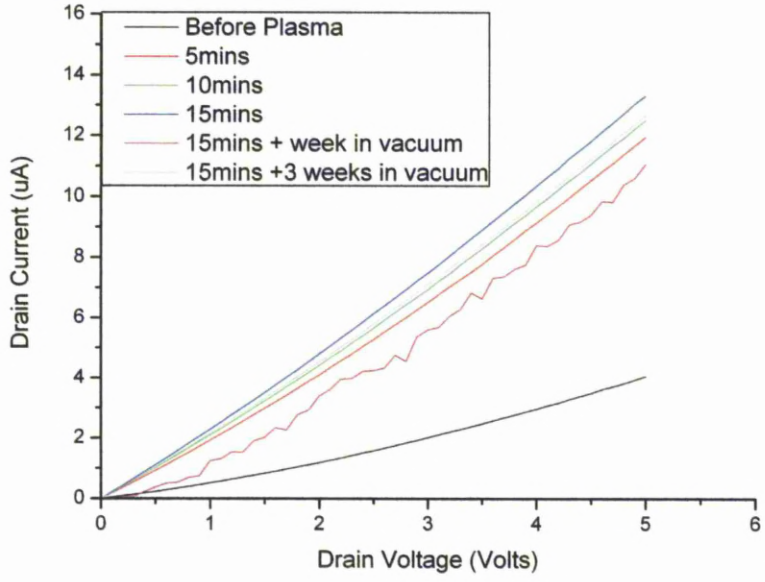

(b) Variation in conductivity, device N°41, (plasma exposure 10mTorr 10Watt 6cm)

Figure 5.22: Variation in conduction with exposure time for two MWNTFETs.

Figure 5.22(a) and figure 5.22(b) show the I_D against V_D curves, for a gate voltage of +5 volts, for two devices on the same substrate as a function of plasma exposure time. Both figures show that channel conductance increases progressively with exposure to plasma. The drain current at $V_D = 5V$ for device N°83, figure 5.22(a), increases from $0.4\mu A$ (as grown device, black curve) to $1.5\mu A$ (after 15min. cumulative plasma exposure). Device 41 displays a similar trend: after 15 minutes of exposure to plasma the drain current increases from $4\mu A$ to $13\mu A$. This equates to a percentage increase of 375% and 325% for device 83 and 41, respectively. When both samples were stored for 1 week in vacuum (1 mbar), drain current dropped. Device N°83 shows a drop of $0.3\mu A$ and device 41 drops $2\mu A$, 20% and 15% respectively. This result suggests that weakly bonded Nitrogen might have desorbed from the MWNT surface. However, the output characteristics show that 1 week after the last plasma exposure there is still clear enhancement of MWNT conductivity.

The inclusion of nitrogen to the carbon lattice was expected to alter the density of states and therefore increase the gate dependence of the devices produced. However this does not appear to be the case.

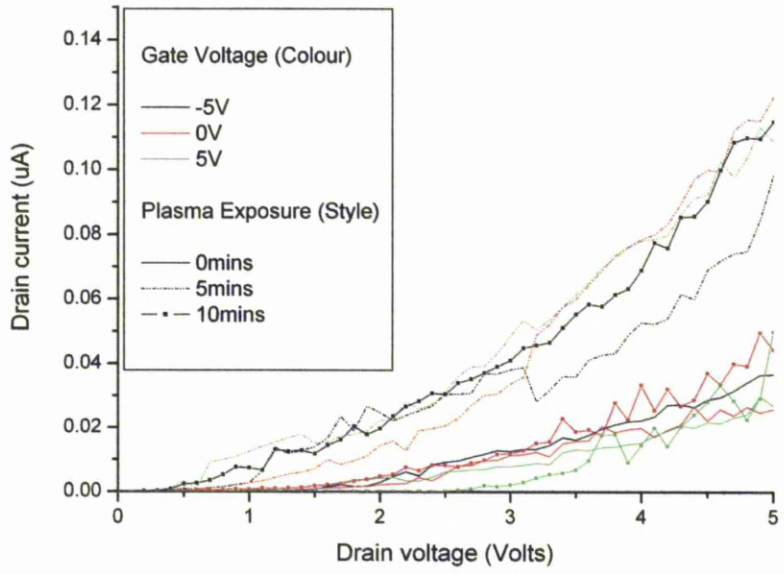

(a) Output characteristics for device N°84, this device shows a large change in gate dependence after plasma exposure (10mTorr 10Watt 6cm).

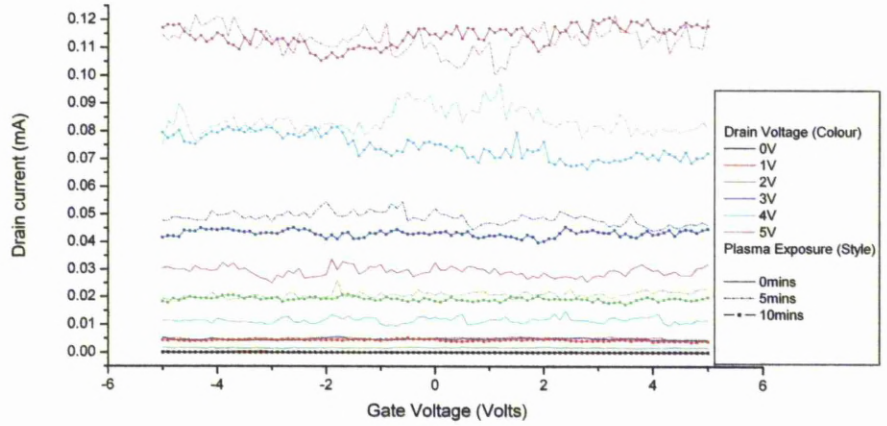

(b) Transfer characteristics for device N°84

Figure 5.23: Input and transfer characteristics for various plasma exposure times, device N°84

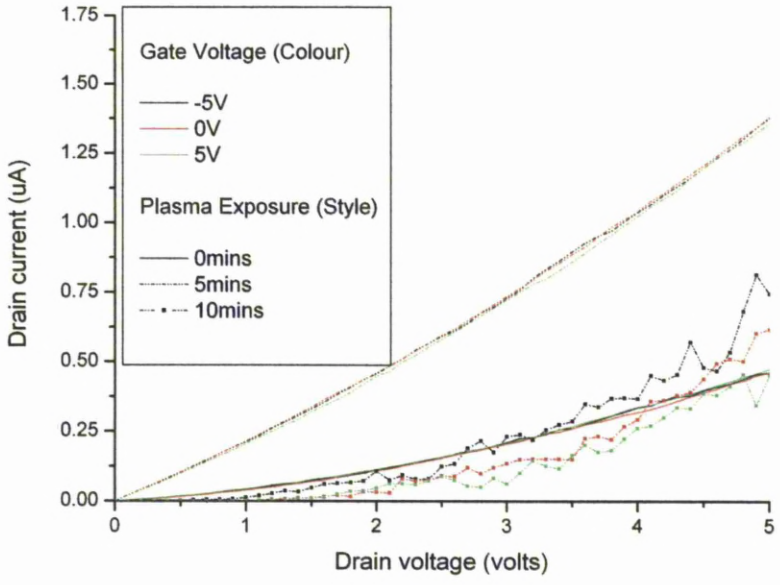

(a) Input characteristics for device N°93, (plasma exposure 10mTorr 10Watt 6cm)

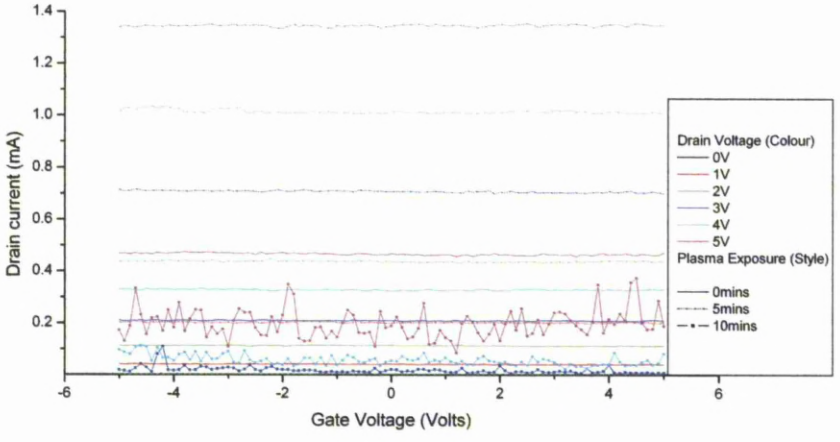

(b) Input characteristics for device N°93, (plasma exposure 10mTorr 10Watt 6cm)

Figure 5.24: Input and transfer characteristics for various plasma exposure times, device N°93

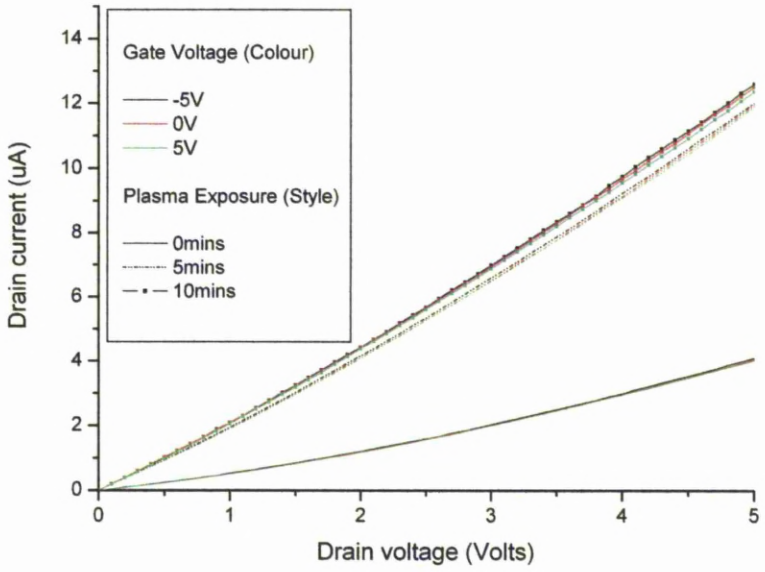

(a) Input characteristics for device N°41, (plasma exposure 10mTorr 10Watt 6cm)

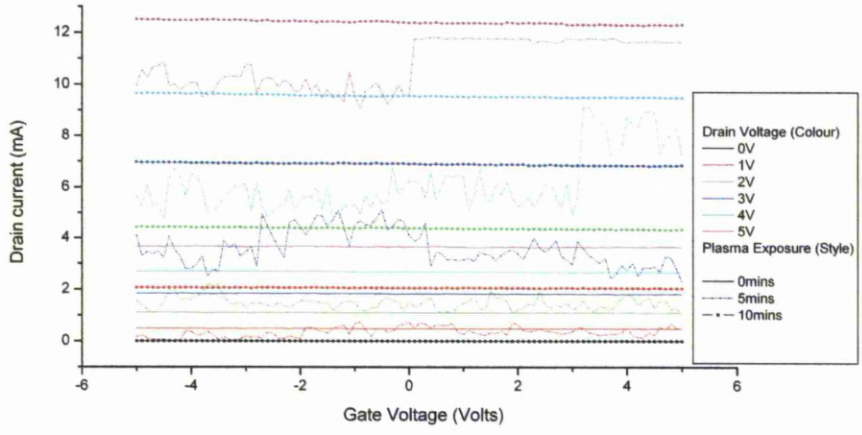

(b) Input characteristics for device N°41, (plasma exposure 10mTorr 10Watt 6cm)

Figure 5.25: Input and transfer characteristics for various plasma exposure times, device N°41

Figures 5.23, 5.24 and 5.25 show the dependence of the channel current on gate voltage. Devices N°s 84 and 93 (figures 5.23 5.24) show some variation with change of gate voltage whereas device N°41 (figure 5.25) does not, showing only increase in conduction. Those devices that show gate dependence display n-type field effect characteristics, i.e. when a positive voltage is applied on the gate the current increases and applying a negative voltage decreases.

5.3.2 Single Wall Nanotube Transistor Analysis

SWNTs were also exposed to a nitrogen RF plasma. A 350uL toluene solution containing 0.0016% of HiPco SWNTs was cast onto the surface of prefabricated contacts using the glass fibre mask production method. The total surface area of the Si used to create the devices was 225mm^2, therefore a concentration of 2.07×10^{-8}g/mm^2 (of SWNTs) is cast on the surface of the sample. As before the solution was stirred in an ultra sonic bath for ten minutes before casting. The cast devices were left in air overnight to dry then stored in a vacuum vessel for another day before measurements were carried out.

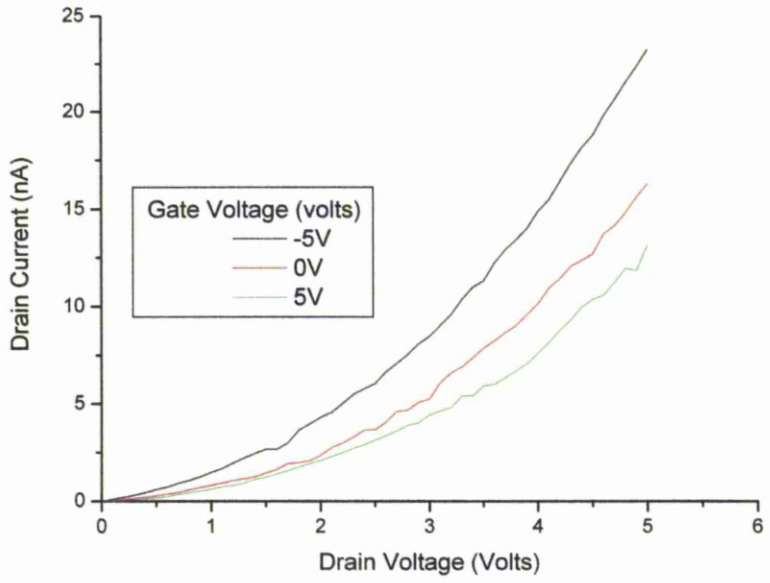

(a) IV characteristics for SWNT FET

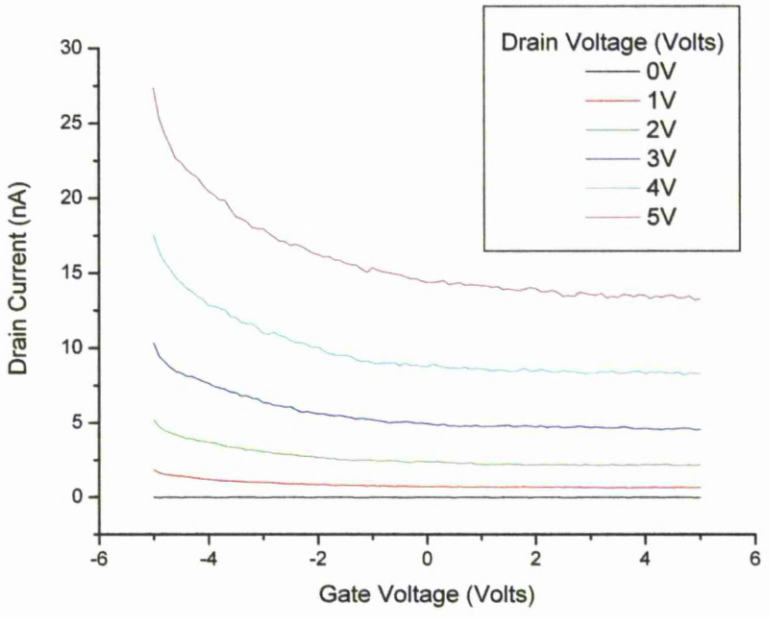

(b) Transfer characteristics for SWNT FET

Figure 5.26: IV and transfer characteristics for SWNT before plasma exposure

Figure 5.26, shows I-V characteristics for the HiPco SWNT FET for various gate voltages. As expected the SWNTs exhibit p-type behaviour with the current dropping from 23nA to 13nA, for V_D =5, when the gate voltage increases from -5 to +5 volts. The device does not switch off which suggests that metallic paths do exist along the channel, and that the SWNTs are semi-metals. Figure 5.27 shows a device with a much greater gate dependance, as the current is much lower in this device it is likely that the ratio of semi-metalic nanotubes to metallic nanotubes is higher even though the over all content of nanotubes is lower.

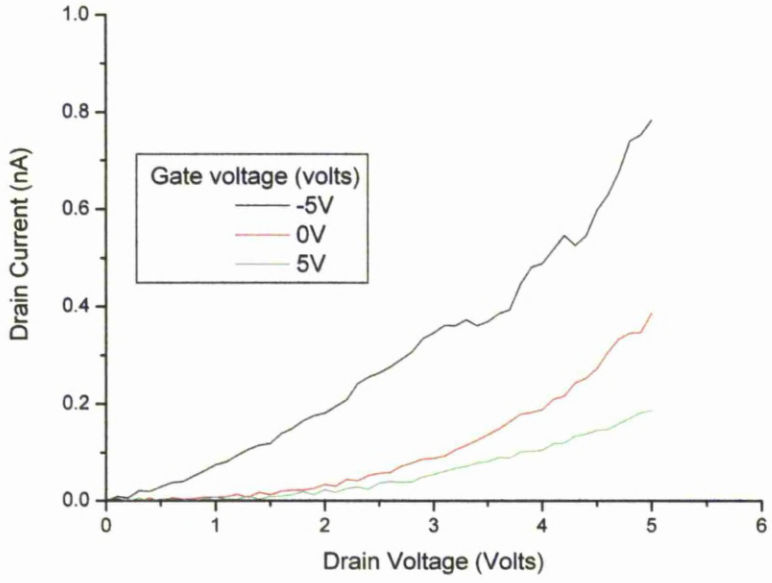

(a) IV characteristics for SWNT FET

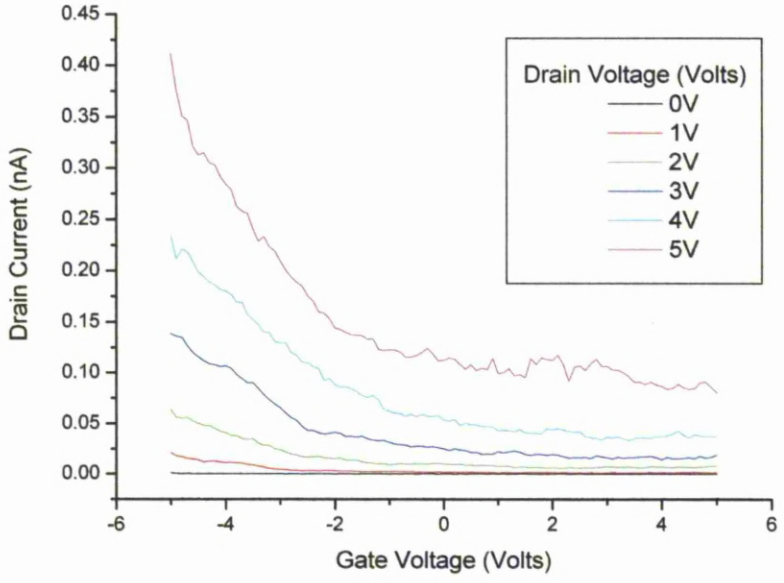

(b) Transfer characteristics for SWNT FET

Figure 5.27: IV and transfer characteristics for SWNT before plasma exposure

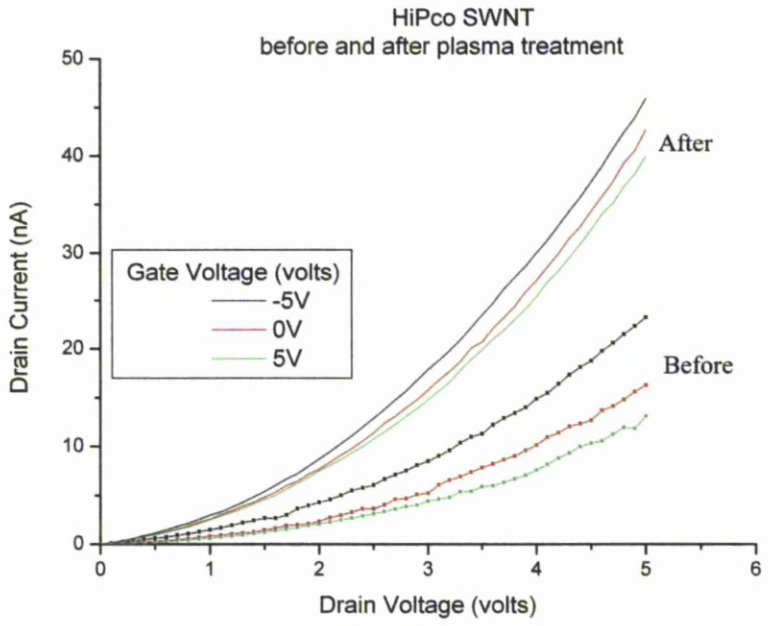

(a) IV characteristics after 10mins exposure

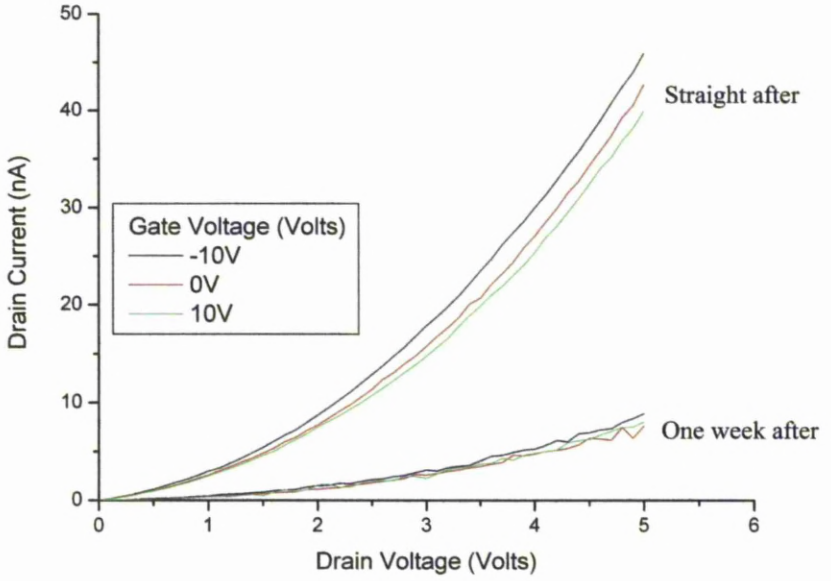

(b) IV characteristics one week after 10mins exposure

Figure 5.28: IV and transfer characteristics for SWNT FET

Exposing the SWNTs to 10mins of plasma has the effect of increasing conduction through the channel by 187%, figure 5.28(a), however unlike the MWNTs this conduction modification is not permanent, figure 5.28(b) shows that one week after exposure the device is no has lower conduction than before exposure. Loosely bonded nitrogen could have be desorbed from the SWNT resulting in damaged SWNTs which do not show the same conductivity.

Conventional transistors have two main regions in the transfer characteristics, figure 5.29, the linear region (below pinch off) and the saturation region (or above pinch off region). Pinch off is the point were the drain current, I_{DS}, in the device starts to saturate. As the CNT devices created do not saturate (due to the metallic components

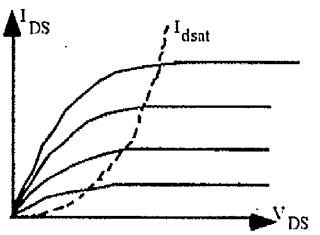

Figure 5.29: Typical transfer characteristics for n-type MOSFET

in the channel), analysis will concentrate on the linear region. In the linear region the drain current can be described by

$$I_D = \beta[(V_{GS} - V_T)V_{DS} - \frac{V_{DS}^2}{2}] \tag{5.4}$$

where β is the device constant given by

$$\beta = \frac{\mu C_o W}{L} \tag{5.5}$$

where μ is the mobility of the carriers, W is the width of the channel, L is the channel length, C_o is the gate capacitance. The transconductance, g_m, can be defined as

$$g_m = \frac{\partial I_D}{\partial V_{GS}} = \beta V_{DS} \tag{5.6}$$

and similarly the channel conductance, g_D, is given by

$$g_D = \frac{\partial I_D}{\partial V_{DS}} = \beta(V_G - V_T) \tag{5.7}$$

where V_T is the threshold voltage required to turn the device on, in the case of the CNT devices here this is zero. This can be re-arranged to define the mobility of the carriers

$$\mu = \frac{g_D}{C_o \frac{W}{L}(V_G - V_T)} \tag{5.8}$$

Using this MOSFET analysis it is possible to obtain the mobility of the carriers in the CNT-FETs created for this study, this can then be graphed against plasma exposure time and in the future other plasma parameters such as power, ion density, ion energy etc. For device N°93 , figure 5.22(a) and device N°41, figure 5.22(b) $\beta = 6.1 \times 10^{-}6$ from this the mobility can be calculated for the various plasma exposure times, figure 5.31 It can be seen that for device N°41, figure 5.30(b), there is a large increase in mobility as exposure time increases from 0 to 5mins but a slower rate of increase is seen from 5 to 15mins. However for device N°93, figure 5.30(a), there is a general increase but a dip at 10mins exposure time, this could be due to error in measurement of the IV curve. For device 93 the mobility does not decrease a lot over the weeks after exposure, figure 5.31(a) and device 41 shows a larger decrease but does not return to the value seen before exposure, figure 5.31(a).

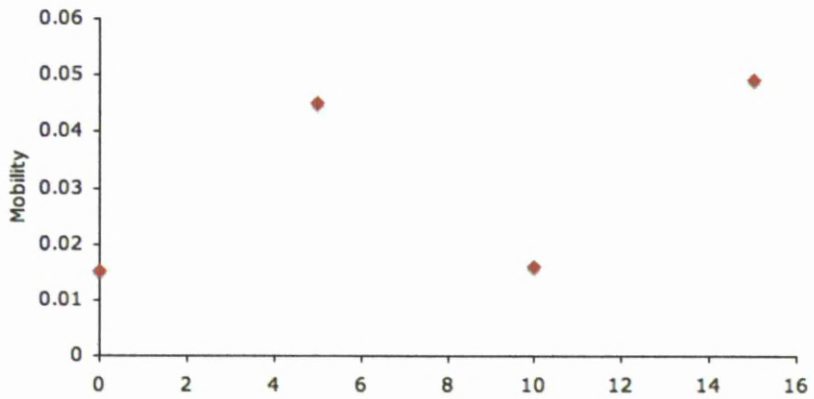

(a) Mobility for device N°93

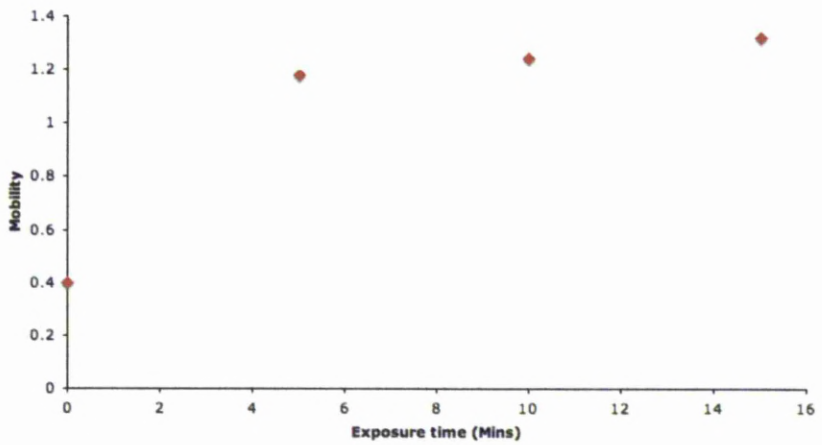

(b) Mobility for device N°41

Figure 5.30: Change in mobility in MWNTs for increasing exposure time (mobility measured in $m^2V^{-1}s^{-1}$)

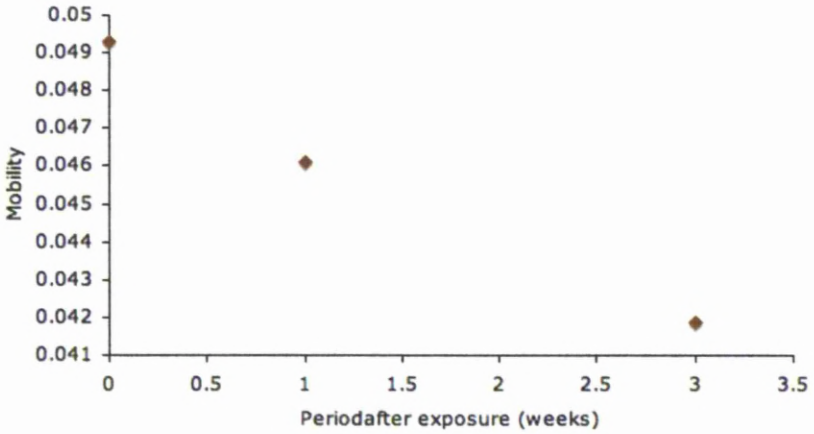

(a) Mobility for device N°93

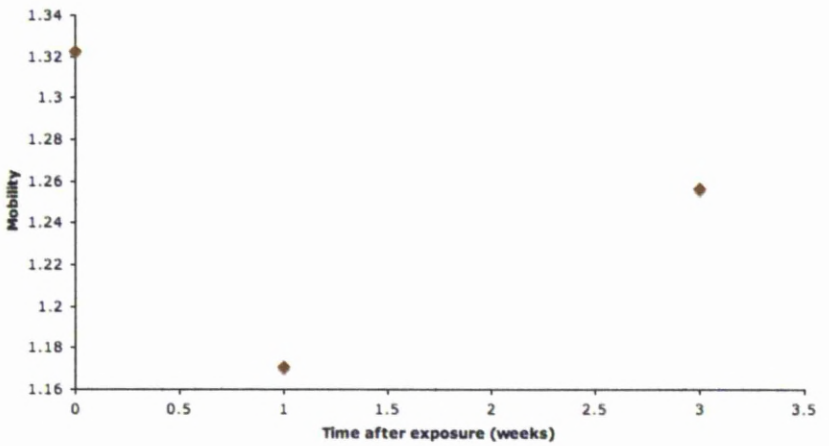

(b) Mobility for device N°41

Figure 5.31: Change in mobility during the time after exposure (mobility measured in $m^2V^{-1}s^{-1}$)

5.4 Fourier Transform Infrared Spectroscopy

Fourier transform infared spectroscopy (FTIR) is a chemical analysis technique which detects the vibration characteristics of chemical functional groups. When infrared light interacts with matter, chemical bonds will stretch, contract and bend. As a result, a chemical functional group tends to adsorb infrared radiation in a specific wavenumber range regardless of the structure of the rest of the molecule

Using CVD to grow MWNTs A. Misra et al [90] introduced ammonia gas during the growth process in order to dope the MWNTs with nitrogen. Once fabricated the nanotubes were analysed using FTIR. They reported a number of wavelength peaks attributed to bonds including; C-N at 1250cm^{-1}, N-CH_3 at 1372cm^{-1}, C-O_X at 2362cm^{-1}, C-H_X at 2851cm^{-1} and vibrational modes of MWNTs at 1445cm^{-1} and at 1736cm^{-1}. N atoms are expected to give strong IR activity if bonded into the carbon network absorption between 1200cm^{-1} and 1600cm^{-1} [90]. C-N peaks have also been reported by Y H Yan [91] who attached 1-Vinylimidazole to the sidewalls of SWNTs. C=N peaks have been seen in different materials at 1637cm^{-1} [91] 1650cm^{-1} [92] and 1672cm^{-1} [93]. C≡N was reported at X. H. Hang for carbon nitride films [94] and from 2100cm^{-1} to 2300cm^{-1} by Jama et al [95]. Jama et al also atributed bands at 1370cm^{-1} and 1570cm^{-1} to nitrogen doped amorphous carbon sp^2 graphitic bonds in nitride films. A C=C stretching mode has been reported to be infrared silent in pure unfunctionalised SWNTs at 1575cm^{-1} [91].

CNTs are drop cast on to the surface of a infrared transparent substrate, potassium bromide (KBR). In order ensure a high signal to noise ratio the densities of CNTs used need to be much higher than those which are required to create a percolation network. Once drop cast the samples are left to dry overnight and are then placed in the FTIR spectrometer which is purged for 20mins to remove moisture from the chamber. A background sample is taken with a blank KBR substrate which is then subtracted from the CNT spectra. Presented in figures 5.32, 5.33 and 5.34 are to date the best spectra observed. Once FTIR spectrometry has been performed on the unexposed samples (figure 5.32) they are exposed to 5mins of plasma they are then re-analysed (figure 5.33). After which they are subjected to a further 5mins in the plasma resulting in a total exposure time of 10mins, figure 5.34.

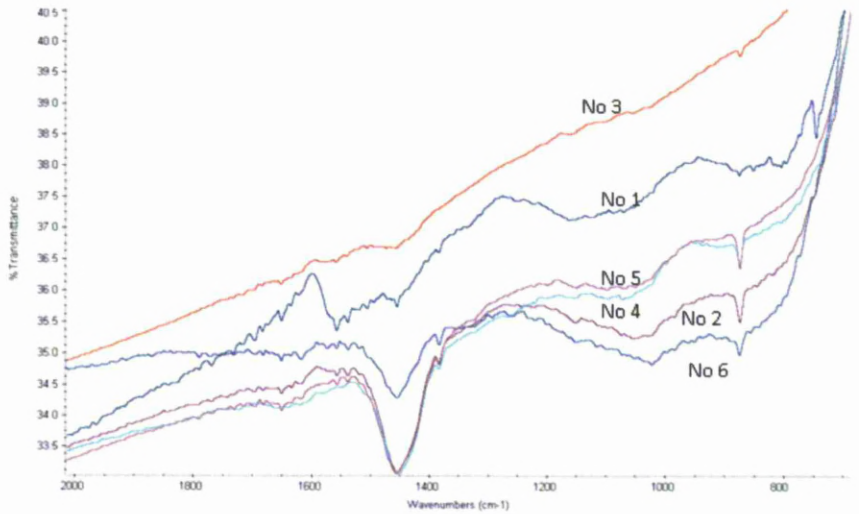

Figure 5.32: Before plasma exposure

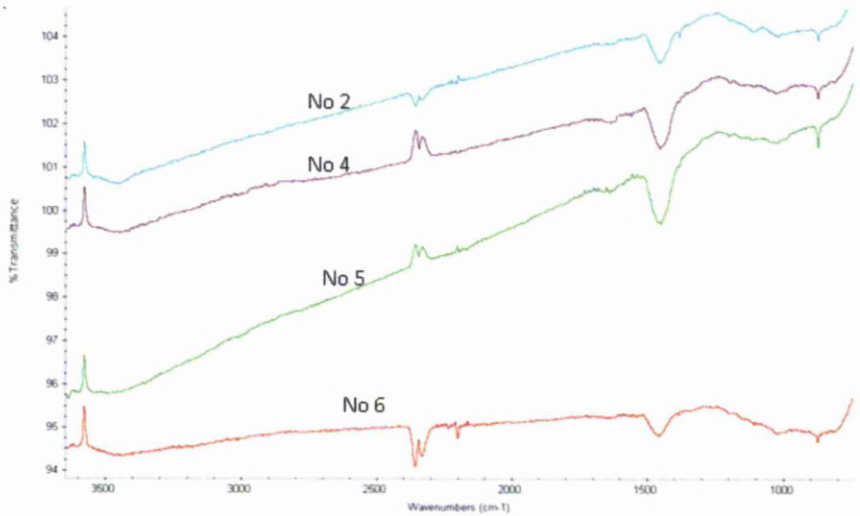

Figure 5.33: a number of samples after 5mins of plasma exposure, 10mTorr 10Watts 6cm plate distance

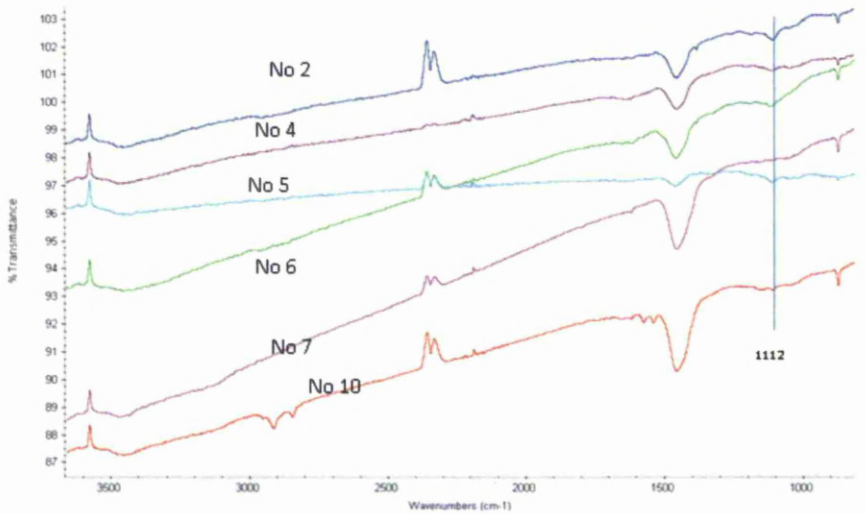

Figure 5.34: A number of sample after 10mins of plasma exposure 10mTorr 10Watts 6cm plate distance

The numbers shown in the figures 5.32, 5.33 and 5.34 represent different types of carbon nanotubes; 2: MWNTs, 4: LN_2 MWNTs from a red arc, 5: LN_2 MWNTs from a white arc, 6: LN_2 MWNTs from a white arc dispersed in 0.5% acetone, 7: Also LN_2 MWNTs from a white arc, 10: Also LN_2 MWNTs from a white arc however they were exposed at 20Watts whereas all the other samples were subject to 10Watt exposures.. The troughs which are present between 2400 and 2200cm^{-1} are a feature of a coating which is present on the KBR. The large peak visible for all samples at 1470cm^{-1} are part of a vibrational mode in the MWNTs which also gives rise to the 875cm^{-1} trough, it is these two troughs that show that MWNTs are present on the surface of the KBR. The most important feature within the spectra is the line which has developed at 1112cm^{-1}, marked on figure 5.34, this is interesting as it is not visible on the samples which were tested in figure 5.32, i.e. non plasma exposed. It is first visible in the 5min samples, figure 5.33, and is largest after 10mins in plasma exposure, figure 5.33. However as of yet this line is to be defined, and is 100cm^{-1} away from the C-N report by A. Misra et al [90]. It can be seen that there is a gradient in intensity from 3500cm^{-1} to 800cm^{-1} this is a feature of the FTIR spectrometer and can be removed if needed, however the variation in gradients between samples represents the density of material on the surface of the sample. Although the data is not presented here the samples have also been exposed for a further 5mins resulting in a total exposure time of 15mins, an early look at these results showed that all lines have decreased in intensity suggesting that there are less MWNTs on the surface or that the MWNTs have been damaged.

5.5 XPS Analysis of Carbon Nanotubes

X-ray photoelectron spectroscopy (XPS) is a powerful technique widely used for the surface analysis of materials. At low energy resolution it provides qualitative and quantitative information on the elements present whilst at high energy resolution it can provide information on the chemical state and bonding of elements. It is based on the principle that when a surface is irradiated with x-rays it emits photo electrons [96]. The photo electrons emited have a direct relationship to the atomic level which they came from. XPS detects all elements with an atomic number (Z) of 3 (lithium) and above. This limitation means that it cannot detect hydrogen (Z=1) or helium (Z=2). Each element produces a characteristic set of XPS peaks at characteristic binding energy values that directly identify each element that exist in or on the surface of the material being analyzed. These characteristic peaks correspond to the electron configuration of the electrons within the atoms, e.g., 1s, 2s, 2p, 3s, etc. The number of detected electrons in each of the characteristic peaks is directly related to the amount of element within the area (volume) irradiated. To generate atomic percentage values, each raw XPS signal must be corrected by dividing its signal intensity (number of electrons detected) by a "relative sensitivity factor" (RSF) and normalized over all of the elements detected. [97]

The technique is fully quantifiable in that the area under the peak is directly related to the concentration of the atomic species. The information can be readily interpreted by comparison to well know spectra of well know compounds. [96].

It is important to note that XPS detects only those electrons that have actually escaped into the vacuum of the instrument. The photo-emitted electrons that have escaped into the vacuum of the instrument are those that originated from within the top 10 to 12 nm of the material. All of the deeper photo-emitted electrons, which were generated as the X-rays penetrated 15 micrometers of the material, are either recaptured or trapped in various excited states within the material. For most applications, it is, in effect, a non-destructive technique that measures the surface chemistry of any material. [97]

5.5.1 Results

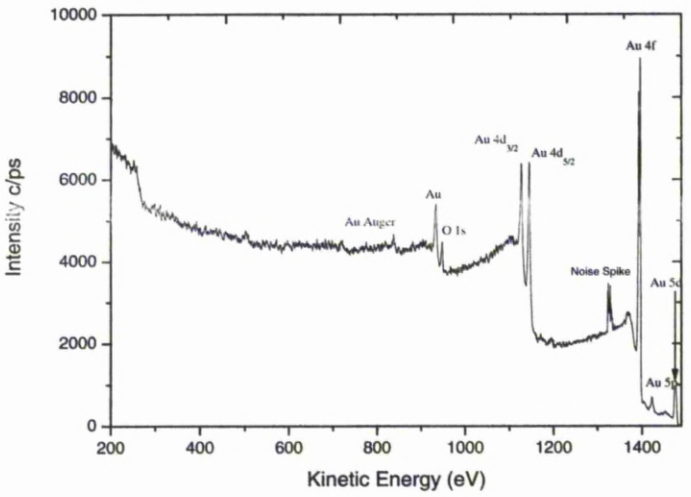

Figure 5.35: Clean gold sample

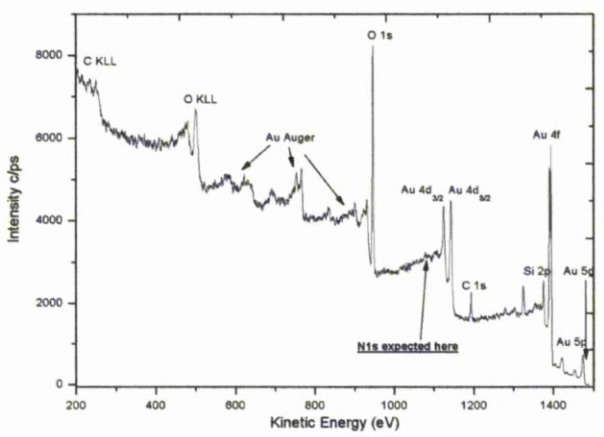

Figure 5.36: XPS of un-exposed sample

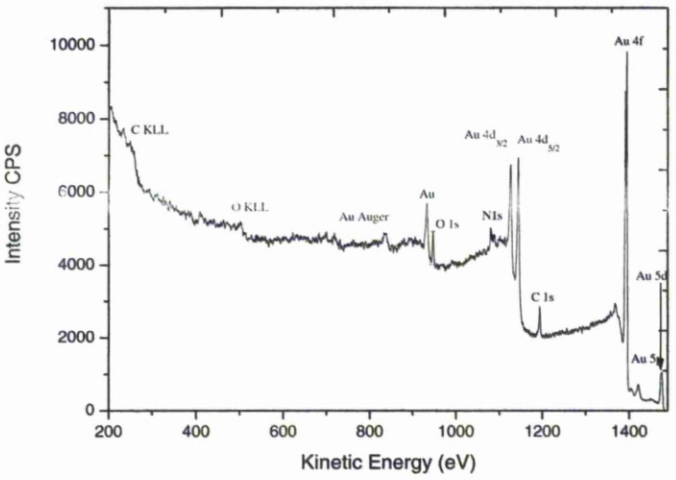

Figure 5.37: XPS of exposed sample, for 5 mins with an electrode distance of 6cm at 10mTorr and 10 Watts

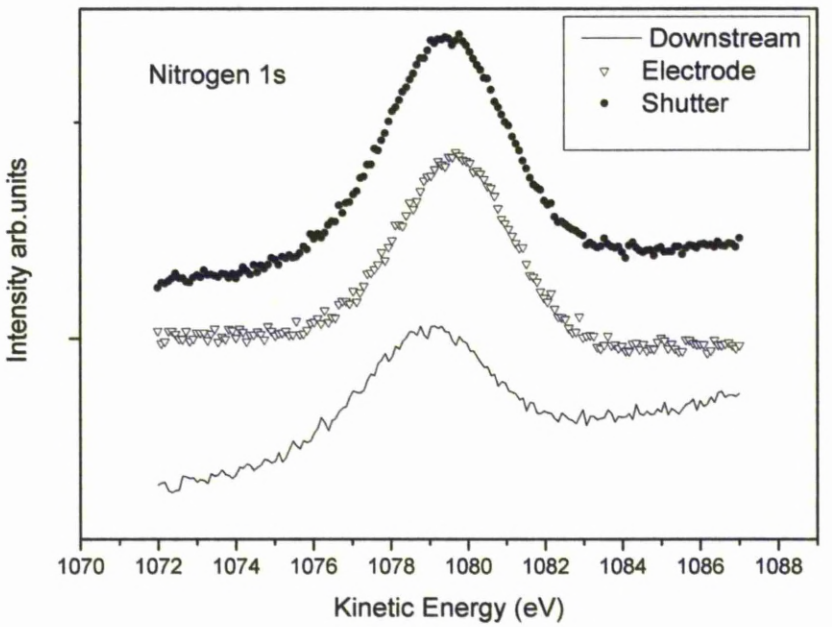

Figure 5.38: XPS of Nitrogen 1s on exposed sample for variation in position within RF plasma rig, for 5 mins with an electrode distance of 6cm at 10mTorr and 10 Watts. The various positions within the plasma where a) downstream were the sample was placed on a grounded surface downstream of the plasma, b) on the electrode (grounded), and c) on the shutter, this position was in the same gas flow position as the plasma but placed on a grounded surface just outside the main plasma region. Note each line shifted up for clarity.

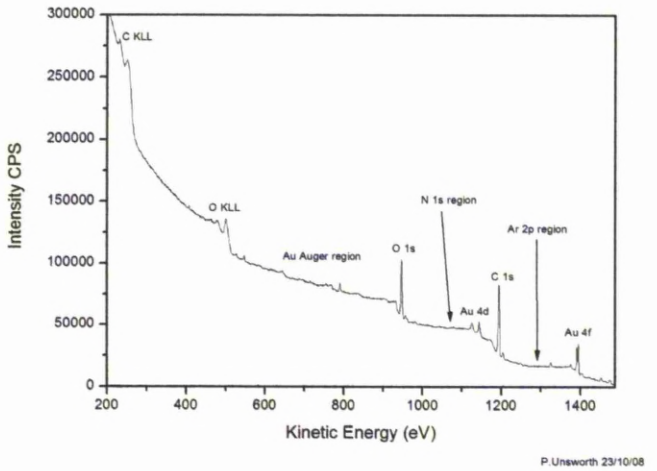

Figure 5.39: XPS of Argon plasma exposed sample

XPS results show that nanotubes exposed to plasma do have a higher Nitrogen content than those which are not exposed. Figure 5.35 shows the clean gold sample which provides a background spectrum. Figure 5.36 shows an unexposed sample with carbon peaks whereas figure 5.37 shows CNTs after exposure to RF nitrogen plasma, 5 mins with an electrode distance of 6cm at 10mTorr and 10 Watts. Using a higher resolution scan the nitrogen 1s peak can be seen in figure 5.38, here samples position within the plasma was varied. The various positions within the plasma where a) downstream were the sample was placed on a grounded surface downstream of the plasma, b) on the electrode (grounded), and c) on the shutter, this position was in the same gas flow position as the plasma but placed on a grounded surface just outside the main plasma region It was though that nanotubes could be damaged by the plasma and only when exposed to nitrogen gas (the chamber is vented to N_2) would the nitrogen attach to the damaged surface. Carbon nanotubes were then exposed to an argon plasma, figure 5.39 to determine how nitrogen and the chamber vented to argon. Nanotubes exposed to argon plasma did not show any nitrogen or argon within the sample, thus showing that the nitrogen attachment is due to the active species within the nitrogen RF plasma.

Amplitude variations show that samples are sensitive to various positions within the plasma and therefore, nitrogen attachment it related to plasma properties such as density and temperature, figure 5.38.

5.6 Raman Spectroscopy

The Raman spectra of carbon nanotubes result from a double-resonant process, where one resonance comes from the excitation energy matching an electronic transition and the second resonance from phonon or defect mediated scattering of the excited electron to a real state. Particular interest has been given to the excitation energy dependence of the D-band in graphite and carbon nanotubes.

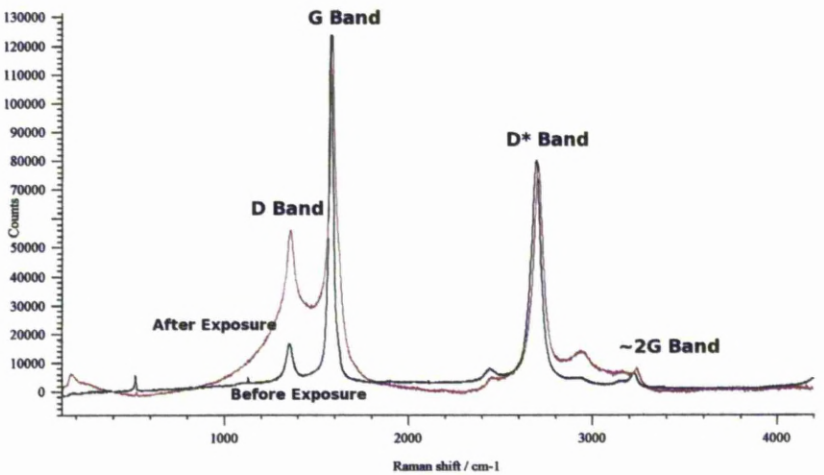

Figure 5.40: Example Raman

The change in the ratio between the D and G bands suggests that there are defects occurring in the carbon lattice of the nanotubes, these defects could be related to changes in the lattice structure due to nitrogen incorporation, it is also possible that some defects are created due to damage to the nanotubes from the plasma process.

5.7 Summary

Characterisation has taken place of the nanotubes which were both produced in house using the liquid arc method described in Chapter 3 and those purchased externally. Carbon nano-particles have been exposed to RF Plasma and the changes that have taken place have been observed. Analysis of the images taken of the nano-particles created in the plasma arc show that the arc method is a viable manufacturing method of easily producing high quality MWNTs. They show that amongst the CNTs of forms of crystalline carbon structures are produced, such as carbon onions. Comparisons of

the quantity (and ratios) of nano-particles produced over various different operating conditions can not be drawn from such imaging techniques as only very small sections can be observed. All operating conditions predominately produce MWNTs over and other structure. Of all the materials analysed possibly the most interesting was the carbon web like structure which was discovered to be air-born and accumulated with the condensation on the beaker used. This material contained few CNTs but probably contained many smaller carbon agglomerates such as carbon nanohorns. This material was unique to the liquid nitrogen method of production and was probably down to the volatile nature of the boiling liquid.

In order to study the CNTs properties before and after plasma functionalistion Random Network Carbon Nanotube (RNCNT) transistors were designed and produced. Consisting of two gold contacts on a silicon dioxide substrate they allow the electrical properties of the CNTs to be analysed. By drop casting random networks of CNTs over the two electrodes a conducting path can be created, it is this that is then exposed to the plasma and the changes monitored. The RNCNT transistors designed were tuned in order to produce the best results, smaller pads gave less leakage though the substrate, isolating transistors prevented the bulk nanotube layer from charging up, and 'burning off' nanotubes gave better performance. This last technique involved turning off all the semi-conducting nanotubes and passing high currents through the purely metallic channel paths. This increased RNCNT transistors gate dependence by removing purely metallic paths leaving only semi-conducting paths from the source to the drain. Finally the method of nanotube deposition was investigated. Nanotubes were drop cast onto the surface in a solution of dicholobenzene, this solution was chosen after nanotube 'bundling' was observed when using other liquids (xylene, acetone and toluene). Plasma modification of the substrate surface was also used to reduce the contact angle from 25% to 5%which improve the evaporation of the solution over the surface. By fine tuning the solution it was possible to obtain a even covering of nanotubes of the surface of electrodes, reducing variation across samples produced from the same materials under the same conditions. This chapter outlined a proposed theory for RNCNT transistor operation, the theory revolves around the work functions of the materials at the source and drain contact points. It is assumed that over the network the work function

difference between connecting parts will be low and will average out over the length of the channel. It is therefore the connections at the electrodes that ultimately decide the characteristics of the gate dependance. In the theory the RNCNT transistors can be said to be two back to back Schottky barriers. Other methods of analysis have also been carried out to build a bigger picture of the modification of carbon nanotubes, such as Fourier Transform Infrared Spectroscopy (FTIR), X-ray Photoelectron Spectroscopy (XPS), Raman Spectroscopy. These three techniques showed that nitrogen had been introduced into the lattice for both nanoparticles produced in a nitrogen environment (arc in LN_2) and by exposure to RF plasma. They also showed that the nanotubes had become damaged during the plasma process. It was suggested that this damage leads to loose bonds which the nitrogen can attach to. The XPS analysis also showed that the bonding structure was different depending on where within the plasma the samples were place and therefore the change in density and temperature of the plasma was a factor in how the nitrogen bonded to the surface. EDX analysis was also carried out but proved to be inconclusive.

This chapter aimed to show that it is possible to modify CNTs using clean safe plasma processing techniques. By exposing MWNTs to plasma it was hoped that it would be possible to modify the behaviour to produce a materials similar to that of SWNTs, thereby creating a material that has all of the desirable characteristics of both types of CNTs without the draw backs. However plasma functionalistion did not (on the whole) lead to a simple relationship between plasma exposure (times/pressure/power etc) and band gap modifications within the carbon. Although it has been shown that plasma modification can improve mobility within the CNTs by introduction of additional conduction bands, it is clear that different CNTs react differently to the modifications. SWNTs show increased conduction but with a small band gap, showing reduced p-type characteristics, as would be expected when introducing more carriers to the system. Changes to the SWNTs do not appear to be permanent as the increase conduction effect wears off with exposure to air. MWNTs did show greater gate dependence after plasma exposure as well as increased conduction however, true semi-conducting MWNTs have not been created as there was no voltage which could be applied to the gate to 'turn off' the channel current. As such these modified MWNTs can be said to

be semi-metals, showing both metallic and n-type semi-conducting behaviour.

Unlike the SWNTs modification to the MWNTs were permanent, although some de-absorbstion was observed. As explained in section 5.3 changes in device properties were seen due to plasma exposure, and using some basic MOSFET analysis it is possible to obtain the mobility of the carriers in the CNT-transistors. Further investigation into this work and some more honing of the techniques laid out within this chapter could lead to direct relationships between plasma properties and CNT mobilities.

Chapter 6

Summary and Recommendations

6.1 Summary

This thesis has investigated the possibility of producing low cost high yield carbon nanoparticles using various different methods. It also studies the basic RF Plasma theory needed to understand modification to carbon nanoparticles. An RF Plasma rig has been designed and constructed from the ground up to allow modification of carbon nanotubes to take place. The rig has been characterised along with the RF plasma generated within it. Using some well established techniques such as Langmuir Probes, Capacitive Probes and Mass Spectrometry, various plasma properties have been extracted to give a detailed understanding of the processes taking place. Multi Walled Carbon Nanotubes (MWNTs) have been created in the lab using a unique plasma in liquid technique, which harnesses the destructive power within the arc discharge to produce nano particles. This arc discharge in various liquids (Liquid Nitrogen, Water and a Water ethanol mix), has been studied using Optical Emission Spectroscopy (OES) and analysis of the electrical characteristics. A theory behind the formation and expansion of the gas bubble within the liquid has been proposed. By using OES time averaged and time resolved it has been possible to see that the production of the carbon nanoparticles are predominately produced at the end of the arc and that a higher current does not yeild more nanoparticles due to the volitile nature of the process. It has been shown that nanotube production in liquid is a valid up scalable process of creating carbon nanotubes. It is worth noting that the arc discharge in liquids is erratic and is therefore difficult to precisely maintain the same gap between the electrodes. However common features and trends can be seen. Such features have been used here to form

a time evaluation of the phenonenom and also develop an understanding of reactions within the plasma. Upscaling could involve more or larger electrodes, with a liquid flow allowing for continuous production of carbon nanoparticles. Although the extremely volatile nature of water/ethanol mixture would require more specialised equipment to prevent the liquid from igniting if upscaling was to be considered.

Once produced and functionalised carbon nanoparticles have been analysed using various different methods, the main one being Random Network Carbon Nanotube (RNCNT) transistors. RNCNT transistors, through great difficulty, have been designed and developed into functional molecular electron devices. The electrical properties of these devices have been investigated, and they have been used as a analytical tools. RNCNT transistors use a percolation path structure to enable transistor channel conduction, which averages the properties of the nanotubes across the channel. Methods for optimising RNCNT transistors, such as burn off, densities at the percolation threshold and modification of the substrate, have been laid out, and a Schottky barrier theory has been suggest as the method of gate control over RNCNT transistors. Other methods of analysis have been carried out to build a bigger picture of the modification of carbon nanotubes, such as Fourier Transform Infrared Spectroscopy (FTIR), X-ray Photoelectron Spectroscopy (XPS), Raman Spectroscopy, Scanning Electron Microscopy (SEM) and Transmission electron microscopy (TEM).

This thesis aimed to show that it is possible to modify MWNTs to have behaviour that is similar to that of single wall nanotubes (SWNTs), thereby creating a material that has all of the desirable characteristics of both types of CNTs without the draw backs. Although it has been shown that plasma modification can improve mobility within the CNTs by introduction of additional conduction bands, different CNTs react differently to the modifications. SWNTs show increased conduction but with a small band gap, showing reduced p-type characteristics, as would be expected when introducing more carriers to the system. Changes to the SWNTs do not appear to be permanent as the increase conduction effect wears off with exposure to air. MWNTs did show greater gate dependence after plasma exposure as well as increased conduction however, true semi-conducting MWNTs have not been created as there was no voltage which could be applied to the gate to 'turn off' the channel current. As such these

modified MWNTs can be said to be semi-metals, showing both metallic and n-type semi-conducting behaviour. This result can be explained by considering the density state measurements taken by Terrones et al [30]. Figure 6.1(a) shows the original density of states (DoS) of a MWNT (in red as taken from Terrones et al), overlaid with the proposed modification to the CNTs DoS (in black) as discussed in Chapter one. It can been seen in figure 6.1(a) that in the proposed scenario adding extra carriers to the CNTs produces an additional state, around the Fermi level, which acts to give the CNTs a more semi-conducting like behaviour. However as this chapter has shown an additional localised state producing improved device switching did not occur. However overall conduction was increased, this can be explained by examining figure 6.1(b), in this scenario a much broader peak has been added which increases the overall conduction of the CNTs but does not add a localised state to increase semi conducting behaviour which is consistent with current voltage curves results shown earlier. This is to say that there is now a broader range of states that carriers in the system may now occupy.

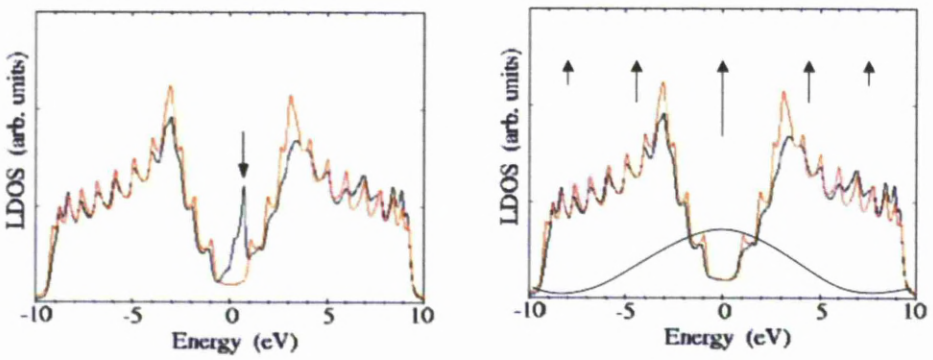

(a) Proposed DoS modifications

(b) Actual DoS modifications

Figure 6.1: Density of States for a single MWNT, red taken from [30].

Unlike the SWNTs modification to the MWNTs were permanent, although some de-absorbstion was observed. As explained in chapter 5.3 changes in device properties were seen due to plasma exposure, and using some basic MOSFET analysis it is possible to obtain the mobility of the carriers in the CNT-transistors.

6.2 Recommendations for Further Work

This thesis produces a foundation for further investigation in to a number of interesting areas of research. Most notably an expansion on the formation of nano particles using arc discharge in liquids. Extraction of electron temperatures and densities from OES spectra would give knowledge of the energies within the arc for a greater understanding and therefore allow for deeper explanations and pave a route forward to effective modelling of arc discharges within liquids. The experiment could be improved in a number of ways, firstly a more focused OES could allow for spacial spectra to be acquired giving an understanding of data from one electrode to the other. This could compliment data taken using a high speed camera to view the evolution of the discharge. Variation in electrodes, such as those containing dopant, to increase yield could provide interesting results as well as the potential to produce new materials with various different properties by including dopants at growth. Expanding this further it could prove productive to investigate pressurised liquids to vary nanotube yield/quality. A more thorough investigation into water ethanol mixtures would allow tuning of yields, however this should be approached with care. A computer controlled feedback loop for controlling the plasma arc gap would mean that a more consistent arc was available for analysis. Variation in gases used to modify CNTs within the RF plasma discharge could be investigated, gases such as ammonia would also allow for active nitrogen species. Plasma functionalistion is not limited to RF discharges, other novel discharges would also provide a suitable environment for modification of carbon nanotubes, such as dielectric barrier discharges (DBD), and possibly even micro plasmas for localised functionalistion of areas within on a substrate, allowing functionalistion of some but not all CNTs. Further investigation into RNCNT transistors could prove interesting for large scale printing of electronic circuits, however manipulation of nanotubes on a smaller scale would allow for better analysis of plasma functionalistion.

6.3 Epilogue

I would like to take this opportunity to reflect on producing this PhD Thesis. I did not anticipate the wide range of activities involved in being a PhD student however; I have enjoyed mentoring a number of MSc and PhD students, as well as producing, hosting and marking undergraduate laboratory experiments, devising experiments, designing and building experimental apparatus, writing software, giving presentations, presenting posters, discussing my work with others at various international conferences and having the chance to use so many fantastic pieces of scientific equipment. All the research presented in this thesis was carried out between 2005 and 2008 at the University of Liverpool, and was written up during a very difficult 2009. Again I would like to thank all those who have made this work possible especially my supervisors, Prof J W Bradley and Dr I Alexandrou, for providing me with this fantastic opportunity.

Appendix A

OES Line Assignments

Wavelength	Line assignment	Ref
318.7369	Atomic O	[6]
350.7416	Atomic O	[6]
352.089	Atomic O	[6]
358.421	CN	[7]
358.76	C_2 - Deslandres–D'Azambuja	[2, 3]
359.29	C_2 - Deslandres–D'Azambuja	[2, 3]
360.73	C_2 - Deslandres–D'Azambuja	[2, 3]
370.337	Atomic O	[6]
384.9	CN	[2, 3, 4, 7]
384.9	CN	[7]
385.22	C_2 - Deslandres–D'Azambuja	[2, 3]
385.517	CN	[7]
386.186	CN	[7]
388.36	CN	[7]
392.069	Atomic C	[6]
392.44	Atomic O	[6]
406.5	H_2	[5]
410.26	Atomic H	[6]
411.259	C_2 - Deslandres–D'Azambuja	[2, 3]
438.2	C_2 - Carbon Swan 1	[2, 4]
437.14	C_2 - Carbon Swan 1	[2, 4]
436.49	C_2 - Carbon Swan 1	[2, 4]
416.8	CN	[2, 3, 4, 7]
416.926	N	[6]
417.616	Atomic N	[6]
426.726	C+	[6]
430.725	N	[6]
431.4	CH	[8]
434	Hγ	[6]
443.274	Atomic N	[6]
451.091	Atomic N	[6]
460.6	CN	[2, 2, 4, 7]
460.6	CN	[2, 2, 4, 7]
466.9	C_2 - Carbon Swan 2	[2, 4]
468.5	C_2 - Carbon Swan 2	[2, 4]
469.8	C_2 - Carbon Swan 2	[2, 4]
471.5	C_2 - Carbon Swan 2	[2, 4]
473.71	C_2 - Carbon Swan 2	[2, 4]
477.1	Atomic C	[6]
477.1	Atomic C	[6]
505.6	C_2 - Carbon Swan 3	[2, 4]
507	C_2 - Carbon Swan 3	[2, 4]
509.7	C_2 - Carbon Swan 3	[2, 4]

512.9	C_2 - Carbon Swan 3	[2, 4]
516.52	C_2 - Carbon Swan 3	[2, 4]
531.435	Atomic N	[3, 4]
547	C_2 - Carbon Swan 4	[2, 4]
550.1	C_2 - Carbon Swan 4	[2, 4]
554	C_2 - Carbon Swan 4	[2, 4]
558.5	C_2 - Carbon Swan 4	[2, 4]
563.55	C_2 - Carbon Swan 4	[2, 4]
592.39	C_2 - Carbon Swan 5	[2, 4]
595.9	C_2 - Carbon Swan 5	[2, 4]
597.7	NH2	[2, 4]
600.4	C_2 - Carbon Swan 5	[2, 4]
605.97	C_2 - Carbon Swan 5	[2, 4]
607.019	Unable to identify from literature	
631.098	H	[6]
650.631	Atomic N	[6]
653.36	C_2 - Carbon Swan	[3, 4]
656.3	H_2 - Hα	[5]
658.761	Atomic C	[6]
661.056	Atomic O	[6]
688.901	Unable to identify from literature	
706.068	Unable to identify from literature	
711.318	Atomic C	[6]
717	H2	[6]
717.494	N_2	[6]
722.9142	Atomic O	[6]
734.6367	Atomic O	[6]
736.1647	Atomic O	[6]
740.7341	Atomic O	[6]
750	N2	[6]
756.5482	Atomic O	[6]
767.6944	Atomic O	[6]
770.675	Atomic O	[6]
777.194	O_2	[5]
777.194	O_2	[5]
780	N2	
786.889	Unable to identify from literature	
805.862	Atomic C	[6]
817.501	Unable to identify from literature	
844.912	O_2	[5]
309.23 - 314.37971	OH	[1]
762.524 - 768.193	Unable to identify from literature	
764.192 - 770.5226	Unable to identify from literature	

Bibliography

[1] Dresselhaus, G. & Avouris, P. *Carbon nanotubes: synthesis, structure, properties and applications.* Springer, (2001).

[2] Saito, Y. *et al. Ultramicroscopy* **73**(1-4), 1–6 (1998).

[3] Amaratunga, G. A. J. *IEEE Spectrum* , 28 September (2003).

[4] Palser, A. H. *Phys. Chem. Chem Phys* **1**, 4459 (1999).

[5] BMC-RACING. *www.bmc-racing.com* .

[6] Mylvaganam, K. & Zhang, L. C. *Nanotechnolgy* **18** (2007).

[7] Fennimore, A. M. *et al. Nature* **424**, 408 july (2003).

[8] Son, S. J., Reichel, J., He, B., Schuchman, M. & Lee, S. B. *Journal of American Chemical Society* **127**, 7316 (2005).

[9] Bianco, A., Kostarelos, K. & Prato, M. *Current Opinion in Chemical Biology* **9**(6), 674 (2005).

[10] Borowiak-Palen, E. *Phys. Stat. Sol* **244**(11), 4311 (2007).

[11] Schindler, A., Brill, J., Fruehauf, N., Novak, J. P. & Yaniv, Z. *Physica E* **37**, 119 (2007).

[12] Xiao, L., Chen, Z. & Fan, S. *Nano Letters* **8**(12), 4539 (2008).

[13] Mitra, S. *Journal of Materials Chemistry by the Royal Society of Chemistry* (2007).

[14] Dai, L., Gong, K., Du, F., Xia, Z. & Dustock, M. *Science* **323**, 760 (2009).

[15] Paradise, M. & Goswami, T. *Materials and Design* **28**, 1477 (2007).

[16] Avouris, P., Appenzeller, J., Martel, R. & Wind, S. J. *Proceedings of The IEEE* **91**(11) (2003).

[17] Antisari, . M., RenzoMarazzi & RadenkaKrsmanovic. *Carbon* **41**, 2293 (2003).

[18] Alexandrou, I., Wang, H., Sano, N. & Amaratunga, G. A. J. *J. Chem. Phys.* **120**(2), 1055 – 1058 (2004).

[19] Tanaka, K., Yamabe, T. & Fukui, K. *The Science and Technology of Carbon Nanotubes.* Elsevier, (1999).

[20] Thostenson, E. T., Li, C. & Chou, T.-W. *Composites science and technology* , 491 (2005).

[21] Bustero, I. *et al. Microchimica acta* **152**, 239–247 (2006).

[22] Ikegami, T., Nakanishi, F., Uchiyama, M. & Ebihara, K. *Thin Solid Films* **457**, 7 (2004).

[23] Kuo, T. F., Chi, C. C. & N, I. N. L. *Japanese Journal of Applied Physics* **40**, 7147 (2001).

[24] Vivien, C., Hermann, J., Perrone, A., Boulmer-Leborgneand, C. & Luches, A. *Journal of Physics D : Applied Physics* **31**, 1263 (1998).

[25] Xiao, K. *Journal of American Chemical Society* (2005).

[26] Czrew, R. & Terrones, M. *Nano Letters* **1**(9), 457 – 460 (2001).

[27] Khare, B. *Nano Letters* **2**(1), 73 – 77 (2002).

[28] Khare, B. & Meyyappan, B. *Appl. Phys. Lett.* **81**(27), 5237 (2002).

[29] Inagaki, N. *Plasma Surface Modification and Plasma Polymerization.* Technomic Publishing Co., (1996).

[30] Terrones, M. *et al. Applied Physics A* **74**, 355 – 361 (2002).

[31] Chen, F. F. *Introduction to Plasma Physics and Controlled Fusion.* Springer, 2nd edition, (2006).

[32] Lieberman, M. A. & Lichtenberg, A. J. *Principles of plasma discharges and materials processing.* Wiley-Iinterscience Publication, (1994).

[33] Chapman, B. *Glow Discharge Processes.* John Wiley and Sons, (1980).

[34] Heason, D. J. *A study of a low pressure RF plasma in the presence of an electron beam.* PhD thesis, University of Manchester Institute of science and technology, January (2001).

[35] Felton, A. *J. Appl. Phys.* **98**, 74308 (2005).

[36] Chirila, V. *Surface and Coating Technology* (200), 548 – 551 (2005).

[37] Plank, N. & Jiang, L. *Appl. Phys. Lett.* **83**(12), 2426–2438 (2003).

[38] Plank, N. & R.Cheung. *Microelectronic Engineering* **73/74**(578 - 582) (2004).

[39] Plank, N. & Fores, G. *Phys. Chem. Lett. B* (109), 22096 – 22101 (2005).

[40] *Carbon Nanotubes.* Pergamon, (1996).

[41] Rutherford & Goldston. *Intoduction to plasma physics.* IOP, (1995).

[42] Mott-Smith, H. & Langmuir, I. *Phys. Rev.* **28**, 727 (19826).

[43] Sternovsky, Z., Robertson, S. & Lampe, M. *J. Appl. Phys.* **94**(3), 1374 August (2003).

[44] A, B. & F, M. *Nuouo Cimento* **29**(487) (1963).

[45] Garscadden, A. & Emeleus, K. G. *Proceedings of Physical Society* **79**, 535 (1962).

[46] Crawford, F. W. *J. Appl. Phys.* **34**(7), 1897 (1962).

[47] Annaratone, B. M. & Braithwaite, N. S. J. *measurement science and technology* **2**, 795 (1991).

[48] Braithwaite, N. S. J., Benjamin, N. M. P. & Allen, J. E. *J. Phys. E: Sci Instrum* **20**, 1046 (1987).

[49] Dyson, A., Bryant, P. M. & Allen, J. E. *measurement science and technology* **11**(5), 554 – 559 (2000).

[50] Watanabe, M., Shaw, D. M. & Collins, G. J. *J. Appl. Phys.* **85**(7), 3428 (1999).

[51] Yatsuzuka, M., Morishita, K., Satoh, K. & Nobuhara, S. *Japanese Journal of Applied Physics* **24**(12), 1724 (1985).

[52] Analytical, H. *Hiden Analytical EQP300 Operation Manual.* Hiden Analytical.

[53] Sano, N. *et al. J. Appl. Phys.* **92**(5) (2002).

[54] *MS260i Imaging Spectrograph Instruction Mannual.* LOT Oriel Instruments.

[55] Swindles, I. Master's thesis, Univeristy of Liverpool, (2007).

[56] Henke, B. L. *Advances in X-Ray Analysis* **4**(244) (1961).

[57] Domke, A. Master's thesis, University of Liverpool, (1999).

[58] Scott, C. D., Arepalli, S., Nikolaev, P. & Smalley, R. E. *Applied Physics A* **72**, 573 – 580 (2001).

[59] Kuo, T. F. *Japanese Journal of Applied Physics* **40**, 7147 – 7150 (2001).

[60] Du, C. & Pan, N. *Materials Letters* **59**, 1678 – 1682 (2005).

[61] Kobayashi, Y., Nakashima, H., Takagi, D. & Homma, Y. *Thin Solid Films* **464 - 465**, 286 – 289 (2004).

[62] Thostenson, E. T. *Composites science and technology* **61**, 1899 – 1912 (2001).

[63] Sano, N., Nakano, J. & Kanki, T. *Carbon* **42**, 667 (2004).

[64] Saidane, K. *et al. Journal of Physics D : Applied Physics* **37**, 232 (2004).

[65] Ishigami, M., Cumings, J., Zettl, A. & Chen, S. *Chemical Physics Letters* **319**, 457 (2000).

[66] Eubank, P. T., Patel, M. R., Barrufet, M. A. & Bozkurt, B. *J. Appl. Phys.* **73**(11), 7900 (1993).

[67] Xing, C., Jia, S., Xing, J. & Shi, Z. *Plasma Science and Technology,* **9**(6), 770 (2007).

[68] Akita, S., ASHIHARA, H. & NAKAYAMA, Y. *Japanese Journal of Applied Physics* **39**, 4939 (2000).

[69] Descoeudres, A., Hollenstein, C., Demellayer, R. & Walder, G. *Journal of Physics D : Applied Physics* **37**, 875 (2004).

[70] Pillow, M. E. *Proceedings of Physical Society* **8**, 737 – 739 (1953).

[71] Acquaviva, S. & Giorgi, M. L. D. *Journal of Physics B* **35**, 795 (2002).

[72] Danylewych, L. & Nicholls, R. *Proc R Soc Lond A* **339**, 197 (1974).

[73] Pretty, W. E. *Proceedings of Physical Society* **40**, 71 – 78 (1927).

[74] Griem. *Plasma Spectroscopy.* McGraw Hill, (1961).

[75] Albinski, K., Musiol, K., Miernikiewicz, A., Labuz, S. & Malota, M. *Plasma Scources Science and Technology* **5**, 736 (1996).

[76] Byszewski, P., Langec, H., Huczkoc, A. & Behnke, J. F. *J. Phys. Chem. Solids* **58**(2), 1679 (1997).

[77] Xu, N. *et al. Journal of Physics D : Applied Physics* **30**, 1370 (1997).

[78] Acquaviva, S. & Giorgi, M. L. D. *Journal of Physics B* **35**, 795 – 806 (2002).

[79] NIST. *online database* .

[80] Guchardi, R. & Hauser, P. C. *J. Chromat. A.* (333), 1033 (2004).

[81] Engleman, R. *J. Quant. Spec. Radiat.* **12**(1347) (1972).

[82] Lange, H. *et al. Carbon* **41** (2003).

[83] Gidalevich, E. & Boxman, R. L. *Plasma Scources Science and Technology* **15**, 765 (2006).

[84] O'Hanlon, J. F. *A user's guide to vacuum technology.* Wiley, (2003).

[85] Bultinck, E. *Numerialcal simulationj of a magnetron discharge utilized fro the reactive sputter deposition of titanium nitride and oxide layers.* PhD thesis, University of Antwerp, (2009).

[86] lieberman, M. A. *IEEE Transactions on Plasma Science* **16**(6), 638 (1988).

[87] Frank, D. J. & Lobb, C. J. *Phys. Rev. B* **37**(1) (1988).

[88] Hu, L., Hecht, D. & Gruner, G. *Nano Letters* **4**(12), 2513–2517 (2004).

[89] Munson-McGee, S. H. *Phys. Rev. B* **43**(3331) (1991).

[90] Misra, A., Tyagii, P. K., Singh, M. K. & Misra, D. S. *Diamond and related materials* **15**, 385 – 388 (2006).

[91] Yan, Y. H., Cui, J., Chan-Park, M. B., Wang, X. & Wu, Q. Y. *Nanotechnolgy* **18**, 115712 (2007).

[92] Narayanan, V. A., Stump, N. A., Cul, G. D. D. & Vo-Dinh, T. *journal of raman spectroscopy* **30**(6), 435 – 439 (1999).

[93] Khare, B., Wilhite, P., Tran, B., Teixeira, E. & Meyyappan, M. *J. Chem. Phys. B* **109**, 23466 (2005).

[94] Han, H.-X. & Feldman, B. J. *Solid State Communications* **65**, 921 (1988).

[95] Jama, C. *Thin Solid Films* **302**, 58 – 56 (1997).

[96] Myhra, S., White, T. J., Kesson, S. E. & Riviere, J. C. *American Mineralogist* **73**, 61–167 (1988).

[97] Filatova, E. O. & Shulakov, A. S. *Brilliant Light in Life and Material Sciences* , 371–381 (2007).